



Horizon 2020
Programme

FOCUS-Africa

Research and Innovation Action (RIA)

This project has received funding from the European
Union's Horizon 2020 research and innovation programme
under grant agreement No 869575

Start date : 2020-09-01 Duration : 48 Months



Report on the regionalextreme eventsidentification andvariability

Authors : Dr. Petitta MARCELLO (AMIGO), Erasmo Buonomo (Met Office), Scott Burgan (Met Office), Nico Caltabiano (WMO), Sara Dal Gesso (Amigo), Joseph Darron (Met Office), Matteo Dell'Acqua (SSSA), Francois Engelbrecht (WITS), Hannah Griffith (Met Office), Federica Guerrini (Amigo), Kate Hamp (Met Office), Chris Jack (CSAG-UCT), Chris Lennard (CSAG-UCT), Jonathan Padavatan (WITS), Marcello Petitta (Amigo), Jessica Steinkopf (WITS), Robel Takele (SSSA), Laura Trentini (Amigo), Lisa van Aardenne (CSAG-UCT), Piotr Wolski (CSAG-UCT)

FOCUS-Africa - Contract Number: 869575

Project officer: Anna-Natasa ASIK

Document title	Report on the regionalextreme eventsidentification andvariability
Author(s)	Dr. Petitta MARCELLO, Erasmo Buonomo (Met Office), Scott Burgan (Met Office), Nico Caltabiano (WMO), Sara Dal Gesso (Amigo), Joseph Darron (Met Office), Matteo Dell'Acqua (SSSA), Francois Engelbrecht (WITS), Hannah Griffith (Met Office), Federica Guerrini (Amigo), Kate Hamp (Met Office), Chris Jack (CSAG-UCT), Chris Lennard (CSAG-UCT), Jonathan Padavatan (WITS), Marcello Petitta (Amigo), Jessica Steinkopf (WITS), Robel Takele (SSSA), Laura Trentini (Amigo), Lisa van Aardenne (CSAG-UCT), Piotr Wolski (CSAG-UCT)
Number of pages	87
Document type	Deliverable
Work Package	WP3
Document number	D3.3
Issued by	AMIGO
Date of completion	2022-11-03 16:06:31
Dissemination level	Public

Summary

Extreme atmospheric hazards are high-impact weather events caused by processes in the Earth's atmosphere that typically result in significant losses and damages. They can have serious consequences for various sectors in the SADC (Southern African Development Community) region, including energy, water, infrastructure, and food security. Because of the region's extensive linkages and significant interdependence, these impacts are amplified, notably amongst the water, energy, and food sectors. As a large part of the region is already critically vulnerable to droughts, floods, climate variability, and high temperatures caused by extreme events (Ramirez-Villegas et al., 2021), addressing the region's existing and emerging infrastructure-water-energy-food issues necessarily requires a better knowledge of major climate hazards. In this framework, Task 3.3 aims to contribute to a better understanding of how climate variability affects the quality of seasonal and decadal forecasts in terms of extreme event description and change, taking into account both frequency and intensity. This task will also look into the future distribution and magnitude of extremes in high-resolution climate projections, which is key for the region's adaptation and mitigation efforts. Particular attention is paid to characterizing the dynamics of extreme rainfall in seasonal forecasts and climate projections for the agricultural sector. This will make use of recently developed methodologies for identifying extreme events, which will build on previously developed specific Extreme Climate Indexes (ECI) and advanced methods for compound, concurrent, and recurring extreme events. ?

Approval

Date	By
2022-11-07 11:23:58	Mrs. Kate DART (MO)
2022-11-12 15:55:01	Mrs. Roberta BOSCOLO (WMO)



Report on the regional extreme events identification and variability

Deliverable D3.3

Lead Beneficiary: AMIGO

10/2022

Erasmus Buonomo¹, Scott Burgan¹, Nico Caltabiano², Sara Dal Gesso³, Joseph Darron¹, Matteo Dell'Acqua⁴, Francois Engelbrecht⁵, Hannah Griffith¹, Federica Guerrini³, Kate Hamp¹, Chris Jack⁶, Chris Lennard⁶, Jonathan Padavatan⁵, Marcello Petitta³, Jessica Steinkopf⁵, Robel Takele⁴, Laura Trentini³, Lisa van Aardenne⁶, Piotr Wolski⁶

¹ Met Office (MO), Exeter, UK

² World meteorological organization (WMO), Geneva, Switzerland

³ Amigo Climate, Roma, Italy

⁴ Institute of Life Sciences, Sant'Anna School of Advanced Studies, Pisa, Italy

⁵ Global Change Institute – University of the Witwatersrand (WITS), Johannesburg, South Africa

⁶ Climate System Analysis Group, University of Cape Town (UCT), Cape Town, South Africa



This project has received funding from the European Commission's Horizon 2020 Research and Innovation Programme. The content in this presentation reflects only the author(s)'s views. The European Commission is not responsible for any use that may be made of the information it contains.

www.focus-africaproject.eu

Document Information

Grant Agreement: 869575

Project Title: Full-value chain Optimised Climate User-centric Services for Southern Africa

Project Acronym: Focus-Africa

Project Start Date: 1 September 2020

Related work package: WP 3

Related task(s): Task 3.3

Lead Organisation: Amigo

Submission date:

Dissemination Level: PU

History

Date	Submitted by	Reviewed by	Version (Notes)
27/10/2022	Amigo		V1



About FOCUS-Africa

FOCUS-Africa – Full-value chain Optimised Climate User-centric Services for Southern Africa – is developing sustainable tailored climate services in the Southern African Development Community (SADC) region for four sectors: agriculture and food security, water, energy and infrastructure.

It will pilot eight case studies in six countries involving a wide range of end-uses to illustrate how the application of new climate forecasts, projections, resources from Copernicus, GFCS and other relevant products can maximise socio-economic benefits in the Southern Africa region and potentially in the whole of Africa.

Led by WMO, it gathers 14 partners across Africa and Europe jointly committed to addressing the recurring sustainability and exploitation challenge of climate services in Africa over a period of 48 months.

For more information visit: www.focus-africaproject.eu

Coordinator Contact

Roberta Boscolo | Climate & Energy Scientific Officer

Applied Climate Services Division

Services Department

World Meteorological Organization (WMO)

CP 2300, 1211 Geneva SWITZERLAND

email: rboscolo@wmo.int

Table of Content

ABOUT FOCUS-AFRICA	3
TABLE OF CONTENT.....	4
TABLES.....	5
FIGURES.....	5
EXECUTIVE SUMMARY	9
KEYWORDS	9
1 INTRODUCTION	10
2 ASSESSING THE REPRESENTATION OF EXTREME TEMPERATURE AND RAINFALL IN REGIONAL CLIMATE MODEL SIMULATIONS OVER SOUTHERN AFRICA TO INFORM SECTORAL APPLICATIONS	11
2.1 BACKGROUND ON CLIMATE RISKS AND TRENDS IN SOUTHERN AFRICA	11
2.2 DATASETS	11
2.3 OBSERVATIONS	11
2.4 REGIONAL CLIMATE MODELS AND ENSEMBLES CONSIDERED	12
2.4.1 CP4A.....	12
2.4.2 CORDEX.....	13
2.5 EVALUATION OF EXTREMES FROM SHORT DURATION EVENTS – HISTORICAL CLIMATOLOGY	13
2.5.1 Maximum Daily Temperature - TXx	13
2.5.2 Minimum Daily Temperature - TNn	14
2.5.3 Maximum Daily Precipitation - RX1	15
2.5.4 Conclusion.....	16
2.6 CLIMATE CHANGE RESPONSE.....	16
2.6.1 Maximum Daily Temperature - TXx	17
2.6.2 Minimum Daily Temperature - TNn	18
2.6.3 Maximum Daily Precipitation – RX1	18
2.7 EVALUATION	19
2.7.1 Mean temperature.....	20
2.7.2 Mean precipitation	20
2.8 SUMMARY	23
3 REVIEW OF IMPACTS OF CLIMATE EXTREMES, INCLUDING COMPOUND EVENTS, IN AGRICULTURE AND NEW METHODOLOGIES.....	24
3.1 EXTREME EVENTS AND AGRICULTURE.....	24
3.2 NEW METHODS.....	25
3.3 REMARKS	26
4 THE ENSO TELECONNECTION TO SOUTHERN AFRICA IN A CHANGING CLIMATE.....	27
4.1 DATA AND METHODS.....	28
4.2 RESULTS	28
4.3 SUMMARY	33
5 CHARACTERIZING THE NATURE OF CROP GROWING SEASON RAINFALL EXTREMES DURING ANOMALOUS YEARS IN SEASONAL FORECASTS	38
5.1 DATA AND METHODS.....	38
5.1.1 Hindcast data.....	38
5.1.2 Rainfall extremes	39
5.2 CHARACTERIZING MODULATION BY ENSO AND IOD EVENTS	40
5.3 RESULTS AND DISCUSSION	42
5.3.1 Spatial distribution of rainfall extremes	42
5.3.2 Historical composites.....	43
5.3.3 Relationship and linkage between rainfall extremes with ENSO and IOD	45

5.4	REMARKS	48
6	RAINFALL EXTREMES IN LAKE MALAWI REGION	49
6.1	OBJECTIVES.....	49
6.2	ANALYTICAL FRAMEWORK	49
6.3	METHODS.....	49
6.3.1	<i>Extreme rainfall and moisture flow regimes.....</i>	<i>50</i>
6.3.2	<i>Extreme rainfall and circulation states</i>	<i>50</i>
6.3.3	<i>Extreme rainfall projections.....</i>	<i>51</i>
6.4	RESULTS	52
6.4.1	<i>Extreme rainfall and moisture flow regimes.....</i>	<i>52</i>
6.4.2	<i>Extreme rainfall and circulation states</i>	<i>53</i>
6.4.3	<i>Extreme rainfall projections.....</i>	<i>58</i>
6.5	REMARKS	65
7	DEFINING MULTI-HAZARD INDEXES FOR COMBINED EXTREME EVENTS IN AFRICA.....	67
7.1	BACKGROUND	67
7.2	THE EXTREME CLIMATE INDEX (ECI)	67
7.2.1	<i>Meteorological datasets.....</i>	<i>68</i>
7.2.2	<i>Hydrological component (SPI).....</i>	<i>68</i>
7.2.3	<i>Heat Component (SHI)</i>	<i>70</i>
7.2.4	<i>Wind Component (SWI)</i>	<i>72</i>
7.2.5	<i>Three-component ECI.....</i>	<i>72</i>
7.3	RESULTS.....	74
7.3.1	<i>Examples of SWI analyses of storm footprints.....</i>	<i>74</i>
7.3.2	<i>ECI application for extreme detection.....</i>	<i>76</i>
7.4	SUMMARY	79
	CONCLUSION	80
	BIBLIOGRAPHY.....	81

Tables

Table 1: Observational datasets used in assessment.	11
Table 2: RCM ensembles considered.	12
Table 3: Extreme climate events and impacts in sub-Saharan Africa (adapted from Ayanlade et al., 2022)	25
Table 4: Description of the Copernicus Climate Change Service (C3S) Seasonal Forecast Models.	39
Table 5: Description of precipitation-based indices used in the study.....	39
Table 6: October - March 1993-2017 ENSO and IOD occurrences.	41
Table 7: Classification of the severity of events associated with ECI.	74

Figures

Figure 1: Comparison of CORDEX and CP4A average annual max of daily temperature (TXx) to CPC observations.....	14
Figure 2: EC-Earth's mean temperature bias over the DJF season when compared to the CRU dataset (Taken from deliverable 3.1).....	14
Figure 3: Comparison of CORDEX and CP4A average annual tmin of daily temperature (TNn) to CPC observations.....	15

Figure 4: Comparison of CORDEX and CP4A average annual maximum of daily precipitation (RX1) to CHIRPS observations	16
Figure 5: Projected changes in TXx across the CORDEX models (25 km and 50 km), between the 1975 – 2005 historical period and 2070 -2100 under RCP8.5.	17
Figure 6: Projected changes in TNn across the CORDEX models (25 km and 50 km), between the 1975 – 2005 historical period and 2070 -2100 under RCP8.5.	18
Figure 7: Projected changes in RX1 across the CORDEX models (25 km and 50 km), between the 1975 – 2005 historical period and 2070 -2100 under RCP8.5.	19
Figure 8: IPCC WGI Interactive Atlas - Mean temperature time series for CRU observations (Top) and the CORDEX AFR-44 ensemble (Bottom). The regions used are those in the WGI Reference Regions SEAF (South Eastern Africa), ESAF (Eastern Southern Africa) and WSAF (Western Southern Africa). These were selected as they encompass all regions of interest for the FOCUS project. (Gutiérrez et al., In Press.; Iturbide et al., 2021)	21
Figure 9: IPCC WGI Interactive Atlas - Mean precipitation time series for GPCP observations (Top) and the CORDEX AFR-44 ensemble (Bottom). The regions used are those in the WGI Reference Regions SEAF (South Eastern Africa), ESAF (Eastern Southern Africa) and WSAF (Western Southern Africa). These were selected as they encompass all regions of interest for the FOCUS project. (Gutiérrez et al., In Press.; Iturbide et al., 2021)	22
Figure 10: CORDEX AFR-44 percentage change in mean precipitation by the end of the century under RCP8.5. (Gutiérrez et al., In Press.; Iturbide et al., 2021)	23
Figure 11: Correlation map showing the Spearman's Rank correlation between the CRU 3-month SPI for DJF and the NOAA Niño 3.4 index for DJF, 1984-2013. The stippling represents regions where correlation values are statistically significant at 5% level.	29
Figure 12: Correlation maps showing the Spearman's Rank correlation between individual CMIP model 3-month SPI for DJF with the derived Niño 3.4 index for DJF, 1984-2013. The stippling represents regions where correlation values are statistically significant at 5% level.	30
Figure 13: Same as Figure 12, but for a different set of models.	31
Figure 14: Taylor diagram showing normalised statistical comparison for the CMIP models' DJF SPI-Niño 3.4 correlations, as calculated over the period 1984–2013, over Africa.	32
Figure 15: Correlation maps showing the Spearman's Rank correlation between individual ScenarioMIP model 3-month SPI for DJF with the derived Niño 3.4 index for DJF, 2071-2100. The stippling represents regions where correlation values are statistically significant at 5% level....	34
Figure 16: Same as Figure 15, but for a different set of models.	35
Figure 17: Difference between the future (2071-2100) and historical (1984-2013) derived SPI-Niño 3.4 correlation values for each model	36
Figure 18: Same as Figure 17, but for a different set of models.	37
Figure 19: Monthly standardized anomaly showing positive and negative phases.	40
Figure 20: Seasonal summary of precipitation-based indices; the values are averaged over the hindcast period (1994 to 2017).	42
Figure 21: Spatial distribution of growing season Number of rainy days (NRD) anomaly during ENSO and IOD episodes.	43
Figure 22: Spatial distribution of growing season Number of heavy rainy days (R10mm) anomaly during ENSO and IOD episodes.	44
Figure 23: Spatial distribution of growing season Longest Dry Spell (LDS) anomaly during ENSO and IOD episodes	44
Figure 24: Spatial distribution of growing season Wet-day Intensity Index (WDII) anomaly during ENSO and IOD episodes.	45

Figure 25: Correlation of preceding months ENSO and IOD episodes and rainfall extremes; A) Number of rain days and B) Number of heavy rain days.	46
Figure 26: Correlation of preceding months ENSO and IOD episodes and rainfall extremes; A) Longest dry spell and B) Wet-day intensity index.	47
Figure 27: Location of Lake Malawi “box” and segmentation of the Shire River basin into three regions for analyses of projected rainfall extremes as described in D3.3.	50
Figure 28: Components of plume plots. Each plume represents the spread of the central 90th percentile of a multi-model ensemble.	51
Figure 29: Spatial distribution of mean rainfall, maximum daily rainfall and 95th percentile daily rainfall in ERA5 data between 1979-2021. Superimposed are outlines of Shire River basin and Lake Malawi. Note the scales are not the same in order to better visuali	52
Figure 30: Distributions of rainfall associated with the easterly and westerly regime of moisture influx into the Lake Malawi basin.	53
Figure 31: Distributions of maximum area-average rainfall per year and maximum grid point rainfall per year associated with the easterly and westerly regimes of moisture flow into the Lake Malawi basin.	53
Figure 32: SOM node archetypes for hus,ua,va fields in the NDJFMA season. Illustrated are wind direction and magnitude (arrows) and associated moisture flux (shading). Lake Malawi “box” superimposed in red.	54
Figure 33: Monthly frequencies of SOM nodes illustrated in Figure 33.	55
Figure 34: Frequency of days with easterly and westerly moisture flow regime for each SOM circulation category.	55
Figure 35: Mean, maximum and 95th percentile of area-average rainfall associated with each SOM circulation category.	56
Figure 36: Maximum and 95th percentile grid point rainfall associated with each SOM circulation category.	56
Figure 37: Frequency of high rainfall events associated with each SOM circulation category for area-average rainfall and local rainfall.	57
Figure 38: Maps showing average of quantile of daily rainfall on days on which a given circulation category occurs. Quantiles calculated on grid-point basis from empirical distribution describing daily rainfall (including no rainfall days) over the 1979-2021 period.	58
Figure 39: Plume plots illustrating ranges of total annual rainfall in historical simulations and climate projection under RCP45/SSP245.	60
Figure 40: Plume plots illustrating ranges of total annual rainfall in historical simulations and climate projection under RCP85/SSP485.	61
Figure 41: Plume plots illustrating ranges of 1-day annual maximum rainfall in historical simulations and climate projection under RCP45/SSP245.	62
Figure 42: Plume plots illustrating ranges of 1-day annual maximum rainfall in historical simulations and climate projection under RCP85/SSP585.	63
Figure 43: Plume plots illustrating ranges of 5-day annual maximum rainfall in historical simulations and climate projection under RCP45/SSP245.	64
Figure 44: Plume plots illustrating ranges of 5-day annual maximum rainfall in historical simulations and climate projection under RCP85/SSP585.	65
Figure 45: Examples of empirical distributions for 3-days cumulative maximum daily temperature, along with fitted split-normal distributions.	70-71
Figure 46: Schematic illustration of the three-component ECI in polar coordinates.	74

Figure 47: Footprints of the tropical cyclones Ava (started on 2018/01/05, on the left) and Idai (started on 2019/03/09, on the right), represented through SWI.	75
Figure 48: Daily time series of SWI, median value over Madagascar and surrounding waters. The red line marks SWI = 1.5.....	75
Figure 49: ECI (upper panel) and its three components (lower panels, left to right: SPI3, SHI, and SWI) averaged over January, 2001. The color scale of ECI (upper panel) matches the classification of the intensity of events in Table 7.....	77
Figure 50: ECI (upper panel) and its three components (lower panels, left to right: SPI3, SHI, and SWI) averaged over 1-10 January, 2016. The color scale of ECI (upper panel) matches the classification of the intensity of events in Table 7.	78
Figure 51: ECI (upper panel) and its three components (lower panels, left to right: SPI3, SHI, and SWI) for 25th April, 2019. The color scale of ECI (upper panel) matches the classification of the intensity of events in Table 7.	79

Executive Summary

FOCUS-Africa aims to develop innovative and sustainable climate services in four Southern African Development Community (SADC) sectors: agriculture, food security, energy, and infrastructure. Climate variability, change, and extremes are particularly dangerous for SADC countries. Water resources, agriculture, hydropower generation, ecosystems, and basic infrastructure are extremely vulnerable as the frequency and severity of floods, droughts, and landslides are rising.

In this framework, Work Package 3 (WP3) aims to improve a fundamental understanding of regional climate dynamics at seasonal, decadal, and climate change time scales, with a special emphasis on supporting the creation of valuable and actionable information through case study activities and engagements. More specifically, the goals of this WP can be summarized in three actions:

- the analysis of future climatic conditions based on high-resolution regional climate projections
- the investigation of seasonal and decadal forecasts predictability, analysing the main drivers of climate variability over the SADC region.
- the identification and variability analysis of extreme events and their future distribution in high-resolution climate projections

These objectives were achieved by the work carried out in Task 3.1 (“High-resolution climate projections analysis”), Task 3.2 (“Analysis of the predictability of seasonal and decadal forecasts over the SADC Region”), and Task 3.3 (“Report on the regional extreme events identification and variability”). Task 3.3 described in this report extends the analyses made in Tasks 3.1 and 3.2 by contributing to understanding the impact of climate variability on the quality of seasonal and decadal forecasts over the SADC region in terms of extreme events characterisation.

When evaluating climate models skill in capturing extreme daily events, some Regional Climate Models turn out to be affected by biases and uncertainties. However, this does not justify the exclusion of these simulations from the development of climate scenarios in the SADC region, which would require a more in-depth analysis of the plausibility of the physical processes in the models.

Then, an investigation of new methodologies to determine risks related to climate extremes reveals that Machine Learning can be an efficient method for improving extreme events forecasts.

Furthermore, we analyse the teleconnection between El Niño Southern Oscillation (ENSO) and rainfall over Africa, as well as its changes in the future. As such changes are expected to have great implications for the agricultural sector, we also investigate the impact of rainfall extremes on crops growing season, at a seasonal timescale.

In addition, in a showcase for Lake Malawi, we provide a generalised understanding of the characteristics and synoptic drivers of two types of extremes, namely localized rainfall and area-averaged rainfall.

Finally, we describe the climate risk generated by severe weather events by defining a specific multi-hazard Extreme Climate Index (ECI), particularly efficient in detecting extreme events in the SADC region.

Keywords

Extreme events, seasonal forecasts, decadal forecasts, scenarios, agriculture, teleconnections

1 Introduction

Extreme atmospheric hazards are high-impact weather events caused by processes in the Earth's atmosphere that typically result in significant losses and damages. They can have serious consequences for various sectors in the SADC (Southern African Development Community) region, including energy, water, infrastructure, and food security. Because of the region's extensive linkages and significant interdependence, these impacts are amplified, notably amongst the water, energy, and food sectors. As a large part of the region is already critically vulnerable to droughts, floods, climate variability, and high temperatures caused by extreme events (Ramirez-Villegas et al., 2021), addressing the region's existing and emerging infrastructure-water-energy-food issues necessarily requires a better knowledge of major climate hazards.

In this framework, Task 3.3 aims to contribute to a better understanding of how climate variability affects the quality of seasonal and decadal forecasts in terms of extreme event description and change, taking into account both frequency and intensity. This task will also look into the future distribution and magnitude of extremes in high-resolution climate projections, which is key for the region's adaptation and mitigation efforts. Particular attention is paid to characterizing the dynamics of extreme rainfall in seasonal forecasts and climate projections for the agricultural sector.

This will make use of recently developed methodologies for identifying extreme events, which will build on previously developed specific Extreme Climate Indexes (ECI) and advanced methods for compound, concurrent, and recurring extreme events.

2 Assessing the representation of extreme temperature and rainfall in Regional Climate Model simulations over Southern Africa to inform sectoral applications

2.1 Background on climate risks and trends in Southern Africa

Extreme meteorological events can have significant impacts on key sectors in the SADC (Southern African Development Community) region, such as energy, water, infrastructure, and food security. These impacts are exacerbated - particularly between the water, energy, and food sectors - due to their complex linkages and strong interdependence within the region. With 30% of the region already critically exposed to climate hazards such as droughts, floods, climate variability, and high temperatures driven by extreme events (Ramirez-Villegas et al., 2021), addressing the existing and emerging infrastructure-water-energy-food issues requires a better understanding of key climate hazards in the SADC region.

When looking at the historical climate of Southern Africa, Chapter 9 of Trisos et al. (2022) showed that over the past few decades, the average temperature in Southern Africa has risen by between 1.04°C and 1.44°C, with the annual number of hot days increasing and the number of cold extremes decreasing. For precipitation, due to the limited availability of station data and other factors, it has been hard for studies to detect statistically significant rainfall trends over many regions, with observational datasets disagreeing on the trend direction (Contractor et al., 2020; Panitzet al., 2014). However, in IPCC AR6 Working Group 2 report (Chapter 9 - Trisos et al., 2022), several studies found decreasing precipitation trends in Southern African Winter (high confidence), as well as increased frequency of dry spells / drought and an increase in the number and intensity of extreme precipitation events.

With climate hazards already critically impacting 30% of the region, understanding future projections of extreme events is key for the region's adaptation and mitigation efforts. The latest IPCC report projects the region to experience greater increases in mean temperatures when compared to the global average. This coincides with an increase in the annual number of heatwaves, by up to 12 per year, with a 99 - 100% probability that hot and very hot days will increase under 1.5°C and 2°C global warming. The number of extreme cold and precipitation events is expected to continue to decrease (increase) under all emission scenarios, with the latter resulting in increased exposure to flooding (high confidence).

This section has two purposes: the evaluation of climate model skill in reproducing relevant extreme indices and their analysis of their projected changes under greenhouse-gas forcing scenarios. The indices are based on annual maxima of daily precipitation, daily maximum temperature and daily minimum temperature. These are used as a way to test model's ability of capturing the most extreme daily events and to assess their changes in the future climate, which are not necessarily inferable from the corresponding changes in the changes in the mean (discussed in D3.1).

2.2 Datasets

For this study, we focus on three extreme indices which describe short duration events. From the distribution of annual maxima of 1) maximum daily temperature (TXx) and 2) daily precipitation (RX1) and annual minima of 3) minimum daily temperature (TNn) representing the hottest, wettest, and coldest days of the year respectively, these indices are constructed by averaging over a 30-year historical (1975 – 2005) and future (2070 – 2100) climatological period.

2.3 Observations

Table 1: Observational datasets used in assessment.

REFERENCE DATASET	INSTITUTION	TYPE	SPATIAL RESOLUTION	REFERENCE
CHIRPS	UC	Gridded observations	1420 x 1480, 1440 x 400, 7200 x 2000	Funk et al. (2015)

MSWEP	Princeton University (DCEE)	Gridded observations	3600 x 1800	Beck et al. (2019)
CPC	NOAA (National Oceanic and Atmospheric)	Gridded observations	720 x 360	https://psl.noaa.gov
CRU	Climate Research Unit	Gridded Observations	720 x 360	(Harris et al., 2014)

For daily precipitation, we look at two observational datasets due to the sparsity of *in situ* observations impacting accuracy and reliability. CHIRPS uses satellite and rain gauge estimates and is available at a range of spatial (0.05° to 0.25°) and temporal (6-hourly to 3-monthly aggregates) resolutions (Funk et al., 2015). For this report we use daily precipitation data at the coarser spatial resolution, which supports land surface modelling activities should they be required. MSWEP is the second dataset used and is a combined product which merges rain gauge estimates with ERA5 reanalysis and IMERG satellite data. It has a spatial resolution of 0.1° and a temporal resolution of 3 hours. For daily maximum and minimum temperatures, we selected the CPC Global Unified Temperature dataset which has a 50 km spatial and a daily temporal resolution (Table 1).

2.4 Regional Climate Models and ensembles considered

Table 2 shows the RCM models that were considered in the evaluation of TXx, TNn and RX1, although not all were subject to the full assessment.

Table 2: RCM ensembles considered.

ENSEMBLE	Nº OF ENSEMBLE MEMBERS USED	SPATIAL RESOLUTION	TIME PERIODS AVAILABLE	REFERENCE
CP4A	1	4.5 x 4.5 km	1997 - 2007 & 2095 - 2105	Stratton et al. (2018)
CORDEX AFR-22	7	0.22° x 0.22°	1950 - 2100	Nikulin et al. (2012)
CORDEX AFR-44	22	0.44° x 0.44°	1950 - 2100	Remedio et al. (2019)

2.4.1 CP4A

Climate Predictions for Africa (CP4A) is a climate change experiment at convective scale (4.5km resolution), run by using a convection-permitting model (CPM) over a domain which includes the whole African continent.

The experimental setup for the CP4A simulations (Stratton *et al.*, 2018) is based on an atmospheric-only version of the global model HadGEM3-GC3 (Williams et al., 2018), one of the models developed by the Met Office that contributed to CMIP6 (Coupled Model Intercomparison Project phase 6). This general circulation model (GCM) has been run in the historical period using prescribed sea surface temperature (SST) and sea ice from the Reynolds dataset (Reynolds et al., 2007) at a resolution of 25km. HadGEM3-GC3 has been used to generate the lateral atmospheric boundary condition for CP4A, which uses the same SST and sea ice as its driving model. The simulation was run for the period 1997-2007 (historical period). In the simulation for 2085-2105 (future period), it used average monthly SST changes from the HadGEM2-ES simulation under the RCP8.5 greenhouse gas concentrations pathway with respect to the historical period (1975-2005); it was downscaled using RCP8.5 for the period 2095-2105, corresponding to 2100.

This model was considered and evaluated; however, the small time slices (10 years) are not suitable for extreme annual analysis and is limited in its application to case studies in this project, therefore it has been excluded from this document.

2.4.2 CORDEX

To address an increasing demand for regional climate change information at high spatial resolutions, the Coordinated Regional Climate Downscaling Experiment (CORDEX) initiative was established to provide a consistent approach and framework for generating datasets from downscaling experiments. Originally, this initiative supported the use of RCMs to generate downscaled simulations at a 50 km (CORDEX AFR-44) resolution (Nikulin et al., 2012) based on the general circulation model (GCM) from CMIP5 (Coupled Model Intercomparison Project phase 5) for RCP2.5, RCP4.5 and RCP8.5 (the RCPS for which atmospheric boundary conditions have been distributed). However, recent developments by the WCRP (World Climate Research Programme) CORDEX Common Regional Experiment (CORE) framework produced a new ensemble with a spatial resolution of 25 km (CORDEX AFR-22) across several regions, with a coordinated experiment based on the use of 3 GCMs (NorESM, MPI-ESM-LR/MPI-ESM-MR and HadGEM2-ES, representing, respectively, a low, medium and high sensitivity GCM) and two regional models (REMO2015 and RegCM4-7, cfr., CORDEX-CORE, (Giorgi et al., 2021)), which has been expanded with the COSMO-CLM RCM simulations driven by the same GCMs (Sørland et al., 2021). This assessment will look at both the 50 km and 25 km model simulations.

2.5 Evaluation of extremes from short duration events – historical climatology

Here we assess how well the RCM simulations represent the three selected extreme indices (multiannual means of TXx, TNn and RX1) for historical and future climatological periods. The historical evaluation looks at the CORDEX models where we use a 30-year climatology (1975 – 2005) to evaluate historical performance. To compare these models to observations, all datasets are re-gridded to a common grid (50 km resolution). The CORDEX model projections for the end of the century (2070 – 2100) under a RCP8.5 forcing pathway are compared to the historical climatology.

2.5.1 Maximum Daily Temperature - TXx

Most CORDEX AFR-22 models underestimate TXx over central and southern SADC (Southern African Development Community), with some overestimations, along the Namibian coast (Figure 1). The CCCM-CANRCM4, driven by the Canadian model CCCM, has one of the worst representations, at both the 25 km and 50 km resolutions (the former is the only existing simulation at 25km outside those following the CORDEX CORE experimental design), with far higher TXx values than observed in the southwest and northeast of the SADC region. The REMO2015 downscaled runs all overestimate TXx across most of the SADC except for South Africa, Botswana and eastern Namibia. The final RCM in this subset, CCLM5_0_15, exceeds TXx observations by 2 – 4 °C across much of south and central SADC. Furthermore, the NORESM1_M driven run for CCLM_0_15 and EC_EARTH-RACMO22T exacerbates the cold bias over South Africa and Lesotho, which isn't as prominent in other GCM driven runs. However, all CCLM5_0_15 representations have a strong cold bias over DRC, Rwanda, Burundi, and south Uganda.

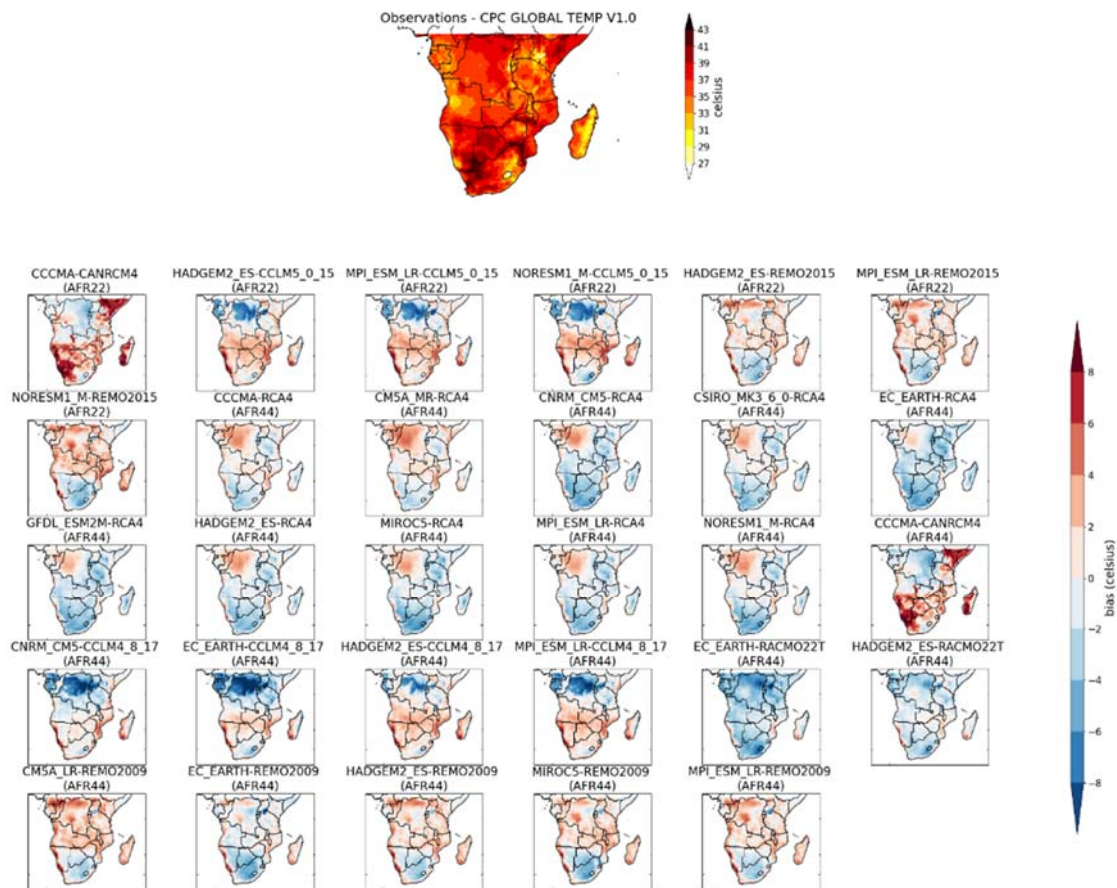


Figure 1: Comparison of CORDEX and CP4A average annual max of daily temperature (TXx) to CPC observations

When looking at the CORDEX AFR-44 models there is an indication of limited added value from the higher resolution dataset, with CCCMA-CANRCM4 runs showing minimal variation between the resolutions. This is also seen between CCLM4_8_17 / CCLM5_0_15, as well as REMO2009 / REMO2015, where large-scale spatial patterns are largely the same across both resolutions. RCA4 and RACMO22T variations all show a strong cold bias across most of SADC, particularly over the countries involved in upcoming case studies. Despite the weak dependence, there is some evidence of GCM influence on model output. For example, EC-EARTH has a particularly cold bias during austral summer when compared to observations (Figure 2). This appears to mute the warm bias seen in RCMs such as REMO2009 and amplify cold bias.

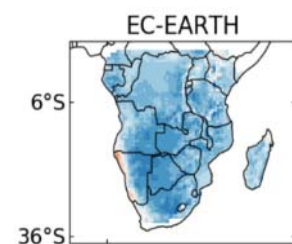


Figure 2: EC-Earth's mean temperature bias over the DJF season when compared to the CRU dataset (Taken from deliverable 3.1)

2.5.2 Minimum Daily Temperature - T_N

Most models overestimate T_N across the SADC region, except for CCCMA-CANRCM4, with the greatest overestimations being seen over DRC (+6 to 8°C) (Figure 3). REMO2009 and REMO2015 downscaled simulations have the greatest hot bias across the region (> 4 °C), whereas CCLM_0_15 has the smallest bias, with most of the case study countries having a bias of +/- 2 °C. RCA4 and RACMO22T also perform better over the case study countries. RCA4 downscaled simulations have a larger warm bias than most over western Tanzania (> 8 °C), and

generally exhibit a slightly warmer bias across the entire region. RACMO22T has a colder bias than most models (excluding CCCMA-CANRCM4), with a lower TNn output along coastal regions and in South Africa. Both CCCMA-CANRCM4 model runs (25 & 50 km resolutions), have a very clear cold bias, particularly over the case study countries (-2 to -6 °C). However, as seen in other simulations, the model doesn't seem to capture TNn over DRC and northwest SADC.

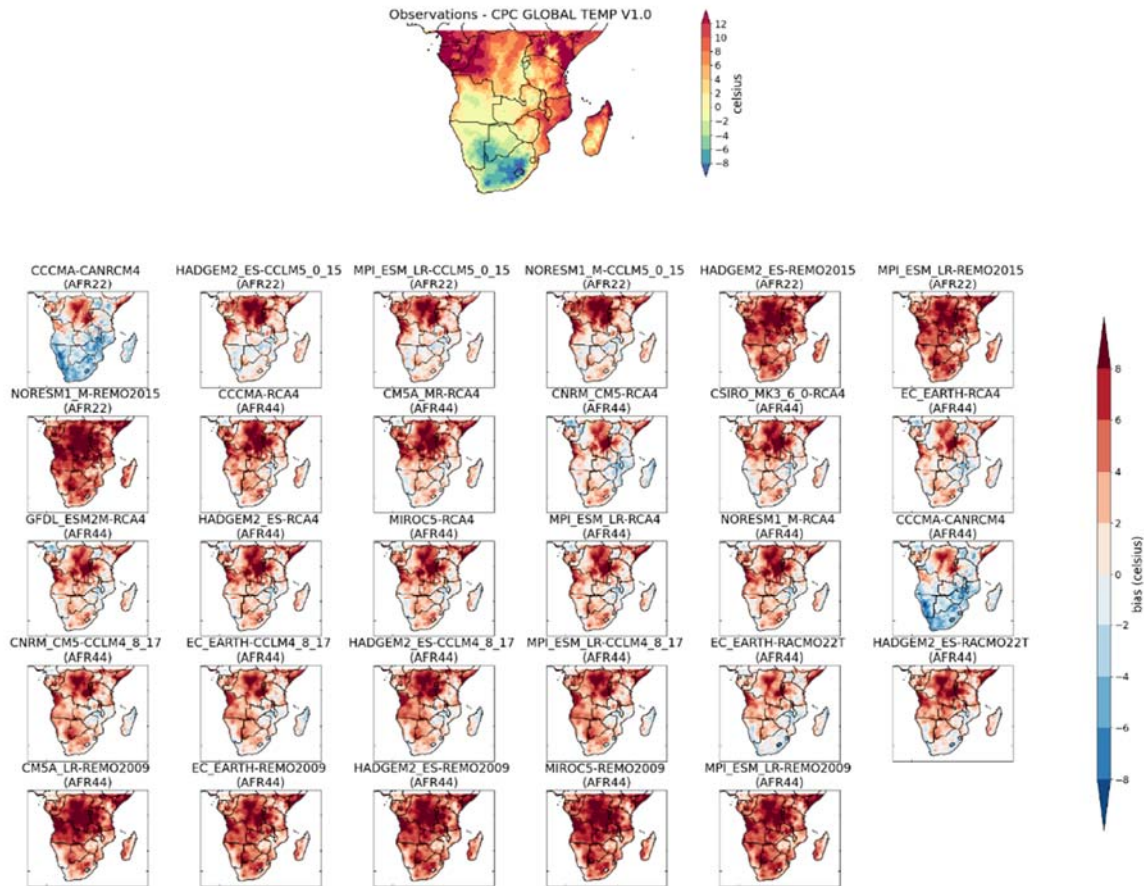


Figure 3: Comparison of CORDEX and CP4A average annual tmin of daily temperature (TNn) to CPC observations

2.5.3 Maximum Daily Precipitation - RX1

Figure 4 includes an additional observational dataset (MSWEP) to account for the sparsity of *in situ* observations impacting accuracy and reliability (top-left panel, Fig 4). The comparison indicates some variability between observations with MSWEP slightly wetter than the CHIRPS dataset (0 to 10 mm day⁻¹), while CHIRPS shows larger precipitation along the Tanzanian and Kenyan coastline (40 to 50 mm day⁻¹). The CORDEX AFR-22 simulations have a wet bias across much of the region, with a slight dry bias over Tanzania and Kenya. The wettest of these simulations is CCCMA-CANRCM4, with many northern parts of the region having a bias exceeding 60 mm day⁻¹. Most of the CORDEX AFR-22 simulations perform slightly better over southern countries with a reduced bias compared to observations. CORDEX AFR-44 has a greater bias range, with RCA4 and RAMCO22T downscaling models having a dry bias in the north and wet bias in south SADC (+/- 20 mm day⁻¹). Both REMO2009 and CCLM4_8_17 have a much wetter bias (like their CORDEX AFR-22 versions), with biases ranging from 20 – 60 mm day⁻¹. CCCMA-CANRCM4 (CORDEX AFR-44) still has a wet bias, but it does display some variation to its higher resolution counterpart, with a reduction in the wet bias intensity across northern and central SADC.

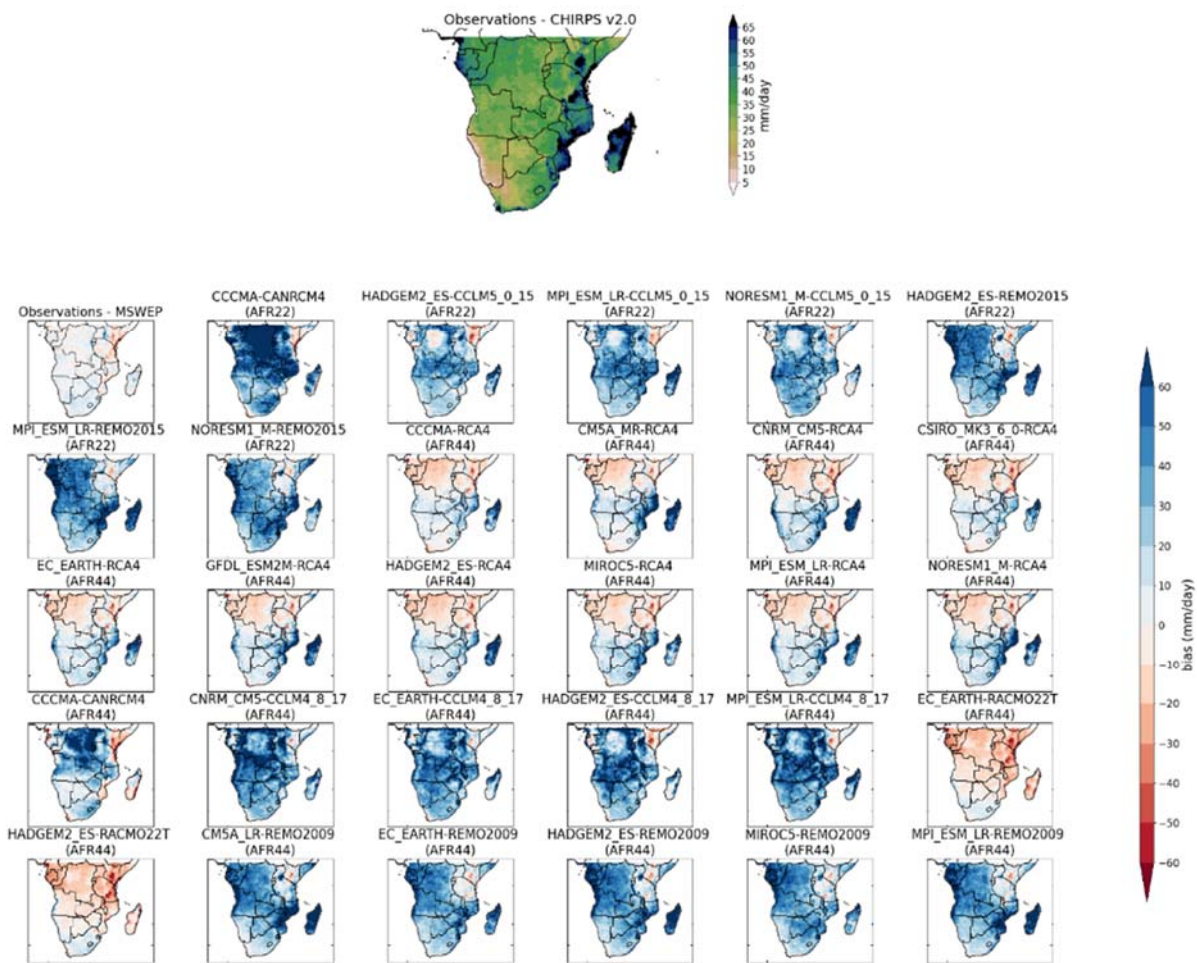


Figure 4: Comparison of CORDEX and CP4A average annual maximum of daily precipitation (RX1) to CHIRPS observations

2.5.4 Conclusion

A common theme amongst the CORDEX models, is weak dependence on the driving GCM models, which has also been noted in other studies (Gnitou et al., 2021; Karypidou et al., 2022). This is evident by the limited variability between all these indices from model runs by each RCM, despite differing driving models. The limited CORDEX AFR-22 ensemble size, coupled with limited variability between RCMs, leads to a reduced representation of uncertainty. This is improved upon through the CORDEX AFR-44 ensemble due to the increased number of RCMs and downscaled GCMs. Despite the apparent strong bias in some indices in this analysis (average TNn in particular), there is no sufficient reason to exclude any of these simulations from the development of climate scenarios over this region. Exclusions would require more extensive analysis on plausibility of the physical processes in the model, without which it is reasonable to assume that similar biases will also be present to an extent in the future projections and likely to be eliminated when estimating climate change responses for these indices from differences between future and historical climate projections.

2.6 Climate change response

Here we assess the projections for the late 21st century compared to the late 20th century, under a RCP8.5 pathway, from the 25 km and 50 km CORDEX ensembles in comparison to the historical climatology. For this analysis we also compare the ensemble averages of the two CORDEX resolutions to help capture the model uncertainties in the future projections under RCP8.5.

2.6.1 Maximum Daily Temperature - TXx

As expected, all models project an increase in TXx (Figure 5). The 25 km and 50 km ensembles produce largely similar projected changes. CORDEX AFR-22 simulations generally project a larger change in temperature over DRC (5 to >8°C) and smaller increases than the CORDEX AFR-44 ensemble along the east coast (2 °C). For individual model results, large temperature increases over DRC are largely driven by the CCLM5-0-15 downscaled simulations. It is also worth noting that those RCM simulations driven by NORESM1_M have a notably lower projected increase, likely due to the low climate sensitivity of this GCM across both mean and TXx variables.

CORDEX AFR-44 projected changes are far more uniform, particularly in the RCA4 downscaled models (Figure 5). CM5A_LR-REMO2009 projects the largest increase in TXx, with values increasing across large portions of SADC by 7 – 8 °C. The smallest increases in temperature are seen from the EC-EARTH and NORESM1_M models, both of which have smaller climate sensitivities within the set of GCMs used in CORDEX (EC-EARTH has a climate sensitivity of 3.1K, Iversen et al. (2013), which is in the middle range of CMIP5 climate sensitivities (Flato et al, 2013) but it is substantially smaller than the climate sensitivity of the “median” model used in CORDEX CORE, MPI-ESM-LR, 3.7K, Flato et al., 2013).

Ensemble means at the two different resolutions are similar in the southern part of the region, while there is a marked increase in response at 25km in the north western part (Figure 5). This increase coincides with the mountains around the DRC, which are more realistically described at 25km resolution, and therefore potentially linked to temperature change amplification at higher altitudes - a robust feature of greenhouse-gas forcing climate change (Mountain Research Initiative EDW Working Group, 2015).

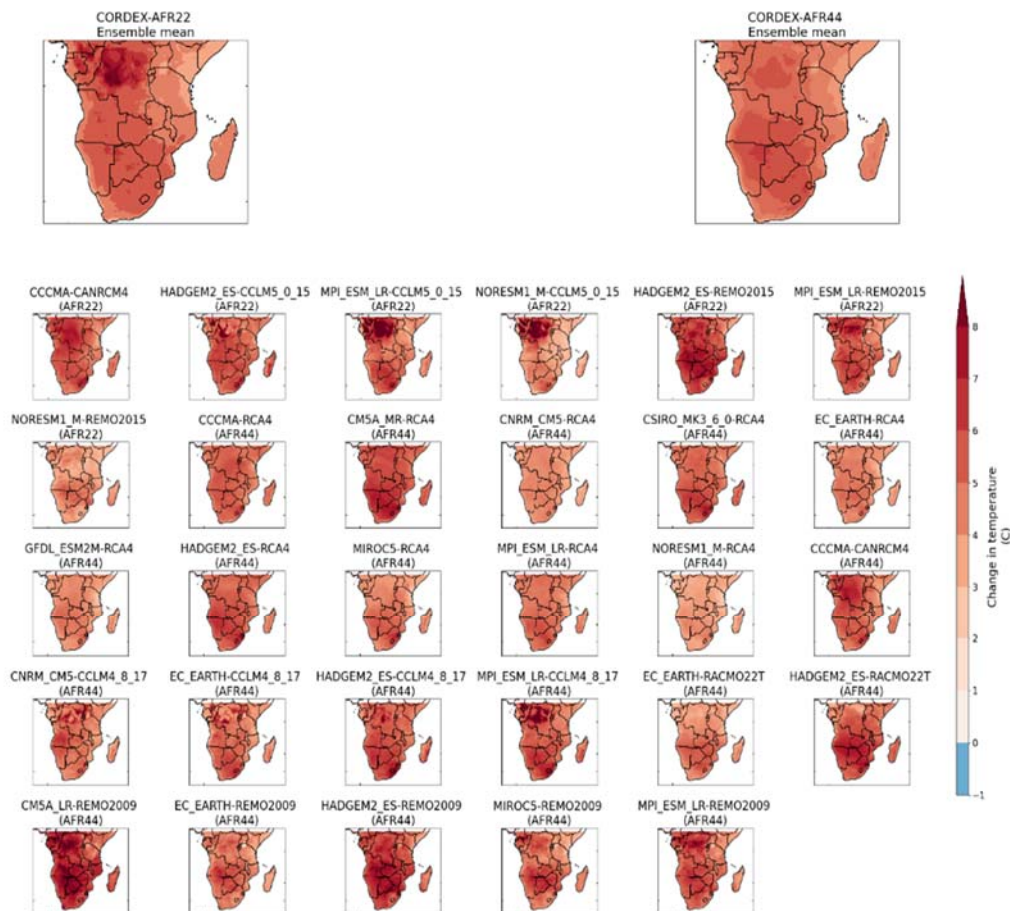


Figure 5: Projected changes in TXx across the CORDEX models (25 km and 50 km), between the 1975 – 2005 historical period and 2070 -2100 under RCP8.5.

2.6.2 Minimum Daily Temperature - T_{Nn}

T_{Nn} also sees an all-round projected increase across all models, with the greatest increase being seen across Namibia, Angola, and Botswana (ensemble average is 4 to 5 °C) (Figure 6). The Western Cape of South Africa sees the smallest increase in T_{Nn} with both ensemble averages projecting an increase of around 1 °C.

The intensity of the climate response for each RCM follows the expected ranking by climate sensitivity of the driving GCM at both resolutions, with specific spatial patterns seemingly related to the RCM formulation and not particularly sensitive to the RCM resolution, even for different versions of the model (e.g. REMO2009 at 50km vs REMO2015 at 25km). The climate response also does not show strong evidence of amplification at higher altitudes seen for mean T_{Xx}, potentially linking this index to larger-scale processes active over wider areas.

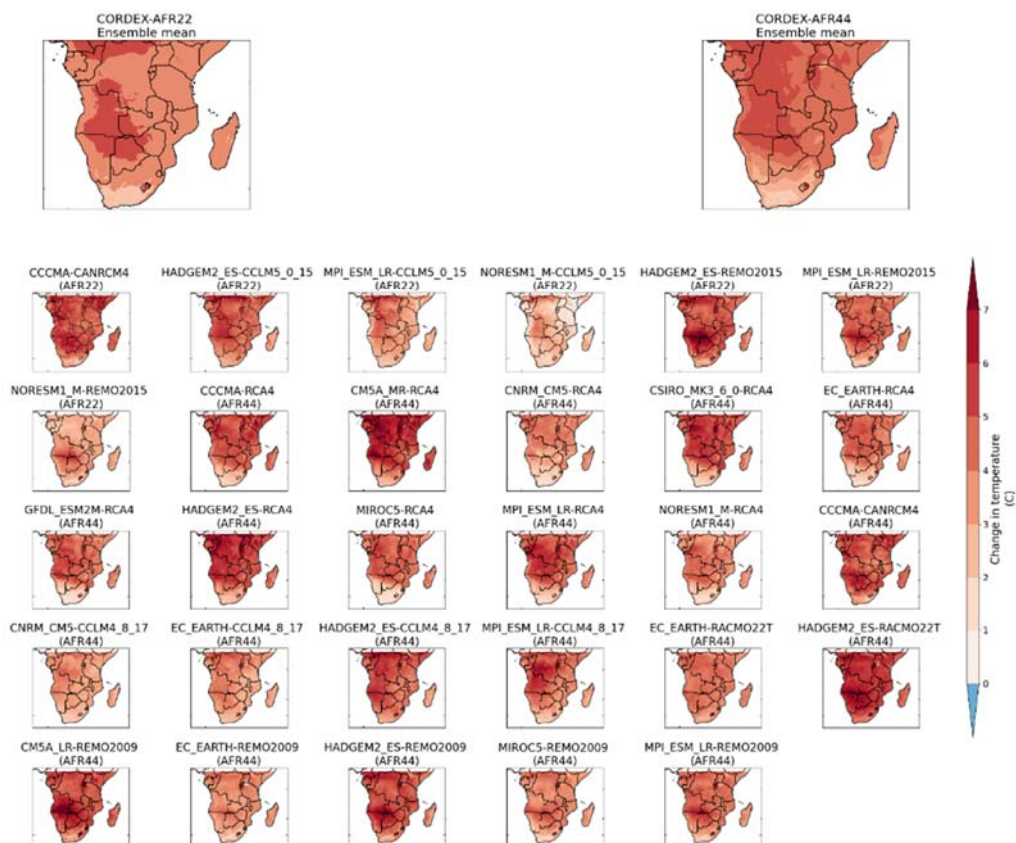


Figure 6: Projected changes in T_{Nn} across the CORDEX models (25 km and 50 km), between the 1975 – 2005 historical period and 2070 -2100 under RCP8.5.

2.6.3 Maximum Daily Precipitation – R_{X1}

The future projections for R_{X1} show larger disagreement across models compared to T_{Xn} and T_{Nn}, with more dramatic changes in R_{X1} seen in the higher resolution CORDEX AFR-22 model ensemble results (Figure 7). Here, a majority of the region is projected to see an increase in rainfall during these extreme events by 10% to 80%. Comparatively the 50 km ensemble shows SADC wide increases, but by 10% to 40%. The 25 km model ensemble also shows a decrease in the R_{X1} value by 10% to 20% along the western coastline of South Africa and Namibian coastline, consistent with a drying trend overall (see section 4.2).

CCCMA-CANRCM4 (25 km resolution) shows the greatest increase in R_{X1} by the end of the century, with a 80 – 90% increase across parts of the region. REMO2015 also projects an increase in R_{X1} across most of the region (30 – 80%). CCLM5-0-15 is the only model to display a strong reduction in R_{X1} across west and southwest SADC (up to 60%), particularly in the NORESM1_M driven model.

CORDEX AFR-44 shows a more diverse range of RX1 changes. Both REMO2009 and CCCMA-CANRCM4 show the greatest increases in this variable. This increase exceeds 60% across large parts of the region, especially along the coastlines in REMO2009. CCLM4_8_17 also shows a general increase; however, the spatial continuity is weak and large decreases are also mixed in with these increases. RCA4 shows a much more uniform spatial representation with a general increase across the region, although the intensity of the increase is lower than other models (10 – 30% in most iterations). RCA4 downscaled models are also the only other simulations to show a clear, repeated decrease in RX1 across the different driving models. This decrease is spatially limited to southern Mozambique (30%) and South Africa (~10 – 20%). The multi-model results, therefore, show patterns of spatial variability in sign and magnitude of climate response: in the context of climate impacts, this result will imply a wide range of realistic outcomes which will need to be considered.

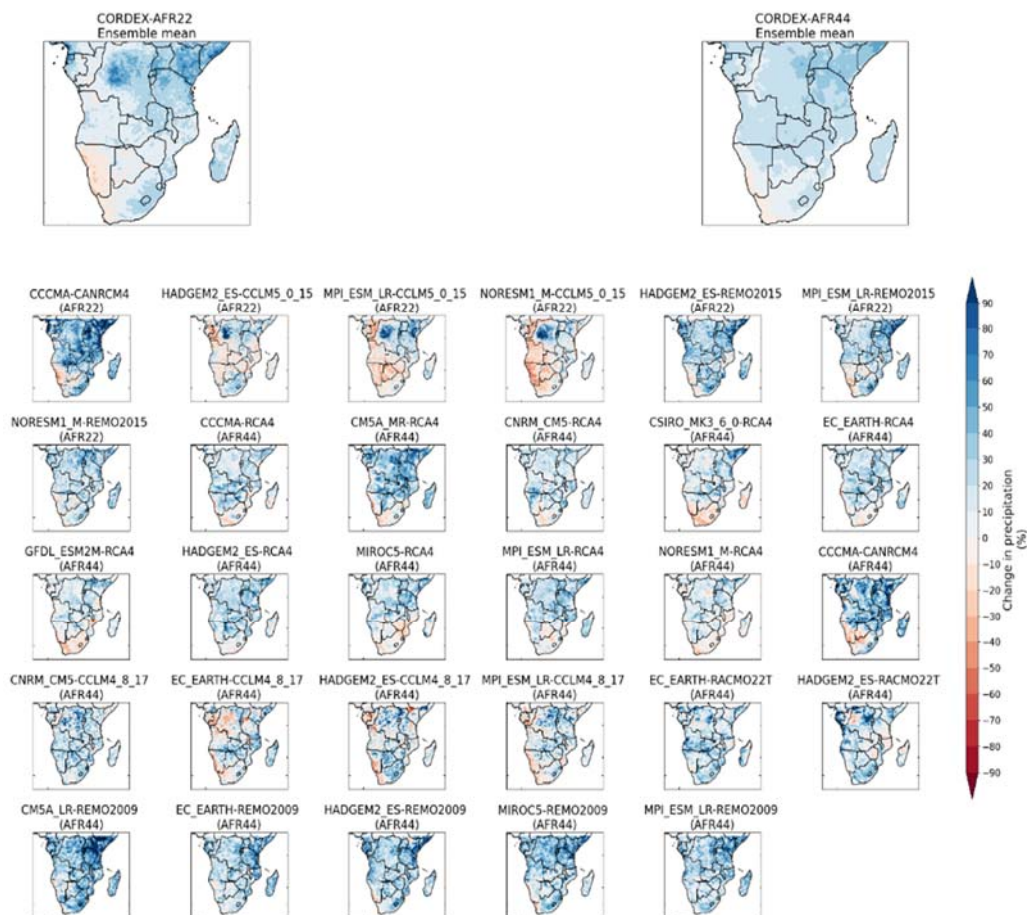


Figure 7: Projected changes in RX1 across the CORDEX models (25 km and 50 km), between the 1975 – 2005 historical period and 2070 -2100 under RCP8.5.

2.7 Evaluation

With no specificity on the required durations provided by end-users coupled with issues surrounding the use of an index that will work across all climatic regions of SADC, this short analysis of long duration events draws on data from Deliverable 3.1 as well as the IPCC AR6 WGI Interactive Atlas and will focus primarily on mean temperature and precipitation changes. This will still feed into case studies and future work, with these changes linking to details on rainy seasons and providing some insight into the potential impact on long duration events. For this study, we have focused on the December – February season, as this is a period associated with higher rainfall and temperatures over case study regions. This follows the same seasonal breakdown used in D3.1.

2.7.1 Mean temperature

In D3.1 we summarised that CP4A's spatial representation of mean temperature was good, but it showed a cold bias of approximately 1 to 3 °C across most of the study countries during this season. The same cold bias was also seen in d3.1 for the CORDEX AFR-22 models, with REMO2015 showing a slight warm bias over parts of Uganda and Kenya. CORDEX AFR-44 was not assessed in this report, but is available through the IPCC WGI Interactive Atlas (Gutiérrez et al., In Press.; Iturbide et al., 2021). By comparing the mean temperature time series over the historical period (Figure 8) we can see that the median value of the model ensemble sits between 22 and 23 °C for the highlighted period, whereas observations fluctuate around 24°. This shows that on average the CORDEX AFR-44 models have a slight cold bias.

When looking at future projections, all CORDEX models were assessed in D3.1 and showed an increase in temperature across the whole of the SADC region. These increases ranged from 2 to 5 °C depending on the region.

2.7.2 Mean precipitation

The average precipitation assessment in D3.1 showed CP4A has a good spatial representation; however, it does have a slight wet bias over the countries of interest regarding monthly rainfall. The CORDEX AFR-22 models also represent seasonal rainfall well spatially and capture mean DJF rainfall in South Africa well. There is a clear dry bias from the CCLM5-0-15 downscaled models along the east coast (~ -150 mm month⁻¹), affecting most case study countries. REMO2015 has a dry bias over Eastern SADC and the GHA, and a wetter bias over southern and southwest SADC.

Again, CORDEX AFR-44 was not assessed for D3.1, therefore we look at the IPCC WGI Interactive Atlas to assess mean precipitation for DJF (Figure 9). For this, we compare to GPCP precipitation data, which oscillates around 3 – 4 mm day⁻¹. Comparatively, CORDEX AFR-44 models range between 3 and 6.5 mm day⁻¹ across the ensemble. When looking at the median value of this ensemble, we can conclude that average precipitation is around 4.7 mm day⁻¹, which would suggest that in general, CORDEX AFR-44 models have a small wet bias compared to GPCP observations.

Future projections for DJF rainfall show large variations across all models with no clear agreement over the SADC region (D3.1), except in the southwest where there is some agreement on a drying trend. Spatial plots from D3.1 shed some light on precipitation change across the assessed models, with CCLM5-0-15 showing a decrease in mean rainfall across large areas of Zambia, Malawi, Mozambique, and Southern Tanzania. This is also seen in the REMO2015 downscaled models; however, the drying is more intense and concentrated around Northern Mozambique. CORDEX AFR-44 was not spatially assessed in D3.1, but using the IPCC WGI Interactive Atlas Figure 10 we see that there is low agreement across the ensemble on the climate change signal for mean precipitation. Figure 9 also includes regions outside SADC, such as South Somalia, which is the only region with some model agreement, with a 50% increase in precipitation projected. However, this is a region with low rainfall during DJF, so the actual change in mm month⁻¹ is minimal.

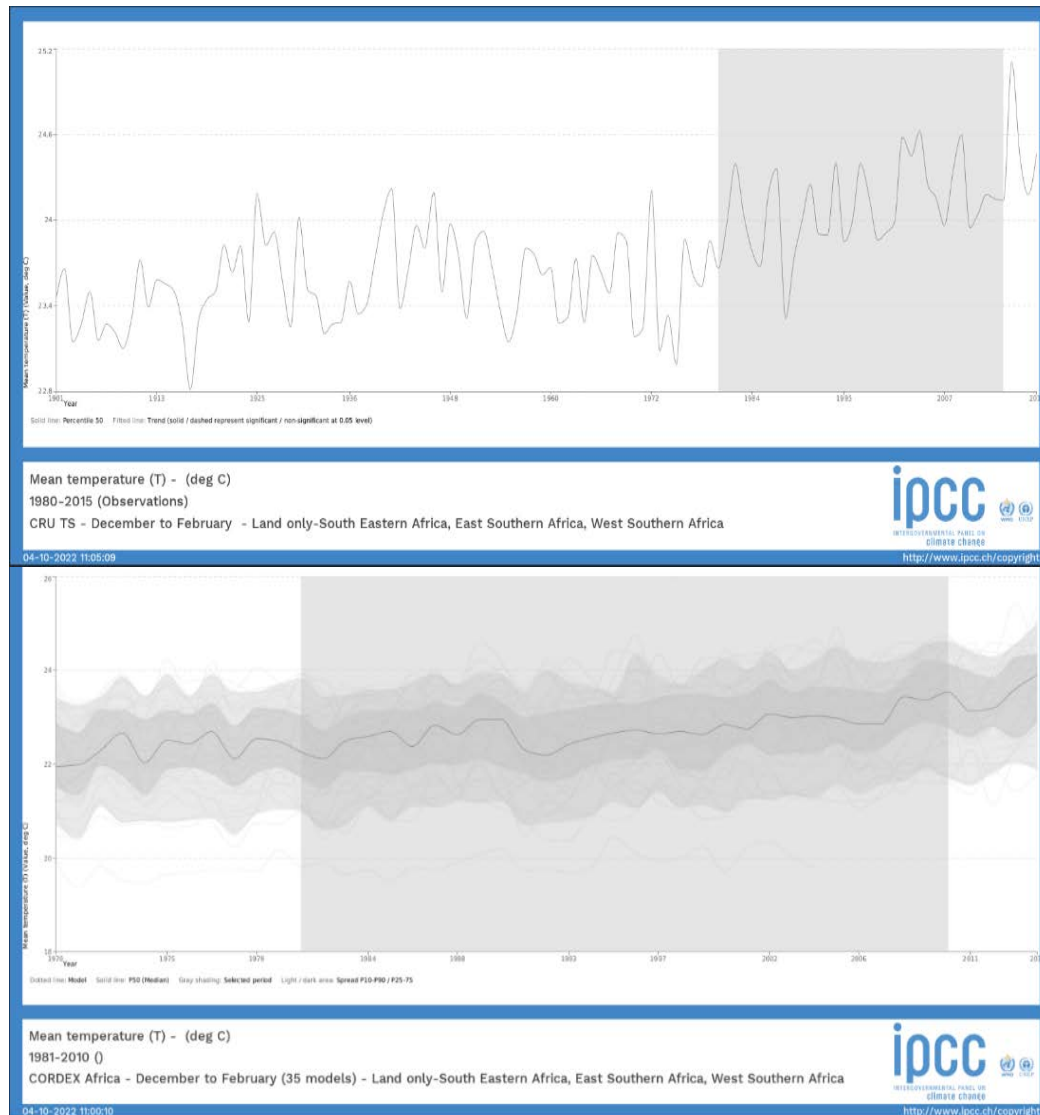


Figure 8: IPCC WGI Interactive Atlas - Mean temperature time series for CRU observations (Top) and the CORDEX AFR-44 ensemble (Bottom). The regions used are those in the WGI Reference Regions SEAF (South Eastern Africa), ESAF (Eastern Southern Africa) and WSAF (Western Southern Africa). These were selected as they encompass all regions of interest for the FOCUS project. (Gutiérrez et al., In Press.; Iturbide et al., 2021)

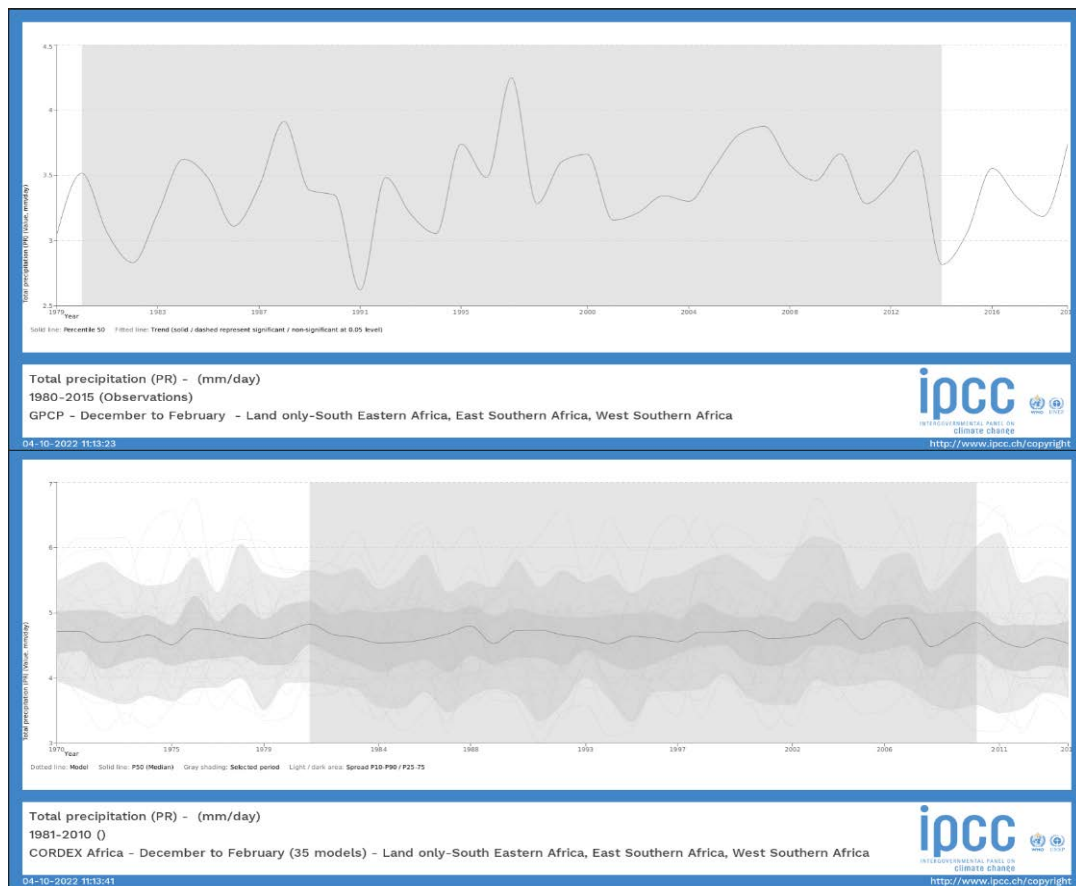


Figure 9: IPCC WGI Interactive Atlas - Mean precipitation time series for GPCP observations (Top) and the CORDEX AFR-44 ensemble (Bottom). The regions used are those in the WGI Reference Regions SEAF (South Eastern Africa), ESAF (Eastern Southern Africa) and WSAF (Western Southern Africa). These were selected as they encompass all regions of interest for the FOCUS project. (Gutiérrez et al., In Press.; Iturbide et al., 2021)

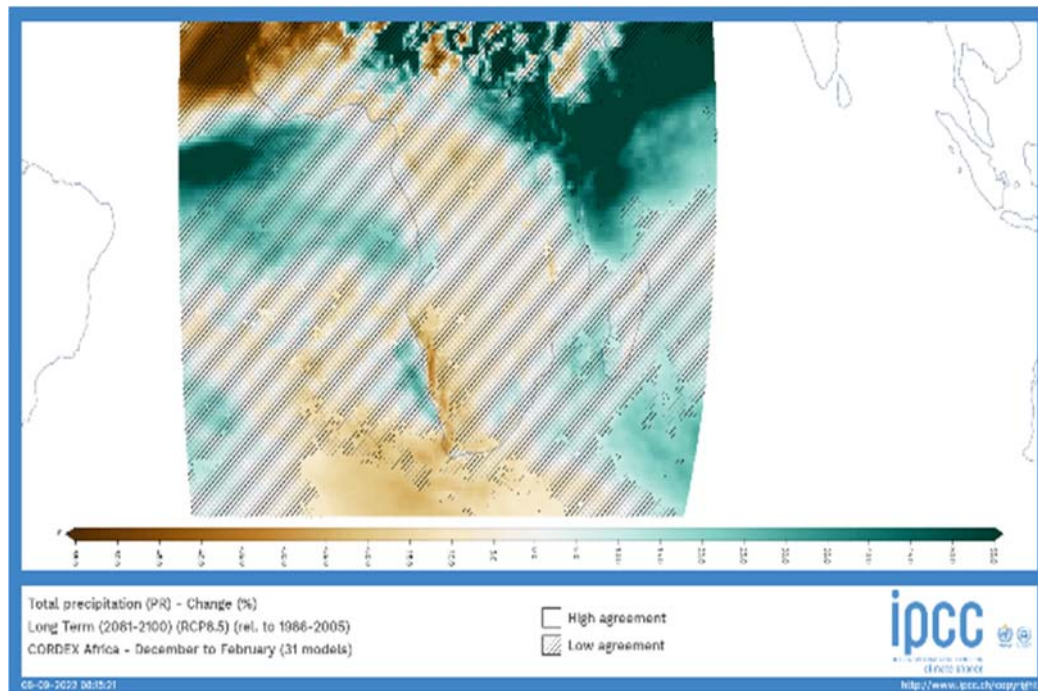


Figure 10: CORDEX AFR-44 percentage change in mean precipitation by the end of the century under RCP8.5. (Gutiérrez et al., In Press.; Iturbide et al., 2021)

2.8 Summary

As expected, the climate change response in mean temperature gives a robust signal of warming with some model uncertainty over the magnitude of change, which could be relevant in impact studies. The precipitation result, however, is characterised by model uncertainty in the whole SADC region. In this case, an increased uncertainty and smaller positive change on long duration extremes are also expected with respect to the results seen for annual RX1, since changes in intensities are expected to increase for shorter duration (e.g., Allen & Ingram (2002)).

3 Review of impacts of climate extremes, including compound events, in agriculture and new methodologies

The undeniable human influence has resulted in changes in weather and climate extremes, with strong evidence that hot extremes (including heatwaves over land and marine heatwaves) have increased and cold events have decreased in every regions assessed in the IPCC AR6 WGI report (Seneviratne et al., 2021). There are clear increases in the frequency and intensity of heavy precipitation events at global scale and in almost every region and increase in agricultural and ecological droughts in almost all regions that are prone to drought. The observed impacts of extreme climate events have intensified in recent years, particularly in Africa, including prolonged dry spells, abnormal rainfall patterns, consequent shortage of water, and heat stress (Chikoore & Jury, 2021; Thoithi et al., 2021). Shifts in average climatic conditions have been observed due to climate change but also due to much more frequent extreme weather events. (Serdeczny et al., 2017; Stuch et al., 2020) show the impact of such extreme events and the threats they pose to agricultural production in the Sub-Saharan Africa (SSA), as well as to urban settlements. Managing the multiple risks of extreme climatic events and disasters in different agro-ecological zones ought to be a research priority in SSA regions, because rural farmers who are already facing hunger and food insecurity (Mbatha Mfaniseni et al., 2021) will be at even greater risk.

3.1 Extreme events and agriculture

Food production is seriously affected by climate variability, and particularly by climate extremes, and food security will be consequently confronted with increasing risks (Wheeler & von Braun, 2013). Deryng et al. (2014) indicate that extreme heat events have a high impact for major producing regions and lower income countries and Semenov (2007) highlights that extreme temperature (either high or low) can seriously harm crops. In addition to the direct effects of heat, drought, and flooding, extreme events indirectly affect crops through pests, changing soil processes and nutrient dynamics (Rosenzweig et al., 2001).

Chatzopoulos et al. (2020) shows that regional climate extremes may have significant economic impacts on agricultural commodity markets. Skilful and reliable predictions are essential for planning given that unfavourable conditions such as heat or water stress affect both grain yield and quality, with large impacts on food security in many regions of the world. Solaraju-Murali et al. (2021) showed that predictions on multi-annual timescales to support decision making in the wheat sector have improved but efforts are still needed to convert those available climate predictions into information that can be understood and used by stakeholders involved in that sector. The assessment of weather impacts on crop production includes not only the focus on changes in the mean values of weather variables but also on the probability, frequency, and severity of extreme events, which substantially influence yields. In addition, many high-impact weather and climate events arise from a combination of multiple drivers and/or hazards such as droughts, heatwaves, heavy precipitation, and storms (Zscheischler et al., 2018). Compound events can be explained when the impact of precipitation extremes are observed, and such impacts can be much more severe if several events occur in close succession (Zscheischler et al., 2020).

Table 3: Extreme climate events and impacts in sub-Saharan Africa (adapted from Ayanlade et al., 2022)

Extreme events	Observed impacts	Most likely affected region in the SSA	References
Drought	Likely increase in agricultural drought occurrence over many regions of SSA with heat over land areas. Likelihood of associated risk of drought becoming noticeable.	Sudan, Sahel, Savanna, Eastern and Southern African highlands	(Ahmed, 2020; Anderson et al., 2021; Dossou-Yovo et al., 2018)
Prolonged dry spell	Higher maximum temperatures are becoming very likely; high likelihood of increasing number of hot days. High probability that dry-spell lengths exceed the normal limit	Sudan, Sahel, both Northern and Southern Guinea,	(Bako et al., 2020; Ojara et al., 2020)

3.2 New methods

As the impacts have been well established by the recent literature, many methods have been used to identify the associated risks. Haqiqi et al. (2021) uses a statistical predictive crop yield model that directly addresses the gap of crop yield impacts due to compound weather extremes, including both dry heat and wet heat. This is made possible by using high-resolution, daily simulated soil moisture data that are consistent with daily temperature data and applied to corn yield data across the continental United States. This study combines a fine-scale weather product with outputs of a hydrological model to construct functional metrics of individual and compound hydroclimatic extremes for agriculture. Supported by statistical evidence, the findings suggest that metrics of compound hydroclimatic extremes are better predictors of corn yield variations than metrics of individual extremes.

Precipitation-related factors present a weaker association with yield anomalies than temperature-related extremes, while irrigation partly mitigates negative effects of high temperature extremes. In order to assess and mitigate climate-related risks to crop production, seasonal forecasts are an important adaptation tool that can assist farmers (Meza et al., 2008). Analysis of temporal clustering, explained as successive occurrence of extreme precipitation events over sub-seasonal timescales can be relevant for hydrology, and therefore, crucial to robustly assess climate risks, particularly high-impact flood events, and water availability. Several studies have focused on these timescales over Europe (Giannakaki et al., 2016; Priestley et al., 2017), California (Neiman et al., 2020) or Pakistan (Martius et al., 2013). Tuel and Martius (2021) give a global perspective of clustering of extremes in sub-seasonal timescales, and find that the Horn of Africa and the Great Lakes region exhibit significant clustering.

The use of artificial intelligence (AI) methods, of which machine learning techniques are part of, for improved forecasts and predictions have increased in the last decade. It can potentially improve such predictions because of its potential to explore very large multi-model forecast and observed datasets more agnostically, to discover emergent patterns in the data, (e.g. Weyn et al. (2021)), instead of first reducing them a priori to limited subspaces and variables as is traditionally done. However, a major challenge is the small size of model re-forecast data used to train the AI method.

By using machine learning models, Beillouin et al. (2020) analysed historical yield data of nine crops (six cereals including winter and spring types, two tuber crops and one oilseed crop) in 17 European countries. When comparing to data from 2018, which was a year that experienced a diversity of atypical extreme climatic conditions, the authors found that it is essential considering single and compound climate extremes to analyse the causes of yield losses in Europe. Statistical and process-based crop models appear to agree on corn yield impacts due to heat (Liu et al., 2016; Tebaldi & Lobell, 2018). However, there is less agreement and greater uncertainty around the crop yield impacts of

hydrologic extremes, due largely to the use of annual or season mean precipitation metrics in statistical models that fail to capture hydrologic extremes (Werner & Cannon, 2016).

Another study that applied a machine-learning algorithm was done by Vogel et al. (2019). The authors analysed the impacts of climate extremes on yield anomalies of maize, soybeans, rice and spring wheat at the global scale using sub-national yield data. They found that climate factors such as mean climate as well as climate extremes observed during the growing season can alone explain 20%–49% of the variance of yield anomalies, depending on the crop types. Similarly, depending on crop type, a large part of the explained variance (18%–43%) can be attributable to climate extremes.

In Africa, Lee et al. (2022) developed an machine-learning-based operational forecast system, aided by satellite datasets, to predict maize yield during the growing seasons for Kenya, Somalia, Malawi, and Burkina Faso. The developed yield forecasting system provided skillful predictions during the growing season, and can support agricultural decision-making processes and food-security planning and management. Although this work was not focused on forecast of extreme events, it does show the potential for such techniques in providing better predictions, and therefore identifying the risks associated with extreme events and the impacts of compound events. The authors suggest that more advanced categorical or probabilistic yield forecasts should be investigated to improve forecasts, particularly in low-yield regions where food shortage is a critical issue.

3.3 Remarks

The use of machine learning has shown to be an effective way for improved forecasts of extreme events in many timescales and its impacts in agriculture. Computationally efficient and able to identify patterns, these techniques can be seen as useful in the context of FOCUS-Africa for improved provision of services, particularly related to prediction of extreme events. However, the work of Lee et al. (2022) also highlight the importance of availability of large datasets that needs be used to train AI methods and improve the applicability of machine learning techniques in forecasts of extreme events in Africa.

Particularly that such techniques depend on the available data to train the AI method, It is essential to point out the need for enhanced in situ observations and measurement of both high quality meteorological variables with appropriate spatial coverage, and also of the impacts. More effort is necessary to improve international coordination of observing system activities as this can has been highly detrimental to the availability of observations, especially over Africa (Santamaria et al., 2021). These observations must be used to monitor changes but also to independently validate predictions, and model skills at different timescales.

Effort could be made to address predictions of extremes in the sub-seasonal timescales as there is high demand and a growing expectation for predictions that go beyond 0–14-day weather forecasts, with a multitude of applications. Gains could be obtained by increasingly developing prediction tools and metrics, particularly using AI and machine learning techniques that strategically target this specific window of opportunity (Mariotti et al., 2020).

One of the new activities under the World Climate Research Programme (WCRP) is the Explaining and Predicting Earth System Change (EPESC) Lighthouse Activity. This new effort to explain and predict annual to decadal-scale Earth system change, and will ensure that advances in fundamental understanding of Earth system change are targeted to meet the needs of decision-makers facing climate-related risks and opportunities. Societal benefits to be delivered by this LHA include early warning of significant global and regional scale changes in the climate system, and quantification of current and future hazard risk on regional scales (Findell et al., 2022). That will include extreme events and hazards in annual to decadal timescales, with a multitude of applications, including infrastructure and agriculture.

4 The ENSO teleconnection to southern Africa in a changing climate

Africa's vulnerability and risks related to climate change are well known and have again been highlighted in the latest Intergovernmental Panel on Climate Change (IPCC) sixth report. Parts of Africa are certain to see an increase in hot extremes and likely also an increase in the frequency and/or severity of agricultural and ecological droughts (IPCC 2021). Southern Africa is projected to become drastically warmer and likely drier under low-mitigation futures due to changes in the extratropical storm track density, the southward shift in mid-latitude cyclones as the earth warms, and increased subsidence over subtropical southern Africa (IPCC 2021). This general pattern of drying can already be discerned under 1.5 °C of global warming (IPCC 2021). Additionally, rainfall events are projected to become heavier over the eastern parts of southern Africa, partially because of the increased amount of moisture in the atmosphere in a warmer regional world (Lenderink and Fowler, 2017; IPCC, 2021). Understanding how extreme rainfall events may change, including seasons of drought or flooding, has important implications for planning in the agricultural and water-security sectors in Africa.

The El Niño Southern Oscillation (ENSO) associated changes in Pacific sea-surface temperatures (SSTs) result in climatic fluctuations in both tropical and extratropical regions of the world via atmospheric teleconnections (Taschetto et al, 2020). ENSO plays an important role in the interannual rainfall variability over many regions of Africa, especially southern, East, and parts of tropical Africa (Nicholson and Kim, 1997; Moeletsi et al., 2011). The ENSO signal is seasonal and results in a dipole rainfall pattern over southern and East Africa. Specifically, during El Niño (La Niña) events southern Africa typically experiences dry (wet) conditions during austral summer, while East Africa exhibits the opposite wet (dry) conditions (e.g. Hoell et al., 2021; Taschetto et al, 2020; Lindesay, 1988). While far less documented, Camberlin et al (2001) noted ENSO also impacts rainfall over the Sahel region during boreal summers, and other parts of the Gulf of Guinea outside this season. Since global climate models (GCMs) provide useful insights into understanding and projecting climate variability and change, accurate representation of features such as ENSO teleconnections are crucial when evaluating these models. Additionally, the performance of GCMs is known to vary spatially in their ability to represent present-day climate, for example, model performance over tropical Africa is relatively weak (Vashisht et al., 2021).

It is also important to understand how the ENSO teleconnection and rainfall will change under future climate change. Climate model projections suggest that increasing global temperatures, driven by greenhouse gas forcing, will result in changes in the mean state of the Pacific Ocean that will likely intensify ENSO-driven precipitation variability in the Pacific and other regions (Taschetto et al, 2020). According to Endris et al (2019), GCM-based projections for the period 2070-2099 indicate an El Niño-like warming pattern over the tropical Pacific Ocean, with the strengthening of the teleconnections to East African rainfall changing during ENSO and Indian Ocean Dipole (IOD) years. A robust signal in both global and regional models is a projected increase in OND East African rainfall, likely driven by SST changes in the Indian and Pacific Oceans (Endris et al., 2019).

Here we investigate how well models in the latest Coupled Model Intercomparison Project Phase 6 (CMIP6) represent the ENSO teleconnection to rainfall in Africa, and examine how this teleconnection might change under future climate change. Rainfall characteristics are analysed using the Standardised Precipitation Index (SPI), which has important applications in the agricultural sector in terms of the objective identification of extremes (periods of drought or above-normal rainfall).

4.1 Data and Methods

Monthly precipitation (pr) and surface temperature (ts) data for 42 CMIP6 models is used in this investigation. The 42 models were selected based on the availability of data for both variables (pr, ts) and for both CMIP historical simulations and ScenarioMIP (SSP 5-8.5, low mitigation) projections. SSP 5-8.5 was selected as scenario as this contains the strongest warming signal by the end of the century, and therefore likely has the strongest regional climate change signal. In order to analyse the performance of the CMIP6 models, a comparison with observational data is undertaken. A comparison with in-situ observations would be ideal; however, this is not possible given the uneven spatial distribution of stations in Africa and the sparsity of records. Hence, the gridded dataset of the Climatic Research Unit (CRU) is used; specifically, the latest Time-Series (TS) version (CRU TS v. 4.05) precipitation data. This is a station-based time-series available for the period 1901-2020, at a 0.5° resolution, at a monthly timescale (Harris et al., 2020). In order to investigate the ENSO teleconnection to rainfall in Africa, the National Oceanic and Atmospheric Administration (NOAA) Niño 3.4 index (NOAA, 2022) is used, as described below.

There is ongoing debate and discussion around which drought indices are preferable in climate research and the suitability of these indices to specific case studies/applications. The Standard Precipitation Index (SPI) is a widely used drought index, that is endorsed by the World Meteorological Organisation (WMO) and is simple in its calculation given that it only requires precipitation as an input parameter. Another advantage of the SPI is that it can be calculated for different timescales (WMO, 2012). The SPI is calculated by taking a long-term precipitation record and fitting it to a probability distribution, which is then transformed into a normal distribution, centering the mean SPI on zero (Edwards and McKee, 1997). This enables an easy interpretation of the SPI: positive values indicate above-median precipitation (i.e. wet conditions) and negative values indicate below-median precipitation (i.e. dry conditions) (Edwards and McKee, 1997). We calculate the 3-month SPI for the CRU dataset and for each of the 42 CMIP6 models, for both the historical and future simulations, for each grid point over Africa. For CRU and the historical CMIP simulations, the period 1984-2013 is investigated. For future ScenarioMIP simulations, we examine the end of the century, 1971-2100.

In order to investigate the rainfall dynamics over Africa, the models' ability to represent the ENSO teleconnection is considered by correlating the SPI with sea-surface temperature (SST) anomalies. All correlations are based on the Spearman's Rank Correlation coefficient. To establish a baseline relationship, CRU SPI is correlated with the NOAA Niño 3.4 anomalies. The Niño 3.4 anomalies are calculated relative to the same baseline period used in the SPI calculation, namely 1984-2013. For each of the CMIP6 models, the area-averaged surface temperature for the Niño 3.4 region (5N-5S, 120W-170W) is calculated and the anomalies are derived. For the historical CMIP simulations, the anomalies' reference period is 1984-2013 and for the future ScenarioMIP simulations the reference period is 2071-2100. Given that the ENSO signal peaks during the December-January-February (DJF) season, each model's DJF SPI is correlated to its own calculated DJF Niño 3.4 anomalies.

Finally, the pattern correlation between each CMIP6 model and CRU correlation values, along with root mean square error (RMSE) and standard deviation of the models normalised by the CRU standard deviation (Taylor, 2001) are used to quantify how well the correlation between the SPI and Niño 3.4 index is represented by the models.

4.2 Results

The initial investigation into the ENSO-SPI correlation during DJF is done using observations (Figure 11). The well-known dipole relationship is well-captured, with negative correlations over southern

Africa representing dry (negative SPI) conditions during an El Niño (positive Niño 3.4) and positive correlations over East Africa representing wet (positive SPI) conditions during an El Niño (positive Niño 3.4), and the reverse captured for La Niña (negative Niño 3.4). Larger regions over southern Africa have a statistically significant relationship (at 5% significance level), than East Africa (Figure 11). The ENSO signal is relatively weak over northern Africa and the Sahel. Interestingly, there is a small region over tropical West Africa that shows a statistically significant relationship of dry (wet) conditions during El Niño (La Niña) (Figure 11).

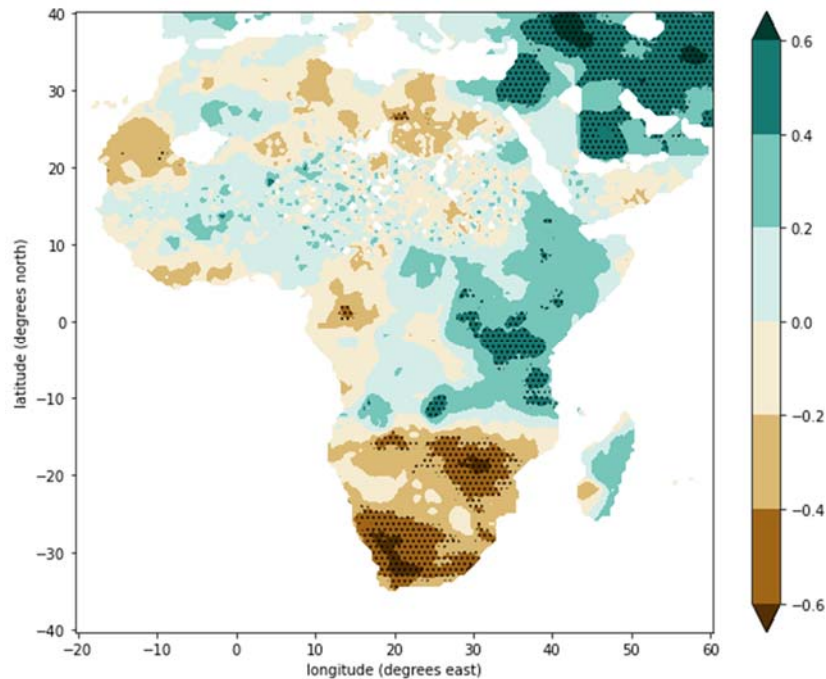


Figure 11: Correlation map showing the Spearman's Rank correlation between the CRU 3-month SPI for DJF and the NOAA Niño 3.4 index for DJF, 1984-2013. The stippling represents regions where correlation values are statistically significant at 5% level.

Considering the historical CMIP model runs, most models capture well the observed dipole (Figures 12 and 13). Compared to the observations, the East Africa domain shows larger regions with a statistically significant relationship, which suggests most models have a relatively strong signal of wet (dry) conditions over East Africa during an El Niño (La Niña). Interestingly, half the models show a statistically significant positive correlation over the Sahel/North-West Africa domain, representing wet conditions (positive SPI) during El Niño (positive Niño 3.4) and dry conditions (negative SPI) during La Niña (negative Niño 3.4) (Figures 12 and 13). Compared to observations, several CMIP6 models do seem 'overconfident' in terms of the strength and spatial extent of the ENSO teleconnection to rainfall in East Africa, tropical Africa and the Sahel/North-West Africa.

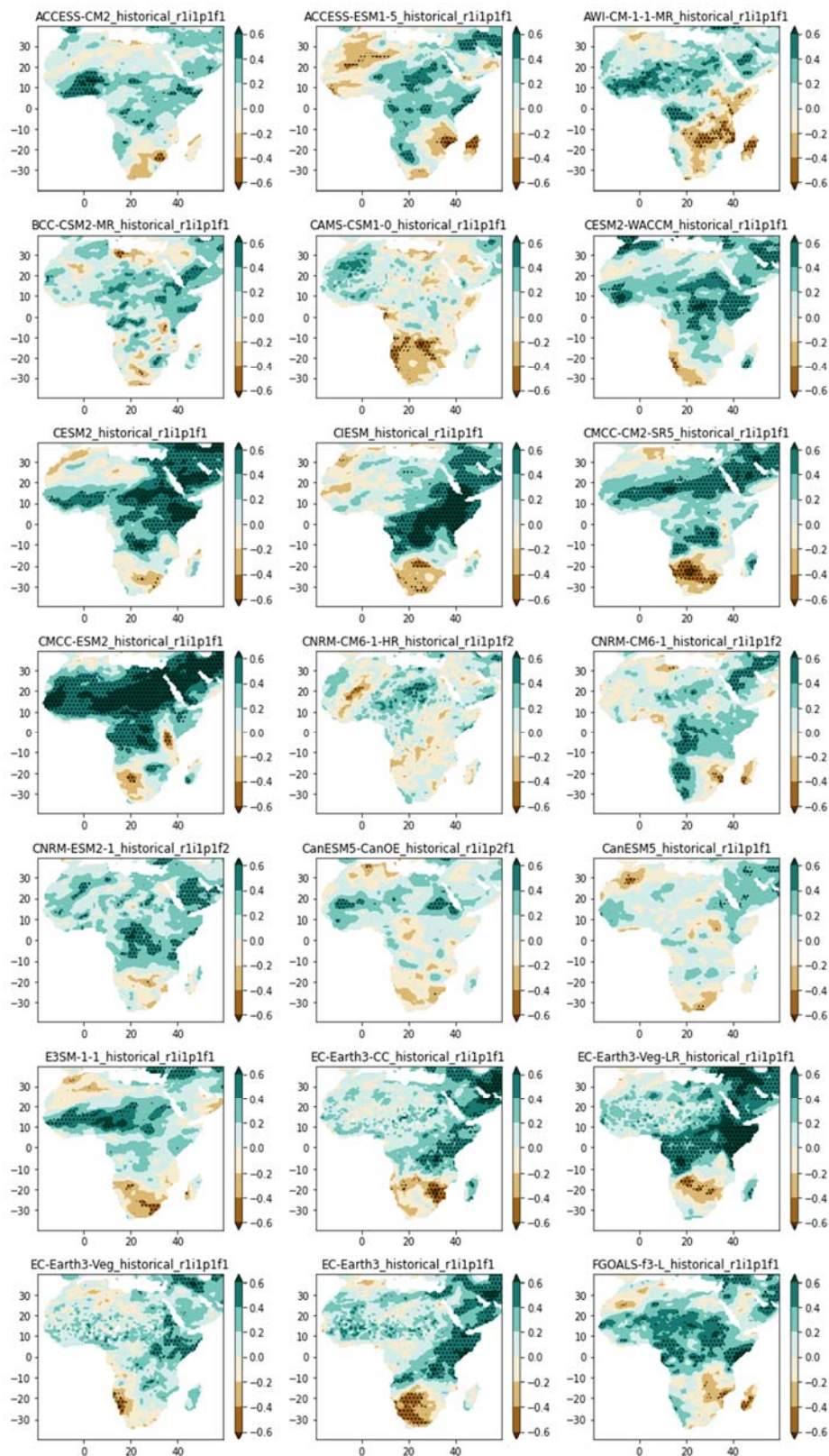


Figure 12: Correlation maps showing the Spearman's Rank correlation between individual CMIP model 3-month SPI for DJF with the derived Niño 3.4 index for DJF, 1984-2013. The stippling represents regions where correlation values are statistically significant at 5% level.

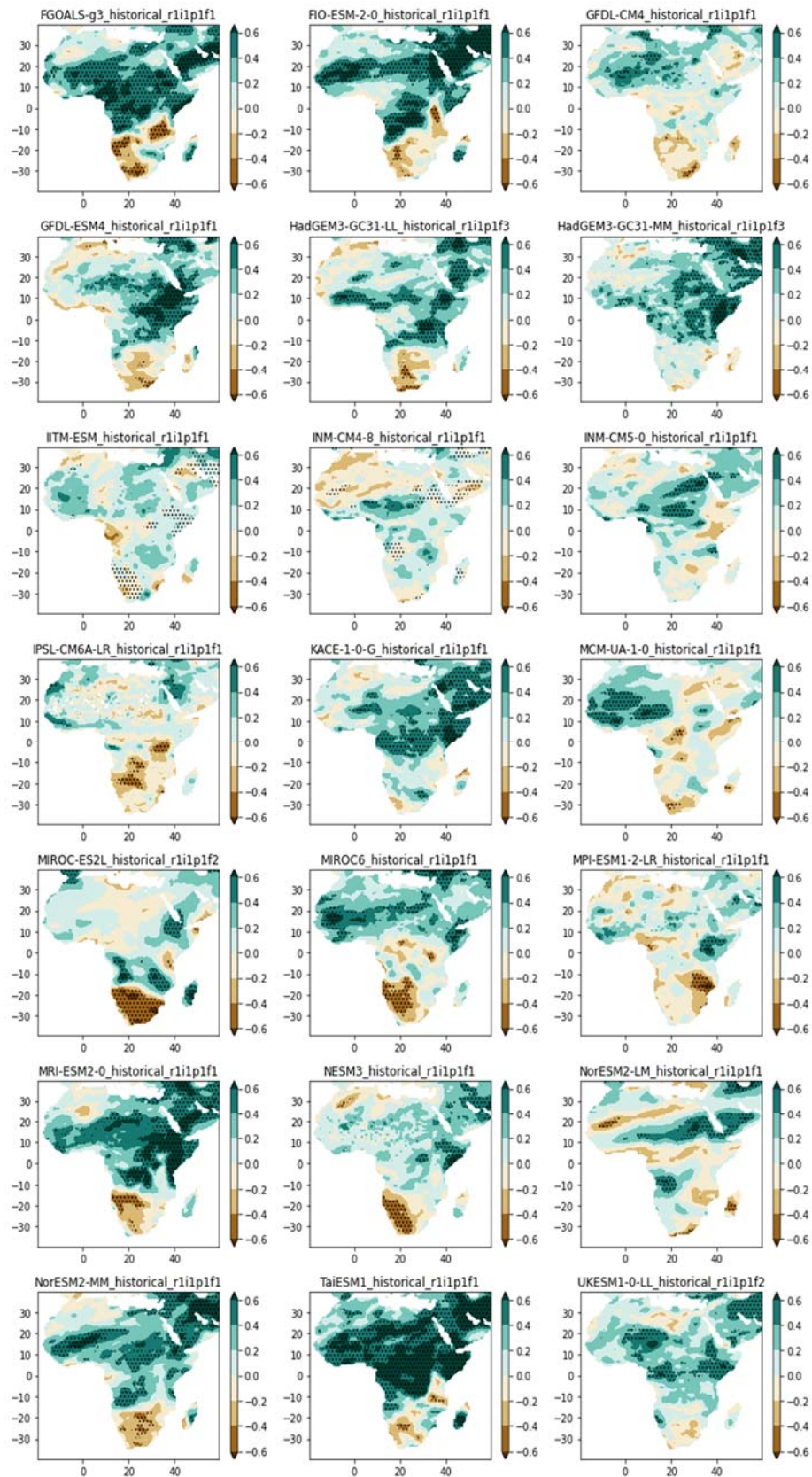


Figure 13: Same as Figure 12 but for a different set of models.

To better understand the performance of these models, the Taylor diagram (Figure 14) summarises how well each model captures the correlation between Niño 3.4 SSTs and the spatial patterns of

rainfall across Africa, in comparison to the observed correlations. The pattern correlations range between 0.02 and 0.67, indicating large variability in the level of agreement between the SPI - Niño 3.4 correlation values in individual models and observed data. Some models normalised standard deviations are very close to 1, indicating a similar spatial variation of the spatial correlations of the model simulations compared to observations. However, overall more models have a lower (rather than higher) standard deviation than observations, which suggests reduced spatial variability in the models (Figure 14).

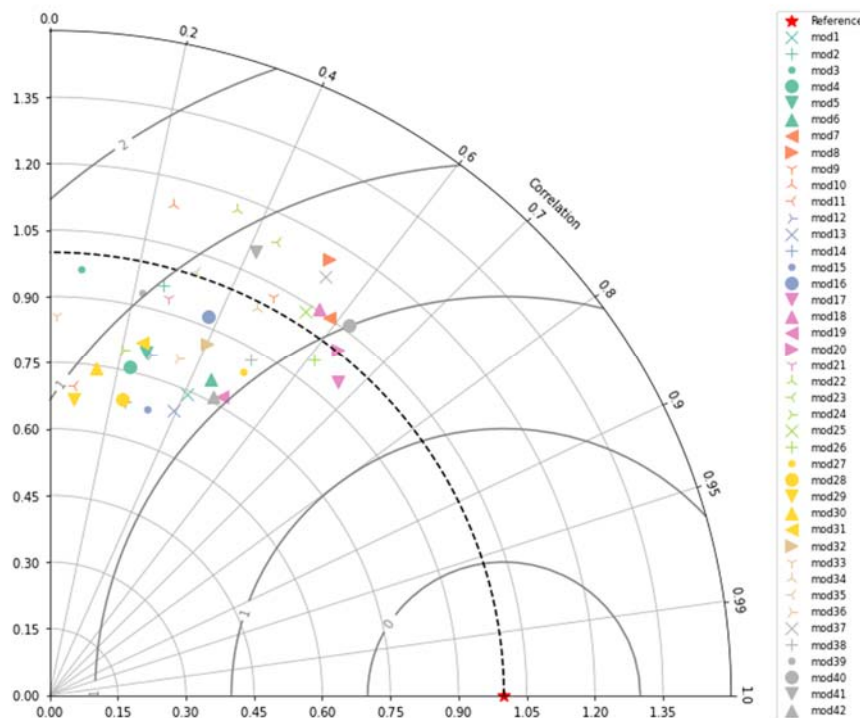


Figure 14: Taylor diagram showing normalised statistical comparison for the CMIP models' DJF SPI-Niño 3.4 correlations, as calculated over the period 1984–2013, over Africa.

Examining the future ScenarioMIP simulations for each model, most (60%) models maintain the dipole pattern in a changing climate, with some notable differences also present (Figures 15 and 16). In some cases, for example CESM2-WACCM, CNRM-ESM2-1, E3SM-1-1 and MIROC6, the dipole pattern becomes stronger and more statistically significant in the future (Figures 12, 13, 15 and 16). On the other hand, CIESM indicates a weakening of the ENSO signal in the future (Figures 12 and 15). Another notable change is evident in MIROC-ES2L and NorESM2-LM simulations (Figure 13), where the negative correlation over the Horn of Africa changes to a statistically significant positive correlation under climate change (Figure 16), indicating a strengthening of the ENSO signal. Significant positive SPI - Niño 3.4 correlations are projected over tropical and north-western Africa in four models (CMCC-CM2-SR5, CMCC-ESM2, FGOALS-g3 and FIO-ESM-2-0, Figures 17 and 18).

How the SPI – Niño 3.4 relationship is projected to change, is further examined by subtracting the historical simulation correlations from the future simulation correlations (Figures 17 and 18). In these figures, the positive (red) values represent regions where the correlation between SPI and Niño 3.4 changes 'more positive', and the opposite is true for negative (blue) values, which indicate a change to correlations becoming 'more negative'. Values close to zero represent little to no change. Therefore, negative values over southern Africa indicate the expected pattern of dry (wet) conditions during an El Niño (La Niña) are stronger under future climate change, for example, in models KACE-1-0-G and MIROC6 (Figure 18). Similarly, positive values over East Africa indicate the expected pattern

of wet (dry) conditions during an El Niño (La Niña) is stronger in the future simulations, for example, in models AWI-CM-1-1-MR, E3SM-1-1, FGOALS-g3 and NorESM2-LM (Figures 17 and 18). There are some noteworthy positive values over southern Africa (for example, CMCC-CM2-SR5 and TaiESM1, Figures 17 and 18) which suggests the correlation changes from the expected negative to less negative correlation values, which indicates a weakening in the classical ENSO signal.

4.3 Summary

This investigation has provided valuable insights into how well the CMIP6 models represent the ENSO teleconnection to rainfall over Africa and how this teleconnection is projected to change in the future. Across the 42 analysed models, there is variability in how closely the correlations between the SPI and Niño 3.4 indices relate to the observational correlations. Overall, the models do well at capturing the austral-summer dipole relationship observed over southern and East Africa during El Niño (southern Africa dry, East Africa wet) and La Niña (southern Africa wet, East Africa dry) events.

There is much regional variation in how the correlations between the SPI and Niño 3.4 index are projected to change under future warming and further analyses of these changes by region is required. While many models did project a strengthening of the relationship under future climate change, some models indicate a weakening or even a reversal of the expected DJF rainfall signal over southern Africa during El Niño/La Niña events. Such changes will have major implications for the agricultural sector. For example, considering maize production in the Free State Province of South Africa, Moeletsi et al (2011) found production was lower during El Niño years and favourable during La Niña years, but this relationship could change. Inconsistencies between model projections are not uncommon and Endris et al (2019) found the frequency and intensity of ENSO/IOD increased in some GCMs, decreased in some and remained similar in others. Future work will therefore focus on quantifying the probability of the ENSO signal changing across various regions in southern Africa, noting that the analysis undertaken here already indicates the most likely future: the ENSO signal will remain similar in sign than the present-day, but with a potential increase in the amplitude of impacts. The research undertaken here is relevant to the FOCUS Africa case studies across South Africa, Malawi and Tanzania, given the strong ENSO signal evident in particular over the summer rainfall region of South Africa and Tanzania.

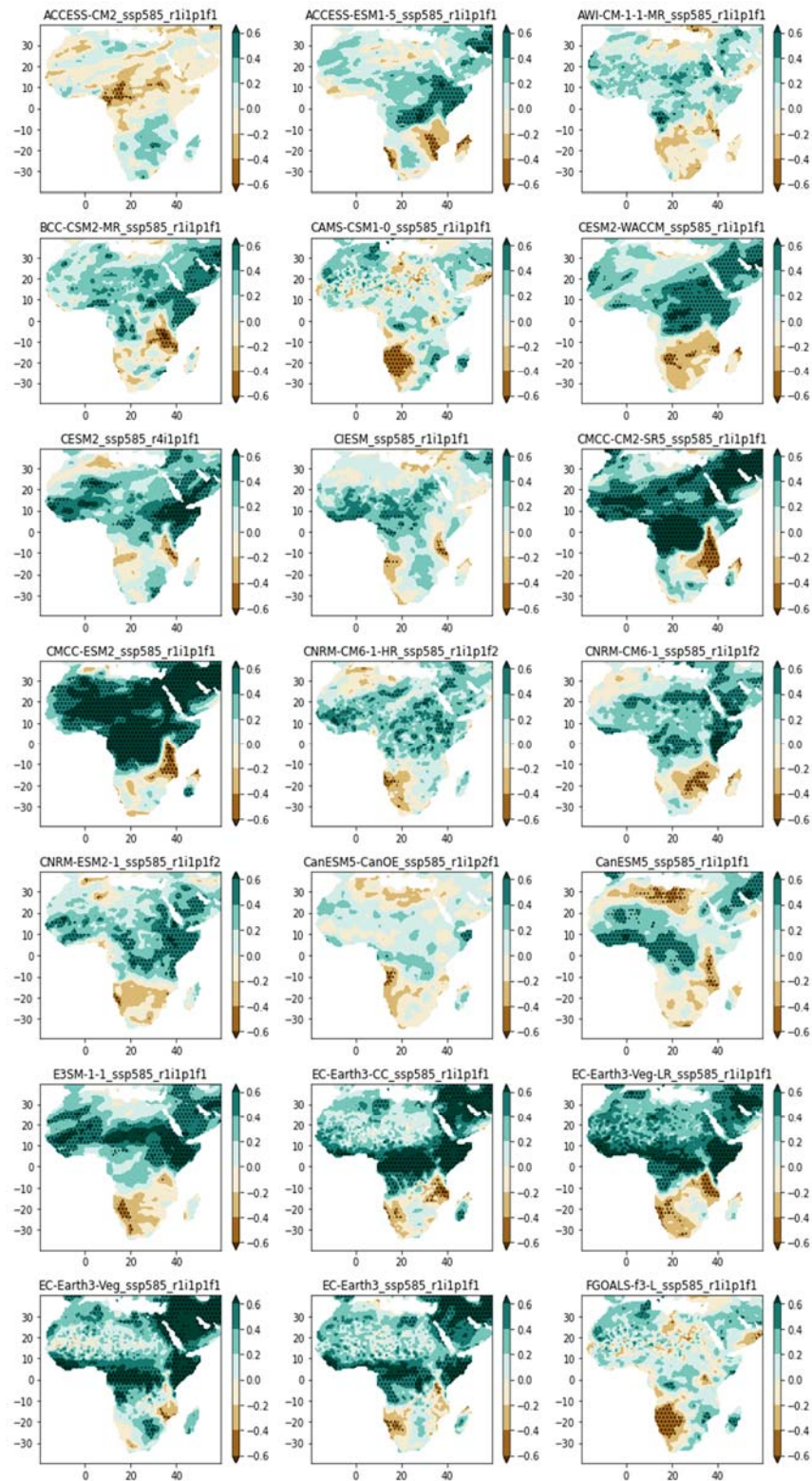


Figure 15: Correlation maps showing the Spearman's Rank correlation between individual ScenarioMIP model 3-month SPI for DJF with the derived Niño 3.4 index for DJF, 2071-2100. The stippling represents regions where correlation values are statistically significant at 5% level.

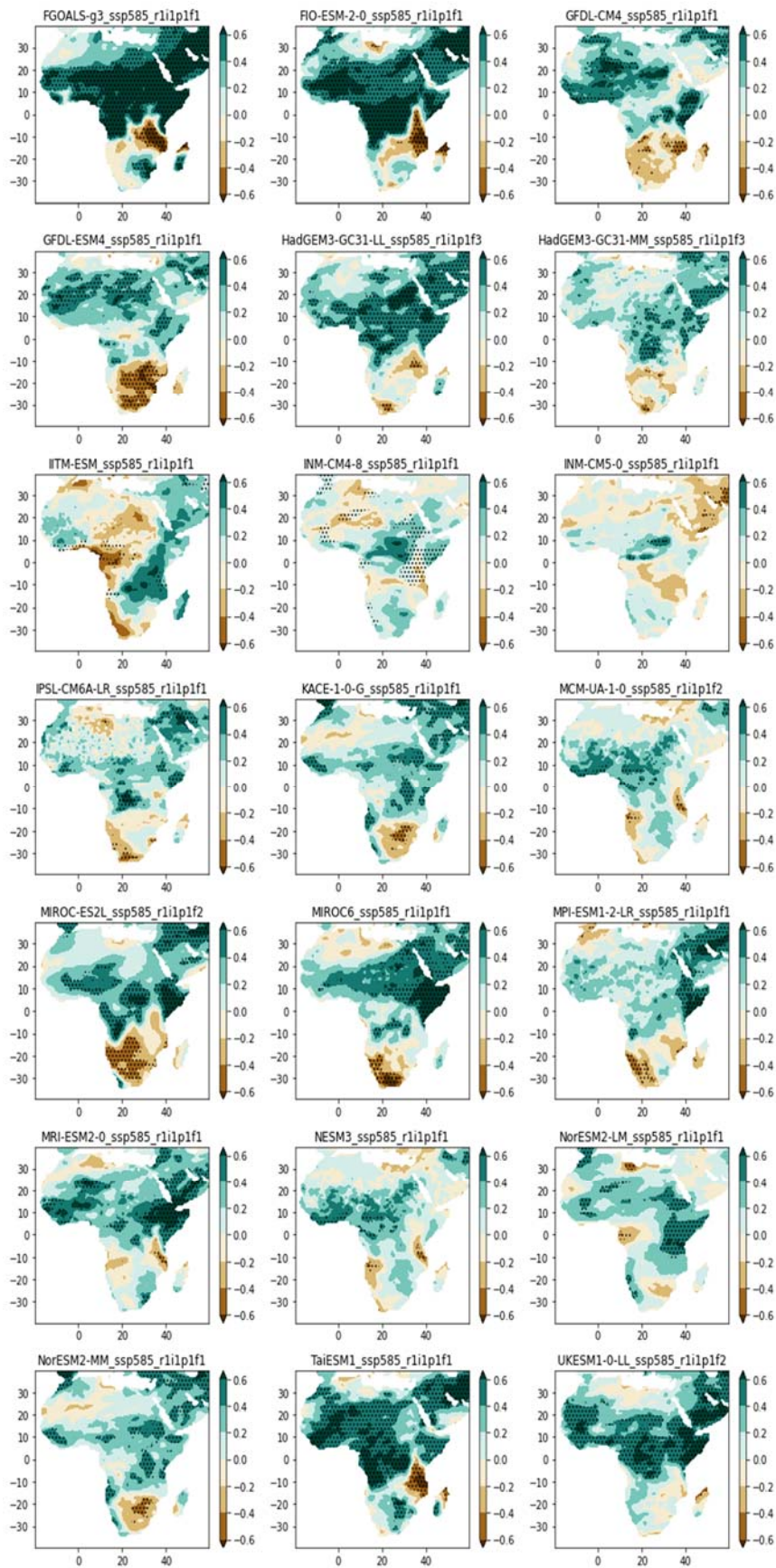


Figure 16: Same as Figure 15, but for a different set of models.

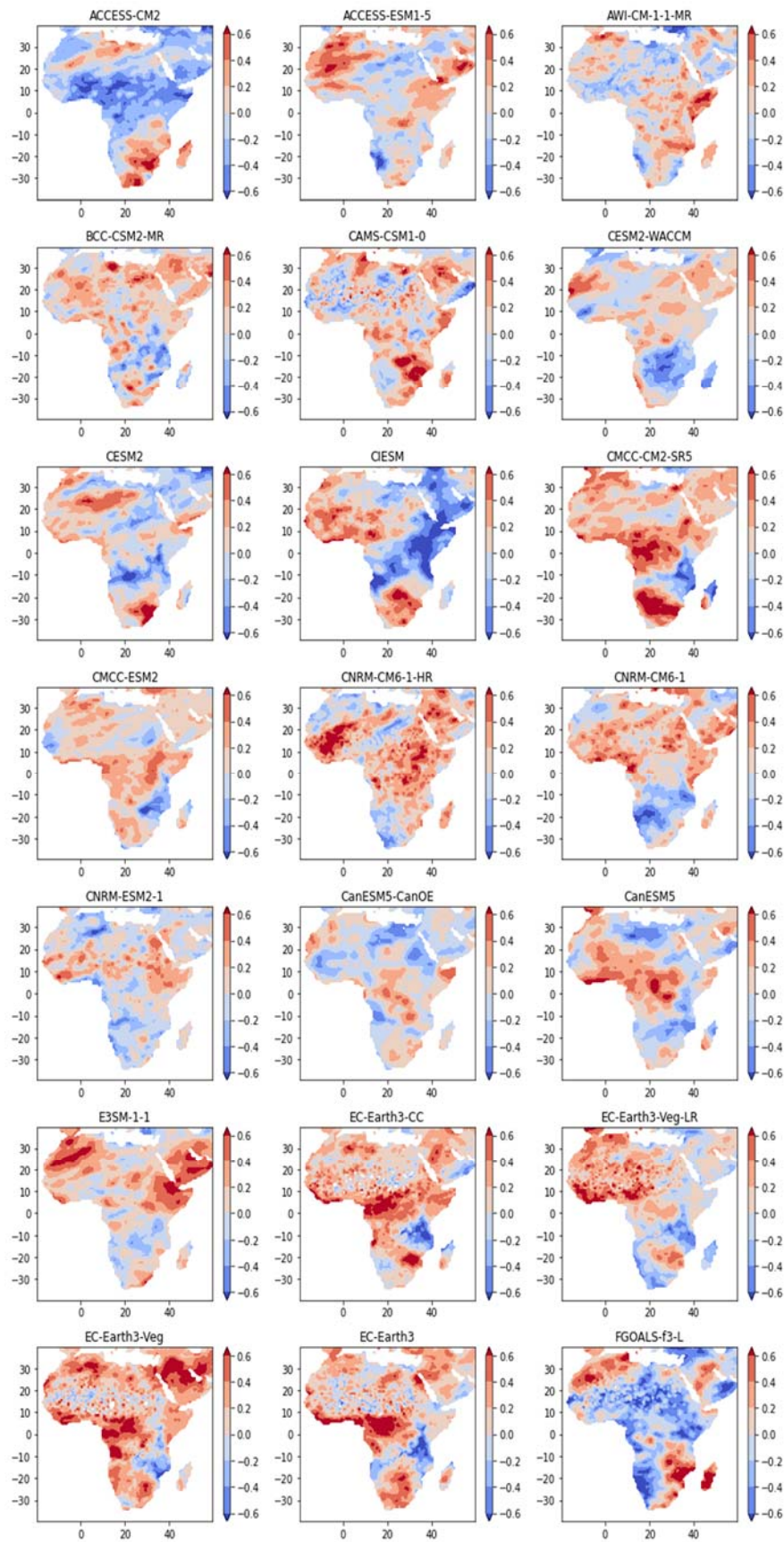


Figure 17: Difference between the future (2071-2100) and historical (1984-2013) derived SPI-Niño 3.4 correlation values for each model

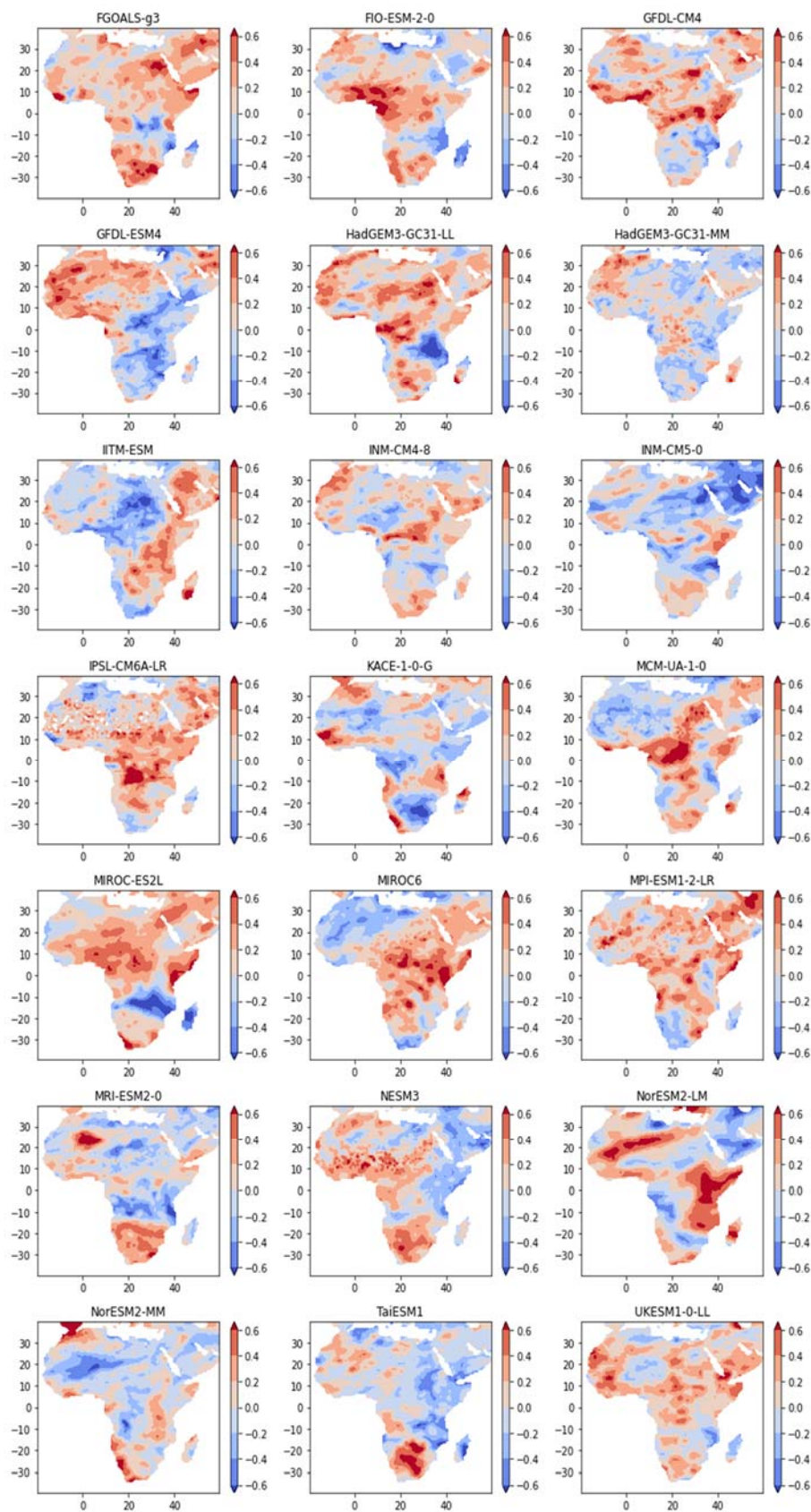


Figure 18: Same as Figure 17, but for a different set of models.

5 Characterizing the nature of crop growing season rainfall extremes during anomalous years in seasonal forecasts

Seasonal forecasts of meteorological variables including indicators of rainfall extremes are attractive for a variety of applications in different economic and social sectors, including crop production and food security (Calì Quaglia et al. 2021). A reliable and timely indication of the seasonal outlook, particularly on events related to rainfall extremes, can be associated with a well-defined economic value if delivered a few months ahead (Bruno Soares et al. 2018).

Year-to-year variability of the growing season climate determines crop productivity, particularly in the southern Africa region where rainfed smallholder farming systems dominate crop production (ADB, 2019). The highly variable nature of the climate in the region poses many challenges for farmers and crop production communities. Under such conditions, farmers, agricultural experts, and policy makers often lack the information on the likelihood of achieving optimal crop production levels, and are forced to make decisions based on limited data about how the growing season is evolving (WMO-No. 134, 2010). In these circumstances, reliable and timely issued seasonal forecast of rainfall derived products can play a vital role for pre-season and in-season strategic planning of crop production (Troccoli, et al. 2008; WMO, 2003).

The crop production season (October to April) in the southern Africa region has a significant inter-annual variability. Among the important mechanisms that control this variability are the El Niño-Southern Oscillation (ENSO) and the Indian Ocean Dipole (IOD). ENSO and IOD are now understood to be among the dominant modes of variability dictating the seasonal rainfall anomaly in southern Africa region (Sun et al., 2017; Nicholas Klingaman and Will Keat, 2018). Accordingly, one can expect a strong relationship of these climate modes not only with seasonal rainfall amount, but also with rainfall extremes.

Given the strong existing teleconnections between large scale climate features and the variability of the southern Africa region rainfall (Andrew Hoell & Linyin Cheng 2018; Glantz and Ramirez, 2020), this already characterized signal could be extended to rainfall extremes and to support the possibility of seasonal prediction of rainfall extremes. In this study, we assess observed teleconnections between climate modes (ENSO and IOD) and different indices for rainfall extremes. With this, we aim to characterize the nature of spatiotemporal variability of crop growing season rainfall extremes in Copernicus Climate Change Service (C3S) seasonal forecast model hindcasts during ENSO and IOD episodes. This is a brief assessment of the seasonal forecast models, as the correct representation of subgrid-scale features such as extreme rainfall events in anomalous seasons have a great value on the quality of the seasonal forecast products which may support decision makers in relation to crop production and food security.

5.1 Data and Methods

5.1.1 Hindcast data

This study considers seasonal forecast systems (Table 4) available in the Climate Data Store (CDS) of the Copernicus Climate Change Service (C3S) archive which provide near-surface precipitation data at daily temporal resolution. For all forecast systems, we consider all available hindcasts (1993 to 2016) initialized on September 1st and issued for the 6 months ahead, since we are targeting a crop production season for southern Africa region which generally covers from October to April. When dealing with seasonal anomalies, they are calculated considering the monthly values from the forecasts initialized in 1st of September. We analyse the longest available period, 24 years from 1994 to 2017, that is common to all systems and target season. We consider all available ensemble members over the hindcast period and utilize the ensemble mean for each seasonal forecast system.

Table 4: Description of the Copernicus Climate Change Service (C3S) Seasonal Forecast Models.

Seasonal Forecast Model	Prediction system	Time Range	Hindcast condition initial	Hindcast Ensemble Size	Reference
UKMO	GloSea5 GC2	215 days	1st, 9th, 17th, 25th of month	7 members/ start time	Maclachlan et al. (2015)
Météo-France	System 8	215 days	last and penultimate Thursday of previous month 1st of month	12 members each 1 member	Lauriane Batté and Michel Déqué (2017)

5.1.2 Rainfall extremes

The daily rainfall time series from AgERA5 (AgERA5, 2021) can be used to identify and examine seasonal October-March Southern Africa region rainfall extremes, and how ENSO and IOD phases condition those extremes. Even though, the rainy season for southern Africa region in general covers from October to April, we use the period from October to March since the lead-time of the hindcasts used in this study for 1st of September initialization (215 days) extends up to end of March. The World Meteorological Organization (WMO) Expert Team on Climate Change Detection and Indices (ETCCDI) recommended a total of 27 core indices with primary focuses to be derived from daily data. This study selected four precipitation-based indices (Table 5) to investigate extreme climate conditions over southern Africa region. These indices can provide relevant information on the amount and distribution of rainfall events to guide and monitor crop production activities. They are calculated over the course of the crop growing period which can indicate the drought intensity and frequency, moisture availability and provide information on excess rainfall events that can potentially cause flood phenomena.

Table 5: Description of precipitation-based indices used in the study.

Short Name	Long Name	Definition	Unit
<i>LDS</i>	Longest dry spell	Maximum number of consecutive dry days (when PR < 2.0 mm)	days
<i>NRD</i>	Number of rainy days	Number of days when PR ≥ 2.0 mm	days
<i>R10mm</i>	Number of heavy rain days	Number of days when PR ≥ 10 mm	days
<i>WDII</i>	Wet-day intensity index	Monthly total PR divided by the number of wet days in the month (when total PR ≥ 2.0 mm)	mm/day

5.2 Characterizing modulation by ENSO and IOD events

The ENSO phases are categorized using the Oceanic Niño Index (ONI) data (Glantz and Ramirez, 2020), a 3-month running mean of ERSST.v5 SST anomalies in the Niño 3.4 region (5°N-5°S, 120°-170°W). The Indian Ocean Dipole (IOD) is an anomalous state of the ocean-atmosphere system which is an irregular oscillation of sea surface temperatures between western and eastern Indian ocean (Saji et al., 1999). To examine the spatial distribution of crop growing season rainfall extreme anomalies during IOD and ENSO episodes (Figure 19), positive and negative cases are identified, as documented in Table 6 and the average value in those anomalous years is computed.

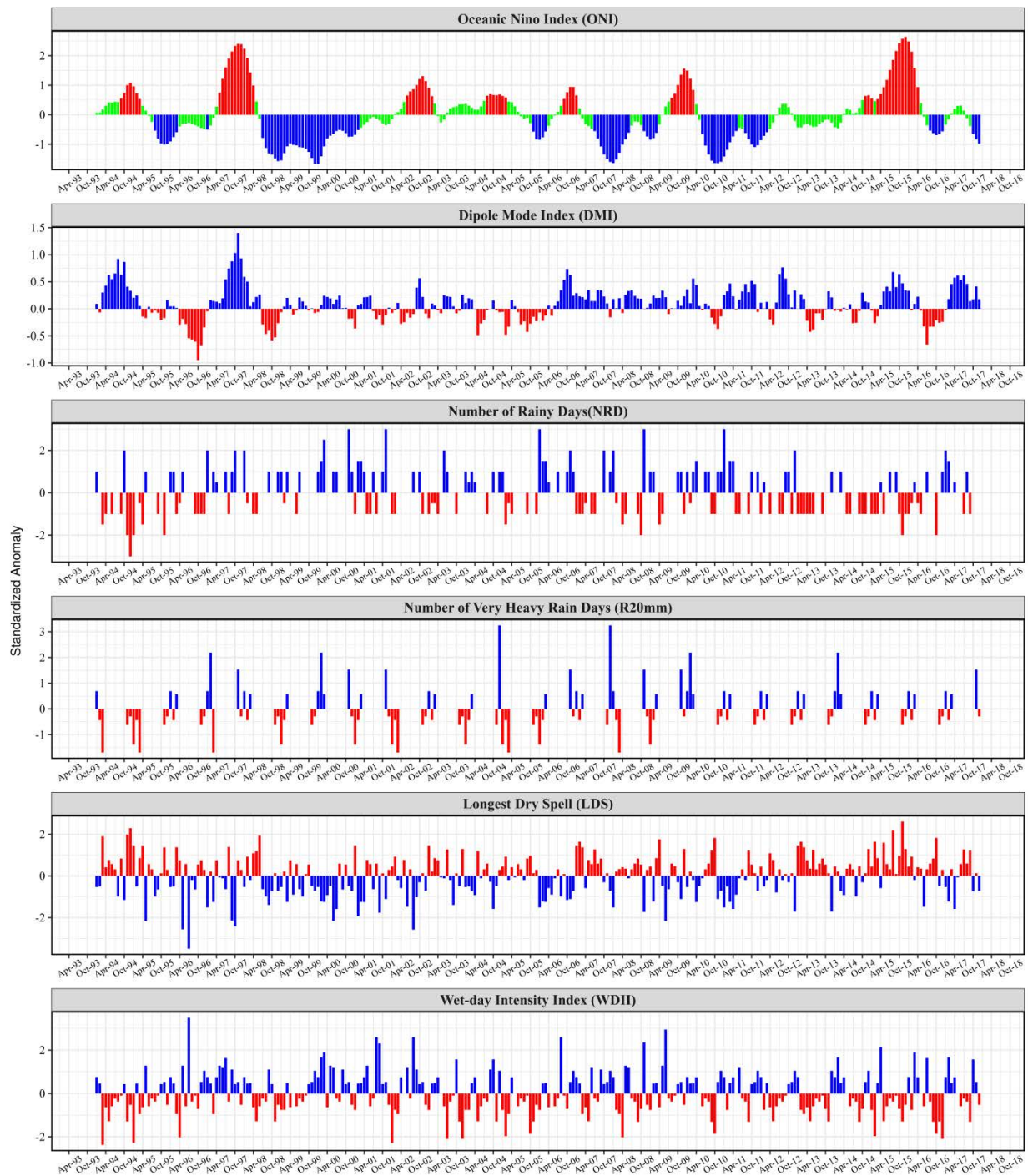


Figure 19: Monthly standardized anomaly showing positive and negative phases

It is important to note that differences in the Southern Africa region rainfall extremes response can be connected to the Pacific Ocean due to different ENSO phase (Ratnam et al. 2014; Hoell et al. 2015) and to the Indian Ocean due to different IOD phase (Reason, 2001). Since the SST anomalies characteristic of both ENSO and IOD rely on atmosphere-ocean coupling in their life-cycles, there is a question as to whether SST anomalies over the Pacific associated with ENSO may in turn force an atmospheric teleconnection that at least partially drives SST anomalies that define the IOD. Current evidence suggests that ENSO is not linearly related with Indian Ocean SSTs that define the IOD (Wang 2010), though at this time it cannot be ruled out that some nonlinear relationships may exist (Andrew Hoell & Linyin Cheng 2018).

Table 6: October - March 1993-2017 ENSO and IOD occurrences.

	El Niño	La Niña	Positive IOD	Negative IOD
<i>Season</i>	1994/95 1997/98 2009/10 2015/16	1995/96 1998/99 1999/00 2007/08 2010/11 2011/12	1994/95 1997/98 2006/07 2009/10 2012/23	2004/05 2005/06

The response of seasonal anomalies of rainfall extremes during ENSO and IOD episodes was investigated. A composite analysis of anomalies of seasonal rainfall extremes comparing the difference between the average of years with positive and negative ENSO and IOD episodes was carried out. Composite analysis is a sampling technique based on the conditional frequency of a given event (e.g. extreme rainfall anomaly) that will occur if it is certain that another event has taken place or will take place (e.g. ENSO and IOD). Thus, the composite analysis will provide information on the anomaly of the rainfall extremes being in the above-average or below-average category based on the state of ENSO and IOD episodes. Compositing by phase provides a better understanding on the spatial variability of the interannual modulation of rainfall extremes by ENSO and IOD episodes. Composites of conditions observed during ENSO and IOD events may provide useful estimates of what to expect.

The nature and linkage of the anomaly pattern and the strength of the linear relationship in observed and seasonal forecast models of seasonal rainfall extremes (i.e. during the crop growing period) with ENSO and IOD indices was investigated using correlation analyses. The correlation analysis was carried out with pre-season ENSO and IOD states (July to September (JAS), August to October (ASO) and September to November (SON)). This helped us to investigate the evolution of the linkage in pre-season months. In addition, this method specifically interrogates links between the indices of the phenomena (anomalies of seasonal rainfall extremes) at the timescale on which they are predicted (pre-season state of ENSO and IOD episodes).

5.3 Results and Discussion

5.3.1 Spatial distribution of rainfall extremes

Rainfall characteristics are a key metric in seasonal forecasts intended for crop production decision support. Indeed, the same amount of rainfall with different frequency and intensity could lead to different surface runoff, evaporation, and soil moisture condition. In seasonal forecast models, it may be possible to tune parameters to improve forecasting of rainfall amounts. Despite that, and unless the rainfall amounts are attributed with the correct combination of frequency and intensity, it is not certain that the tuned forecasts may result in improved information to support crop production practice (Trenberth et al. 2003).

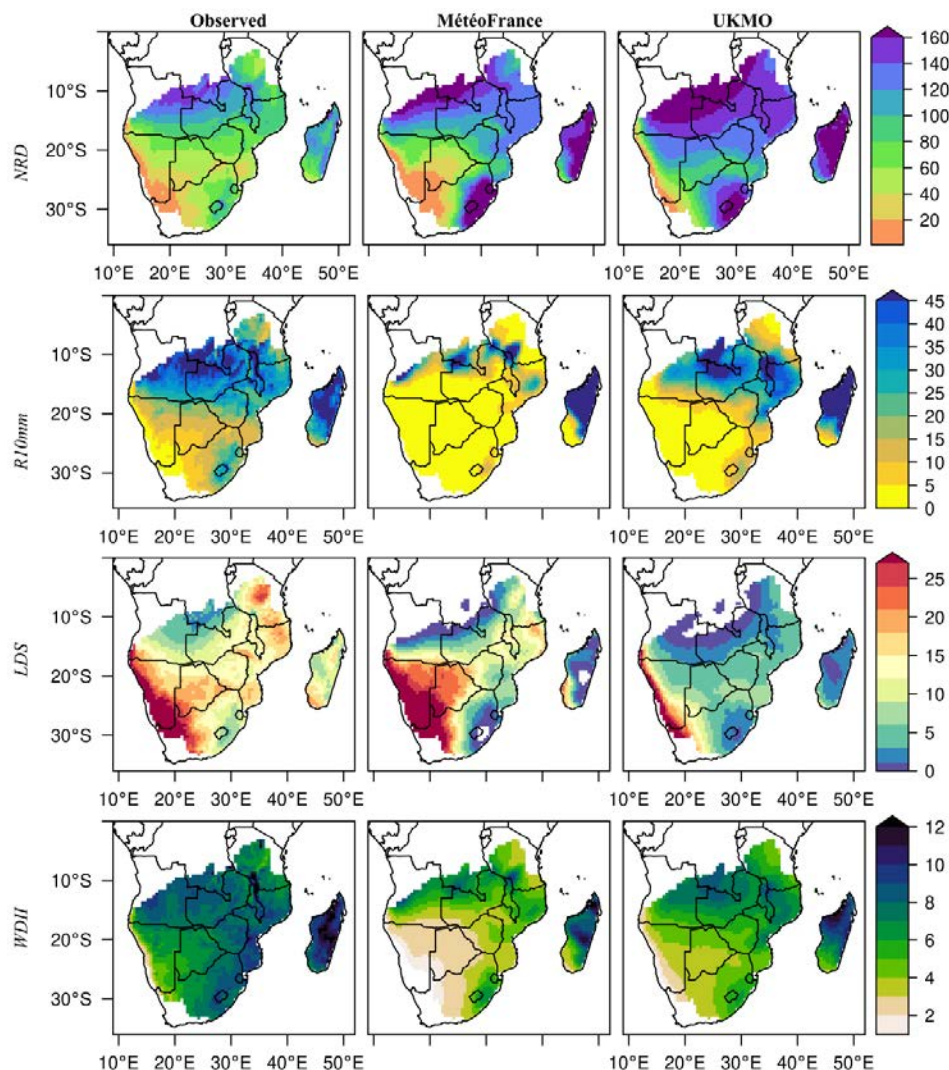


Figure 20: Seasonal summary of precipitation-based indices; the values are averaged over the hindcast period (1994 to 2017).

The spatial distribution of growing season rainfall extremes averaged over the hindcast period (1994 - 2017) was evaluated in southern Africa (Figure 20). The spatial gradient of observed rainfall extremes was represented by the seasonal forecast models. Yet, the seasonal forecasts failed to capture the total number of heavy rain days (R10mm) over the October to March period. The number of rainy days contributing to the seasonal rainfall is a simple index that captures the combined effects of rainfall frequency and intensity on the water supply (Kevin E. Trenberth and Yongxin Zhang, 2018).

Enhanced number of rainy days (NRD) was presented by the seasonal forecasts. This could be attributed to poorly resolved localized mesoscale response to the synoptic forcing by the seasonal forecast models (Salathé et al., 2008; Prein et al. 2020).

In the region of study, the occurrence of dry spells longer than 10 days is often observed during November to February. This is a time of the year where most cereal crops in the region undergo flowering and grain filling processes, the most critical stages in crop growth and development. The seasonal forecasts underestimate this LDS over the eastern half of the region. Particularly, lower magnitude of LDS was presented by the seasonal forecast from UKMO. The wet-day intensity index (WDII) is underestimated by the models over the southwestern arid and semi-arid dry lands, the area covering southern Angola, Namibia, Botswana, parts of Zimbabwe, Southern Mozambique and western half of south Africa. The underestimation was higher by the seasonal forecast from Météo France than UKMO. This underestimation might suggest the difficulty of the models in capturing the intensity of rainfall events over dry areas.

5.3.2 Historical composites

This section examines the spatial distribution of growing season anomalies of rainfall extremes during ENSO and IOD episodes (Figures 21-24). A consistent signal of the rainfall extremes during ENSO and IOD episodes was somehow shown by the observed and the seasonal forecast data. Above average NRD and R10mm over the northern part and below average in southern parts were observed during El Niño and positive IOD episodes and vice-versa. A resembling spatial pattern was produced by the seasonal forecasts, but above average NRD and R10mm were produced by the UKMO model over northern Namibia which contradicts the observed below average pattern. The observed above average NRD and R10mm during negative IOD episodes over parts of southern Africa was missed by the seasonal forecast from Météo France. In addition, the occurrence of heavy rainfall events over southwestern part of the region is missed by the seasonal forecast from Météo France. This poor performance of the seasonal forecast in representing R10mm agrees with the findings of Pepler et al. (2015), King et al. (2020) and Gebrechprkos et al, (2022), which highlight the struggle of seasonal forecast models in predicting heavy precipitation events

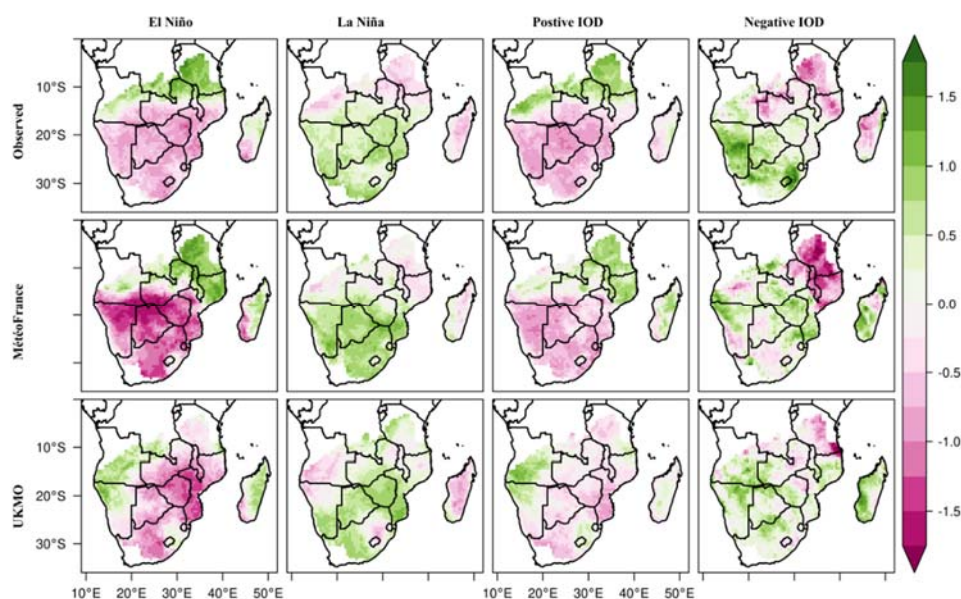


Figure 21: Spatial distribution of growing season Number of rainy days (NRD) anomaly during ENSO and IOD episodes.

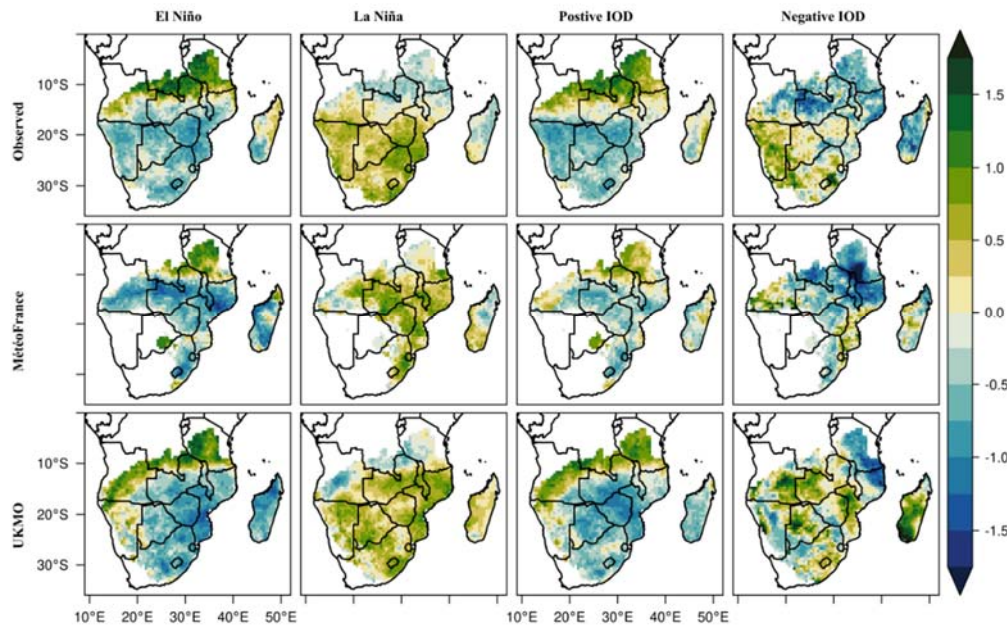


Figure 22: Spatial distribution of growing season Number of heavy rainy days (R10mm) anomaly during ENSO and IOD episodes.

During El Niño and positive IOD events above average LDS was observed in southern parts indicating the occurrence of longer dry spells during these episodes. Consequently, below average LDS was presented by the seasonal forecast from UKMO over western dry lands of Namibia during El Niño and positive IOD episodes which contradicts the observed above average LDS. Mixed signal of LDS across the region was shown by the observation and the seasonal forecasts during La Niña and negative IOD episodes.

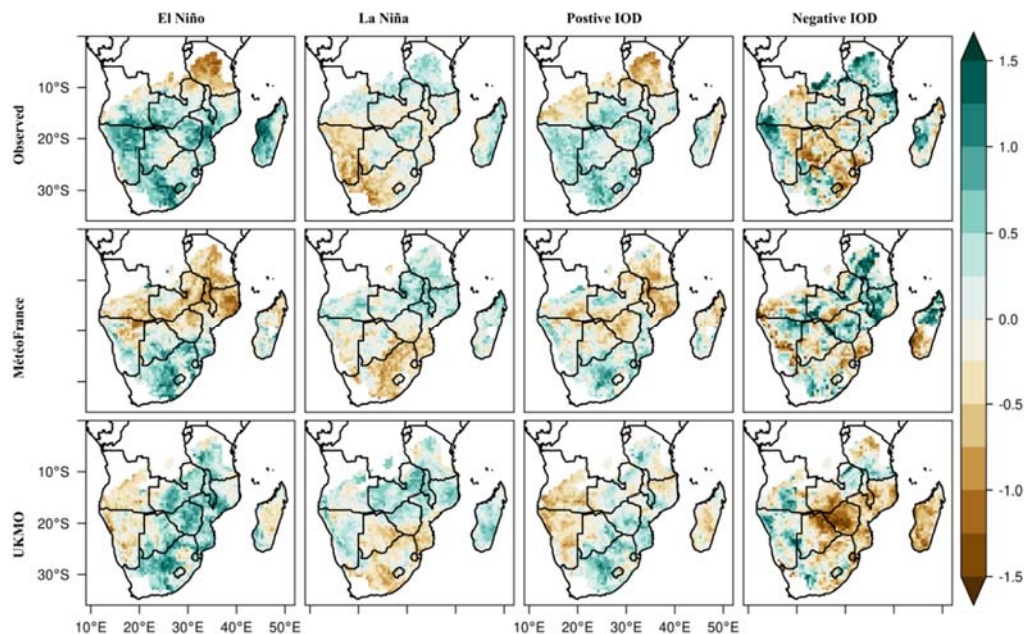


Figure 23: Spatial distribution of growing season Longest Dry Spell (LDS) anomaly during ENSO and IOD episodes

Similar to NRD and R10mm, above average WDII was observed over the northern parts and below average WDII over southern parts during El Niño and positive IOD episodes. A consistent above average WDII during La Niña episode was shown by the observed data and well captured by the seasonal forecasts. This suggests enhanced wet-day intensity was experienced across the region during La Niña episodes. The observed below average WDII over southern parts during El Niño episode was overestimated by the seasonal forecasts.

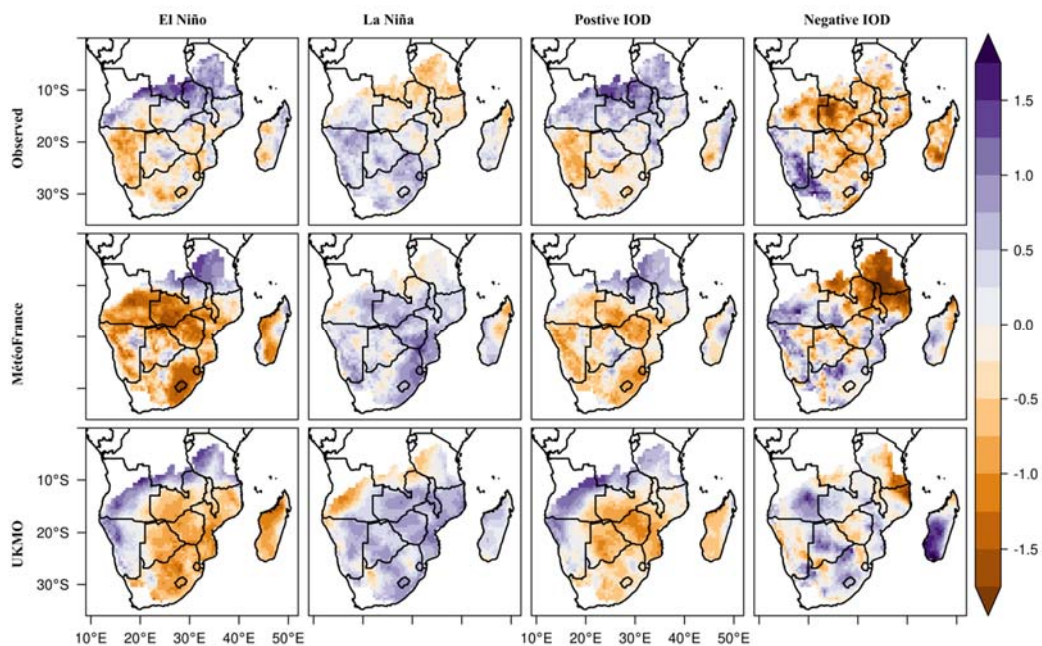


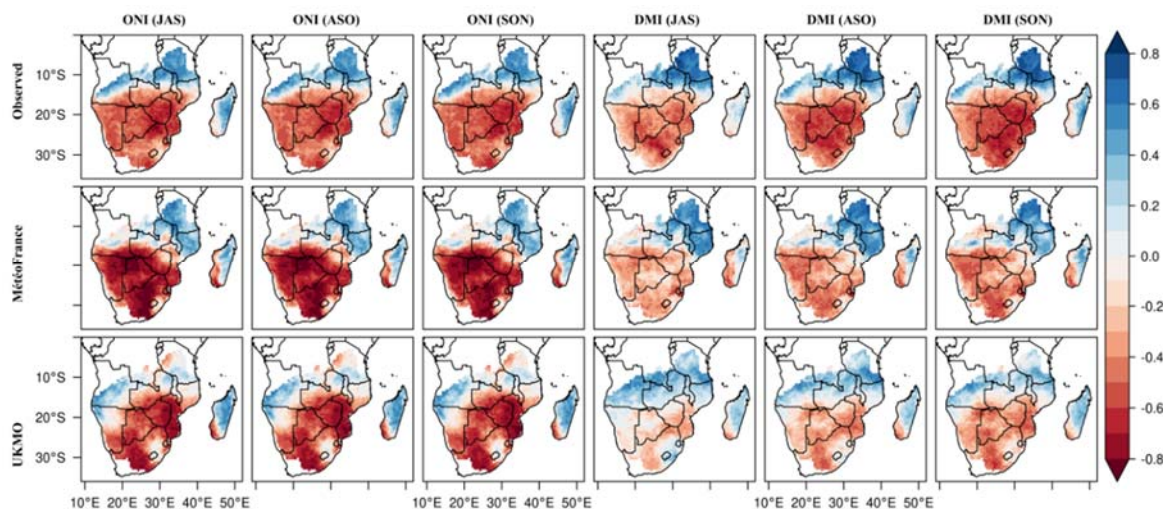
Figure 24: Spatial distribution of growing season Wet-day Intensity Index (WDII) anomaly during ENSO and IOD episodes.

5.3.3 Relationship and linkage between rainfall extremes with ENSO and IOD

Inter-annual anomalies of seasonal rainfall extremes are often linked to variations in systems that control the regional climate with quasi-periodic fluctuations, such as ENSO and IOD. The correlation between seasonal anomalies of rainfall extremes and preceding month ENSO and IOD episodes (in JAS, ASO, OND) is presented in Figure 25 and Figure 26. The data from observations and seasonal forecasts show a consistent positive correlation for all preceding months of ENSO and IOD episodes in the northern parts and negative correlations in southern parts of the region for NRD, R10mm and WDII. Whereas LDS show a reverse signal, negative correlations in northern parts and positive correlations in southern parts of the region in both observations and seasonal forecasts. The seasonal

forecast from Météo France produced week correlation for R10mm, as the model failed to capture the occurrence of heavy rain days over southwestern parts.

A) Number of Rain Days (NRD)



B) Number of Heavy Rain Days (R10mm)

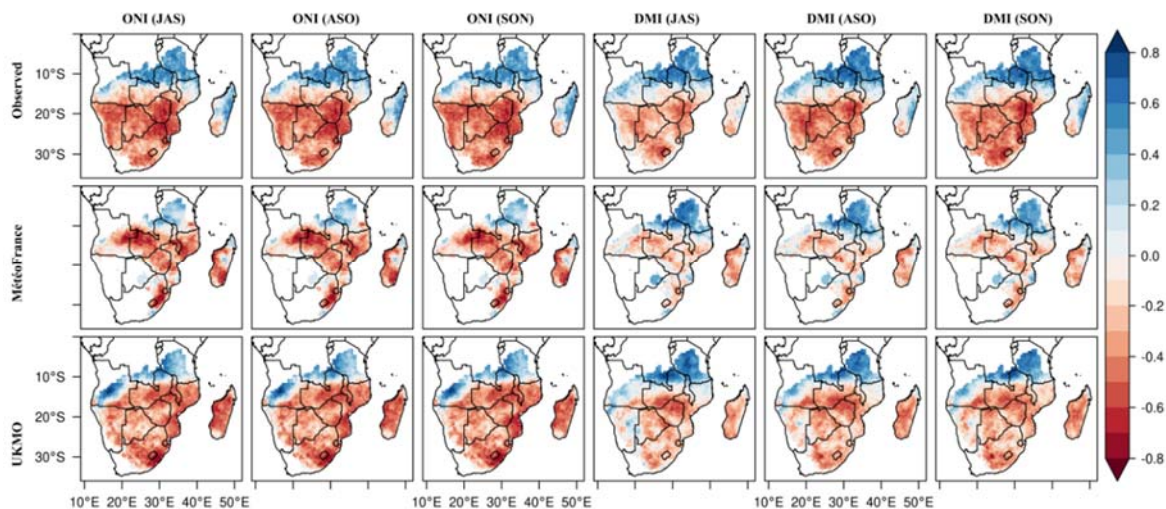


Figure 25: Correlation of preceding months ENSO and IOD episodes and rainfall extremes; A) Number of rain days and B) Number of heavy rain days.

The existence of this ENSO and IOD signals in the seasonal anomalies of rainfall extremes could have a potential to drive the inter-annual variations. Recent studies also suggest strong potentials for predicting seasonal anomalies of rainfall extremes using the pre-season and in-season ENSO and IOD state (Andrew Hoell & Linyin Cheng 2018).

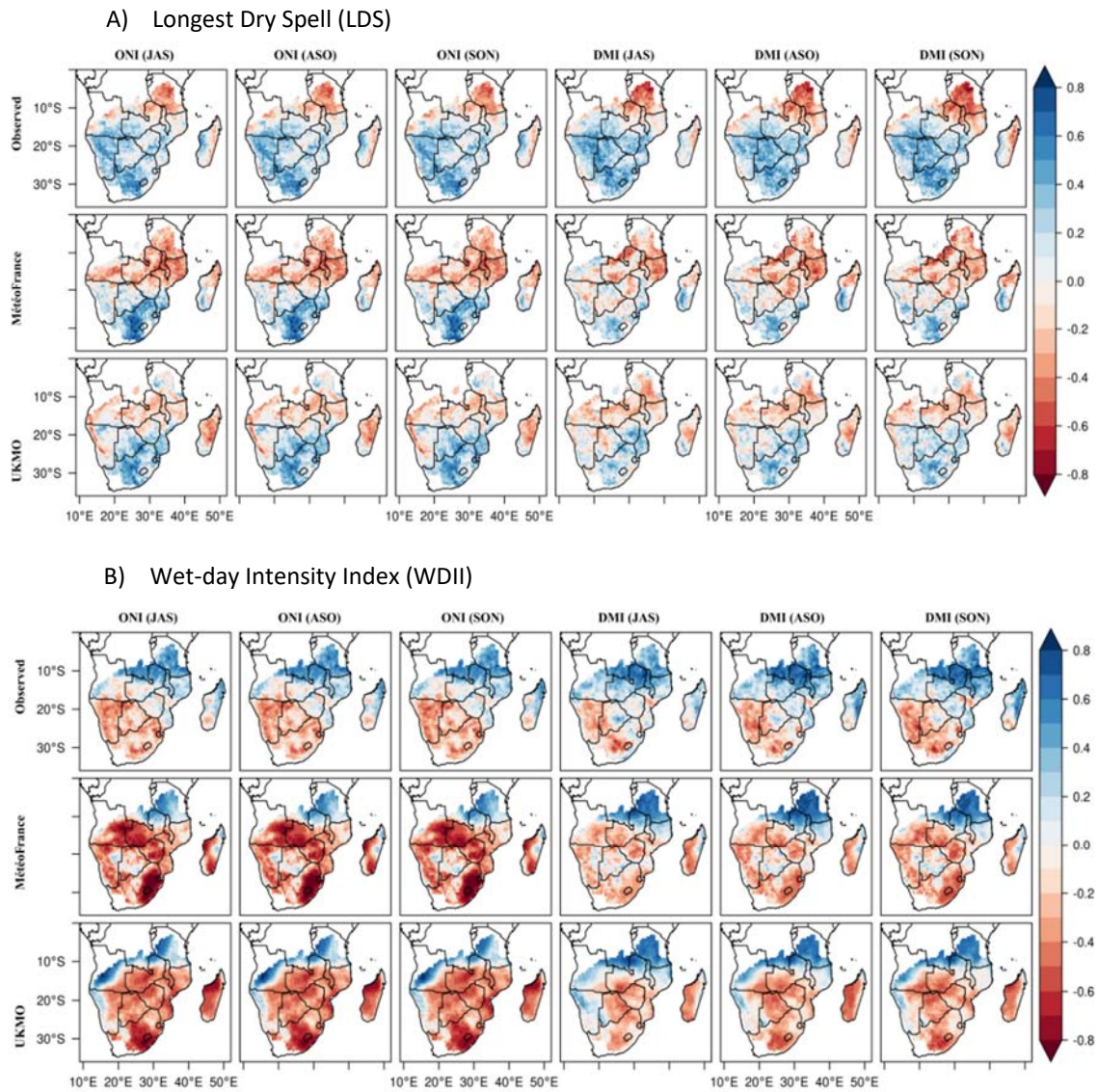


Figure 26: Correlation of preceding months ENSO and IOD episodes and rainfall extremes;A) Longest dry spell and B) Wet-day intensity index.

5.4 Remarks

Over the years, rainfall extremes during October to March over the southern Africa region trigger loss of crop production and provoke lasting detrimental effects on ecosystems (Masih et al, 2014). Extreme dry conditions during 2015-2016 (one of the most pronounced El Niño events) resulted in crop failures, food shortages and economic crises (Kolusu et al., 2019; Liu and Zhou, 2021). As archived in the OFDA/CRED International Disaster Database (<https://www.emdat.be/>), in 2008, La Niña related extreme wet conditions resulted in flooding and crop destruction. Considering the effects of dry and wet extremes on crop production, we sought to better understand the mechanisms by which these extremes are behaving to the region and how the region's two main climate drivers, ENSO and IOD, modify the spatial pattern and occurrence of these extremes in observed and seasonal forecasts.

The daily rainfall from the seasonal forecast models revealed many interesting features, including the light rainfall days that dominate the seasonal rainfall and the roles of the number of rainy days, heavy rain days, the longest dry spells and the intensity of daily rainfall during the crop growing period. The seasonal forecast models examined here reproduce enhanced number of rainy days, poorly simulate the number of heavy rain days, and underestimate the intensity of daily rainfall over dry and semi-arid lands. On the other hand, the forecasts more or less capture the observed response of anomalies of seasonal extremes during ENSO and IOD episodes.

The models' performance in daily rainfall frequency and intensity found here are consistent with previous studies emphasizing that dynamical climate models generally tend to rain too frequently at reduced intensity (Dai and Trenberth 2003). These biases can affect soil moisture estimates, surface runoff and evaporation as well as surface latent and sensible heat fluxes in the seasonal forecast models (Sun et al., 2005). For instance, Trenberth et al. (2003) discussed that light to moderate rainfall allows more time for water to enter into the ground, thus benefiting crops and enhance subsequent surface evaporation but may result in little surface runoff. However, heavy and intense rainfall can produce high runoff or even flash floods but may leave subsurface soils dry. The role of these discrepancies for simulating daily rainfall characteristics and extremes in seasonal forecasts is an important aspect of future research if seasonal forecasts are intended to benefit crop production process.

The ENSO and IOD show a consistent signal in modulating year-to-year fluctuation of the seasonal anomalies of rainfall extremes. These results are consistent to what has been previously identified in the literature (Williams and Hanan, 2011; Sazib et al. 2020; Ficchi et al. 2021). Knowledge of the state of ENSO has long been used to predict the deviations of the seasonal rainfall over southern Africa region since Nicholson and Entekhabi (1986) first identified the relationship between ENSO and Southern Africa region climate. The observed relationship between ENSO and IOD phases and seasonal anomalies of rainfall extremes, which is fairly reproduced by the seasonal forecast models during anomalous years can open the door to employ hybrid dynamical-statistical methods (Irene Cionni et al. 2022).

The dynamical seasonal forecast models have increased ability to forecast the state of sea surface temperature anomaly to produce seasonal forecasts. These forecast models, however, are not yet perfect in predicting the spatial distributions of occurrence of rainfall extremes across landscapes with different ecosystems. Studies such as this provide valuable contexts on the ongoing research progress on improving the ability of predicting the rainfall extremes at seasonal time scale. Empowering forecasters with information on how ENSO and IOD condition the probability of extreme rainfall occurrences allows them to provide relevant information on floods and droughts to mitigate the loss of crop production.

6 Rainfall extremes in Lake Malawi region

6.1 Objectives

This report falls within the broader aim of understanding extreme atmospheric hazards or high-impact weather events in southern Africa, typically generating substantial losses and damages and caused by processes in the Earth's atmosphere.

Amongst several directions of research and analysis intended to contribute to this broader objective, this section of the report contributes to two of these, addressing specifically extreme rainfall over the Lake Malawi basin, the region which is a subject of two of the Focus Africa case studies. These objectives are:

- characterising extreme events in terms of both frequency and magnitude in the context of their seasonality and predictability at seasonal time scale, and
- investigating future distribution and magnitude of extremes, relevant to all sectors and case studies, in the high-resolution climate projections.

6.2 Analytical framework

The overall framework of analysis targeting the first objective stems from results reported in Deliverable 3.2, where rainfall over Lake Malawi basin was analysed as a function of the source of the air mass and moisture transport by a low-level jet during rainfall events, revealed in earlier research (e.g. Barimalala et al., 2021 and Munday et al., 2021). In that deliverable, we have shown that the two main classes of synoptic systems bringing rainfall to Lake Malawi basin, differing in the dominant sources of moisture, i.e. the easterly flow mostly from tropical Indian Ocean, and westerly flow from interior of the continent originating from tropical Atlantic, firstly, result in different levels of area average rainfall over the basin, and secondly, have distinct seasonal pattern and varying relationships with regional rainfall. Here, we extend these analyses to specifically target extreme rainfall - both in terms of locally occurring (grid-point) extremes, and in area-total (basin-average rainfall) extremes at daily time scale. The choice of these targets is motivated by their impact on performance of agriculture, hydrology/water resources, infrastructure and potential for rainfall-induced losses and damages.

The overall framework of analysis targeting the second objective links to the work carried out in Work Package 4 under deliverable 4.2 that considers process-based evaluation of climate models/projections, with one of the techniques deployed describing circulation dynamics (frequency of synoptic states identified by self-organising maps (SOM) classifier) observed in reanalysis simulations and in climate change model simulations. Here, we extend those analyses to evaluate the relationship between circulation states and rainfall extremes. This provides an avenue to evaluate projections of future rainfall extremes in a downscaling-like manner, based on dynamical considerations rather than just through interpretation of the direct rainfall output of the climate models. While the latter avenue is not in fact pursued in this report, we do provide an illustration of future rainfall extremes over the Lake Malawi basin as projected by the moderate-resolution CORDEX models. In order to ascertain the level of uncertainty of these projections, we use so-called plume plots that enable the visualisation of multi-model, multi-generation ensemble projections.

6.3 Methods

We schematize the Lake Malawi catchment as a “box” spanning 33E to 35.5E, and 14.50S to 9.25S (Figure 27). For the analyses of future rainfall extremes, we distinguish three regions spanning the

Shire River basin. The two northern regions are intended to capture the main regional differences in magnitude of mean and extreme rainfall over the Lake Malawi “box” - higher values are generally observed in the northern part of the basin, and are associated with mountainous regions there (Figure 27). The southern, lower Shire region is added so that the entire basin is covered. While indeed mean rainfall and rainfall extremes vary spatially at a much finer scale than the three adopted regions, the size of the regions is dictated by and commensurate with the size of grid cells (computational units) of the two analysed GCM ensembles (CMIP5 and CMP6) and with the generalised level of analyses conducted here.

6.3.1 Extreme rainfall and moisture flow regimes

We re-use the datasets used earlier, and described in detail in D3.2: ERA5 reanalysis rainfall and variables describing atmospheric circulation - specific humidity (q), zonal (u) and meridional (v) winds at pressure levels spanning surface to 700 mb between 1979-2021. The pressure level data are used to derive vertically integrated moisture transport, and to define two low level moisture flow regimes - westerly flow and easterly flow, and schematize them as occurring on days when the net zonal flow across the western boundary of the Malawi “box”, i.e. across the “window” spanning 14.50S to 9.25S along the 33E meridian (Figure 27) is westerly and easterly respectively.

We subsequently analyse area-average rainfall (average over the Lake Malawi “box”) and maximum grid point rainfall on days characterised by either of the regimes, for the entire year (i.e. annual maximum of area-average rainfall, and annual maximum of maximum grid point rainfall recorded within the Lake Malawi “box”), but also for separate seasons.

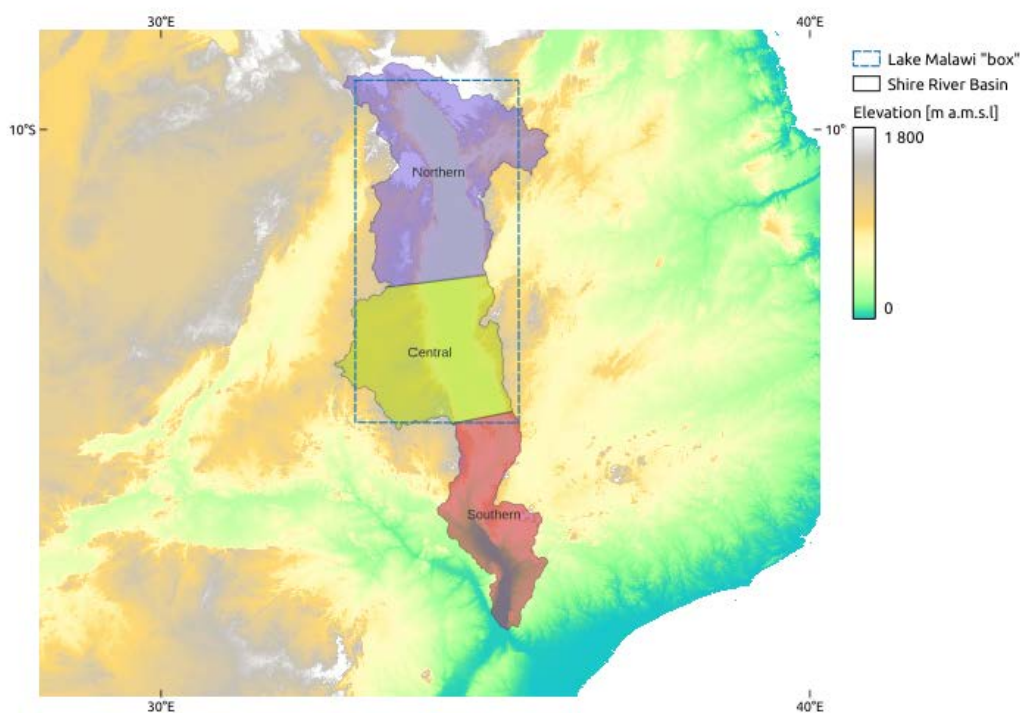


Figure 27: Location of Lake Malawi “box” and segmentation of the Shire River basin into three regions for analyses of projected rainfall extremes as described in D3.3.

6.3.2 Extreme rainfall and circulation states

Self-organising maps (SOMs) reduce high-dimensional multivariate atmospheric data to a specified number of generalised 2-dimensional circulation patterns (Hewitson and Crane, 2006). They do this

through a non-linear projection of the probability density function of the high-dimensional multivariate input data onto a two-dimensional array of nodes that span the full continuum of the data space. In doing this SOMs reduce the large multivariate dataset into a smaller set of data that still represent the original data and relate the large-scale atmospheric forcing to local scale responses. SOMs have been used to examine extremes (e.g. Lennard and Hegerl, 2015) and a more detailed description of the SOM methodology is available in the report of WP4, Task 4.2, Action 6, titled “A process-based assessment of global and regional projections”.

Here we use SOMs to classify daily circulation fields over the study region into 20 archetypal synoptic states. SOM classification is based on daily ERA5 reanalysis over 1981-2020 period, and the number of SOM nodes (20) is a subjective choice that allows to distinguish conditions that occur approximately 18 days a year ($365/20 \approx 18$). These represent archetypal “observed” states of the atmosphere during that period. We then quantify each synoptic state’s associations with mean and extreme ERA5-based rainfall through the lens of moisture transport into the Lake Malawi “box” described above. We analyse the seasonal distribution of each of the identified synoptic states, as well as area-average rainfall over the Lake Malawi “box”, and grid-point maximum rainfall, representing localised rainfall maxima, associated with each state.

6.3.3 Extreme rainfall projections

We use a particular form of time series graphs - the so-called plume plots (Figure 28), to evaluate change in extreme rainfall over the 3 regions of the Shire River basin. Plume plots visualise the evolution of the historical and future climate, with explicit presentation of uncertainty of projections across all three analysed ensembles, i.e. CORDEX, CMIP5 and CMIP6. These figures form the basis for evaluation of robustness of downscaled (CORDEX) projections against the GCM ensembles, as well as visualisation of the range of future climates as projected by the analysed ensembles.

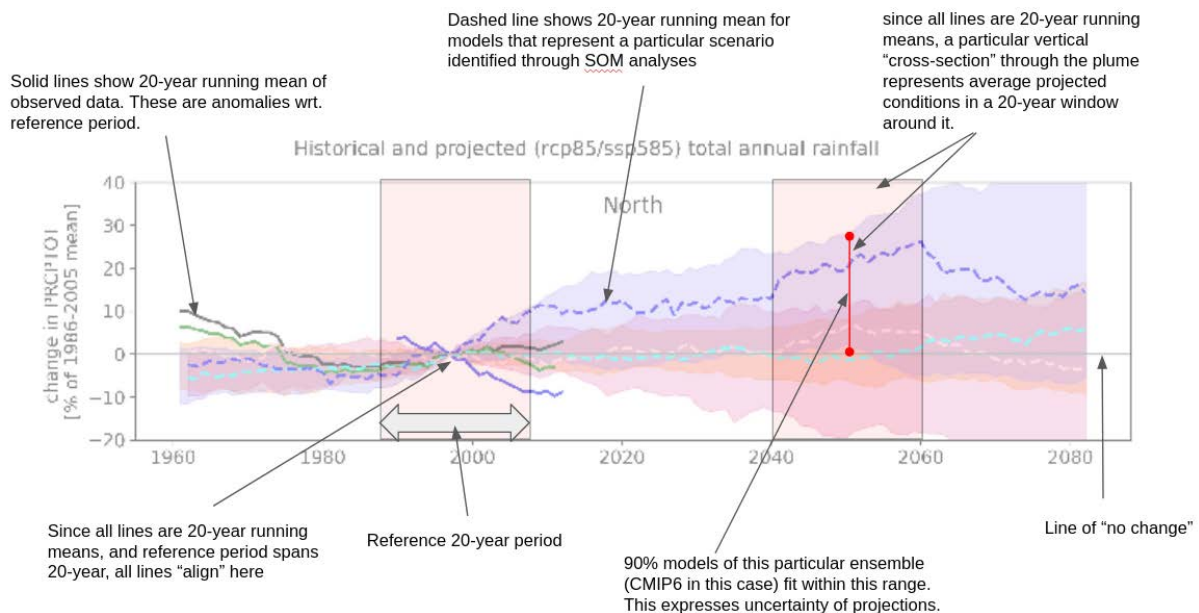


Figure 28: Components of plume plots. Each plume represents the spread of the central 90th percentile of a multi-model ensemble.

6.4 Results

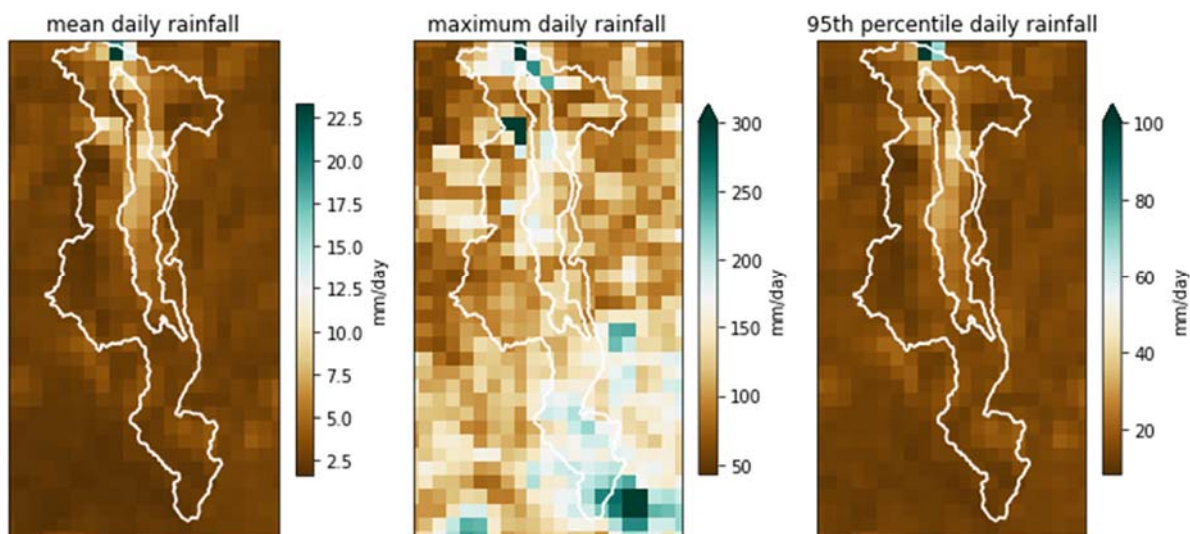


Figure 29: Spatial distribution of mean rainfall, maximum daily rainfall and 95th percentile daily rainfall in ERA5 data between 1979-2021. Superimposed are outlines of Shire River basin and Lake Malawi. Note the scales are not the same in order to better visualize the rainfall gradients.

Figure 29 illustrates spatial distribution of mean rainfall, maximum daily rainfall and 95th percentile daily rainfall in ERA5 data. Maximum daily rainfall, unsurprisingly, appears the most heterogeneous, with the highest values (in excess of 350mm/day) associated with mountainous regions in the north of the domain, with the extreme southern part of the Shire River basin. In addition, higher values are present in the northern half of Lake Malawi. The 95th percentile daily rainfall and mean daily rainfall appear to be less heterogeneous. Overall, these two variables show a similar spatial distribution to that of the maximum daily rainfall, with the exception of the southern tip of Shire River basin, where high maximum daily rainfall does not seem to be accompanied by noticeably higher mean and 95th percentile rainfall.

6.4.1 Extreme rainfall and moisture flow regimes

As mentioned in the introduction, the analyses carried out in Deliverable D3.2 suggested that different levels of area average rainfall over the basin are associated with the two main classes of synoptic systems bringing rainfall to Lake Malawi basin (the easterly moisture flow regime mostly from tropical Indian Ocean, and westerly moisture flow regime from interior of the continent originating from tropical Atlantic). This is illustrated in Fig. 3a of that Deliverable D3.2 which shows a considerably larger number of days with low area-average rainfall under the easterly regime, while also a large number of days with high area-average rainfall under the westerly regime. These differences can potentially be interpreted in terms of spatial heterogeneity of rainfall, with rainfall under the westerly regime being more uniformly distributed than that occurring during the easterly regime, with a consequence that the westerly regime results in more wide-spread rainfall, leading to area-average extremes over the region, while the local extremes are associated with the easterly regime. This is most likely the result of the nature of rainfall generating mechanisms - while rainfall associated with easterly air masses takes the form of typical convective storms, rainfall associated with the westerly air masses is stratiform in nature (DCCMS C.Vaya - pers. comm). A more detailed analysis confirms that assertion.

Firstly, of note is that as illustrated in Fig. 29 of D3.2, moisture influx from the west occurs almost exclusively during the DJFM period, and there are few westerly flow events in the remaining months of the year, while the easterly moisture flow dominates the months outside of the DJFM season. This is evident in Figure 30 below that presents a distribution of daily area-average rainfall under westerly and easterly regimes for all months (left-hand-side panel) and the core of the rainy season (right-hand-side panel). The differences between these regimes are clearly noticeable, with the distribution of area-average rainfall under the westerly regime shifted towards higher values compared to that under the easterly regime.

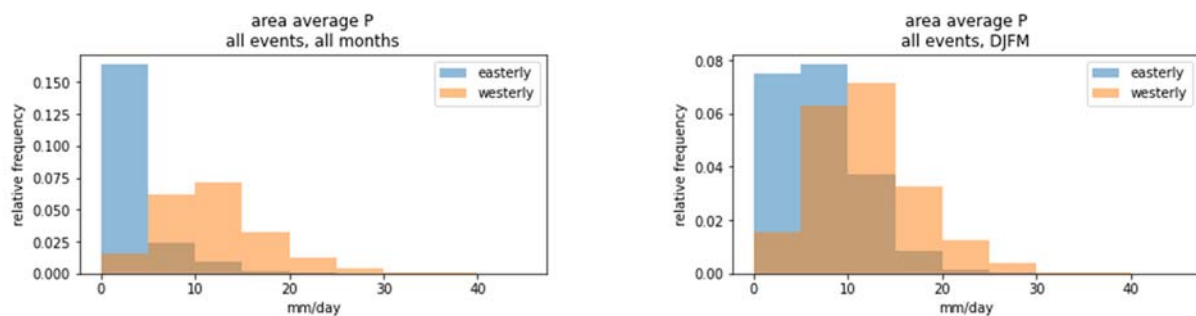


Figure 30: Distributions of rainfall associated with the easterly and westerly regime of moisture influx into the Lake Malawi basin.

Further, in order to ascertain the similarities and differences between local extreme rainfall under each of the two regimes, Figure 31 presents distributions of the highest annual area-average rainfall and the highest daily rainfall in each of the grid point over the full period within the Lake Malawi “box”. Differences in the former are well articulated, with the maximum value and the distribution for the area-average shifted towards higher values under westerly flow regimes (Figure 31a). Somewhat surprisingly, there is also a similar shift visible in the maximum daily grid point rainfall, with westerly regime conditions seemingly favouring overall higher grid point rainfall values (Figure 31b), although indeed the maximum value present during the easterly regime is higher than that for the westerly regime.

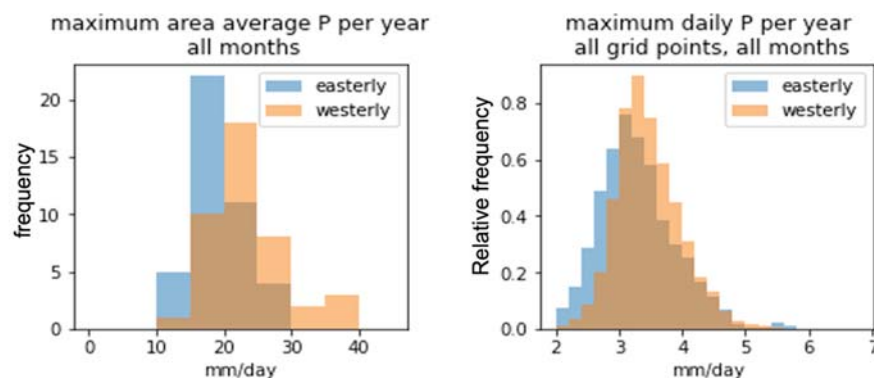


Figure 31: Distributions of maximum area-average rainfall per year and maximum grid point rainfall per year associated with the easterly and westerly regimes of moisture flow into the Lake Malawi basin.

6.4.2 Extreme rainfall and circulation states

Analyses described so far consider a relatively simple differentiation of synoptic or circulation conditions under which extreme rainfall forms based on a distinction of the direction of air masses flow and moisture transport across the axis of Lake Malawi “box”. Here, we consider a more

comprehensive differentiation of atmospheric circulation conditions - namely circulation classification based on SOMs. Results of classification of an extended rainy season (NDJFMA) hus , ua and va fields (specific humidity, zonal and meridional wind) at 700 mb are presented in Figure 32 in the form of circulation archetypes (typical circulation patterns associated with each class (or SOM node). Figure 33 presents the frequencies of each of the nodes in each of the months.

Nodes 5,10,15,20 (the last column of the SOM array) occur only in the core of the rainy season, i.e. DJFM, while nodes 1,6,11,16 (the first column of the SOM array) are characteristic of the shoulder (ND and MA) of the rainy season, with the remaining nodes spanning all months, with those in the second column occurring predominantly in the shoulder season, while those in columns 3 and 4 in the core rainy season.

Nodes in the 3rd, 4th and 5th column represent the Inter Tropical Convergence Zone (ITCZ) and Congo Air Basin (CAB) in the southerly position with moisture inflow from the equatorial region, and a combination of these conditions with various levels of the continental high pressure over southern Africa, and various levels of influx of moisture from tropical and southern Indian Ocean. Notably, node 5 is characterised by a combination of westerly moisture regime and a strong inflow of moisture from the southern Indian Ocean into the Lake Malawi region, while nodes 15 and 20 are still characterised by the westerly regime, but with much weaker contribution of moisture from the southern Indian Ocean.

Nodes in the 1st and 2nd columns represent the passage of the westerly wave in the mid-latitudes with the mid-latitude cyclones in their seasonally most northerly position, with the Lake Malawi region influenced by air masses from over the Indian Ocean north of Madagascar.

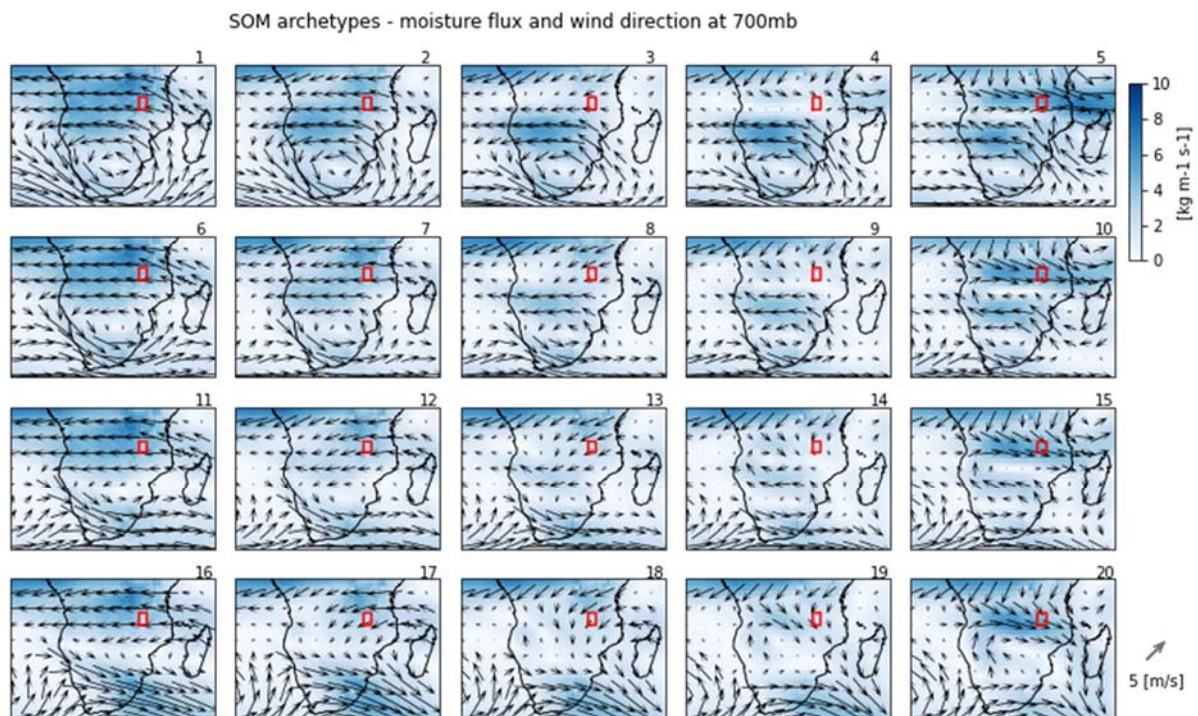


Figure 32: SOM node archetypes for hus , ua , va fields in the NDJFMA season. Illustrated are wind direction and magnitude (arrows) and associated moisture flux (shading). Lake Malawi “box” superimposed in red.

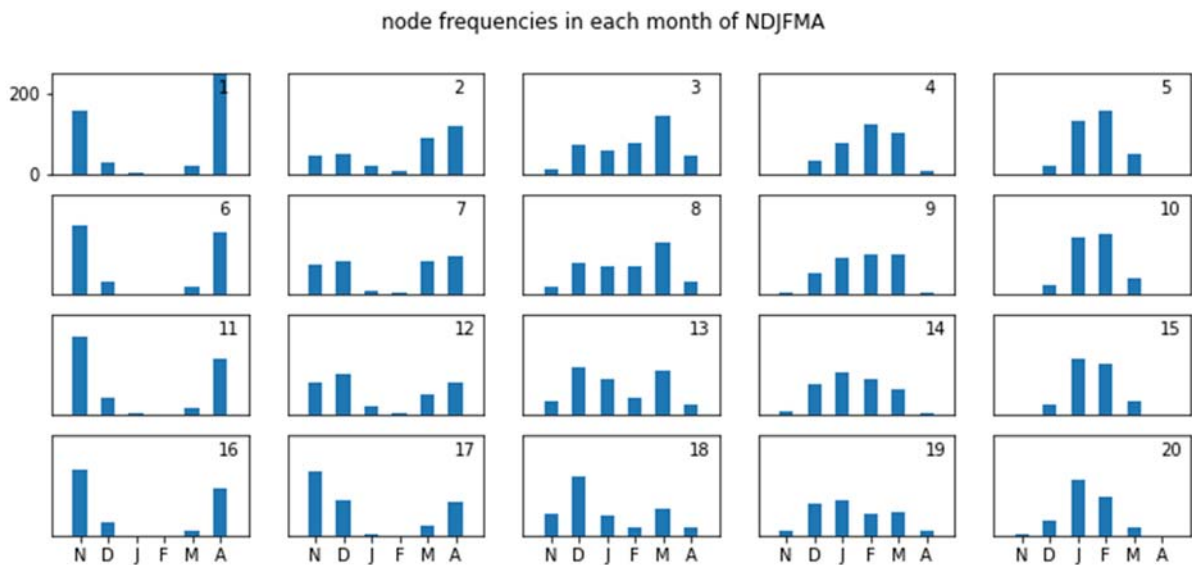


Figure 33: Monthly frequencies of SOM nodes illustrated in Figure 32

Figure 34 illustrates the relationship between SOM based classification of circulation and the westerly and easterly moisture flow regimes used in the previous section. The association between these two ways of characterising drivers of rainfall over Lake Malawi region is very clear - nodes in the last column of the SOM array represent exclusively the westerly regime, while the nodes in the 4th column represent a mixture of westerly and easterly regimes. That “mixing” is most likely a result of generalisation of SOM-based classification that takes into account circulation patterns over the entire region, while the “regime” approach considers only very local manifestation of that regional circulation.

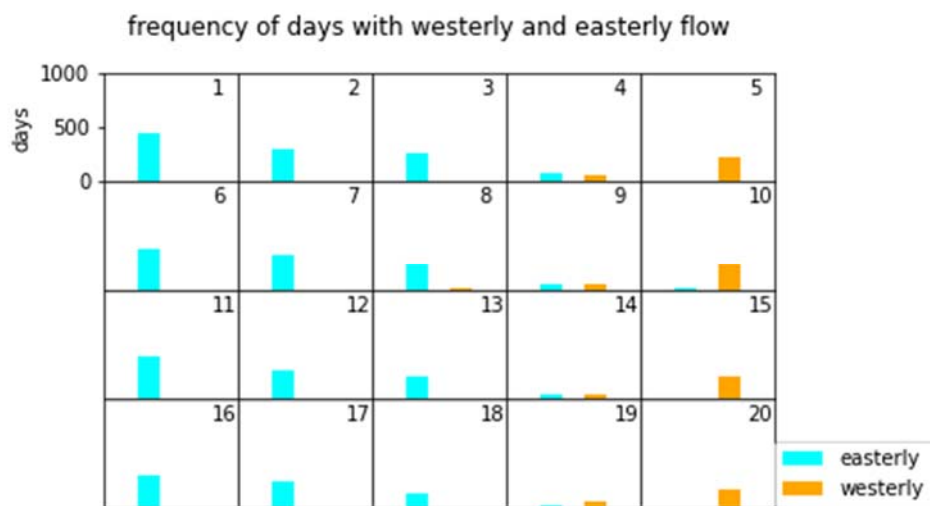


Figure 34: Frequency of days with easterly and westerly moisture flow regime for each SOM circulation category

Various characteristics of rainfall associated with each of the SOM nodes are illustrated in Figures 35 through 37.

Maximum area-averaged rainfall of the Lake Malawi “box” ranges between 19–38 mm per day across the SOM with higher values for nodes in the top-right corner of the SOM array (Figure 35), and that pattern is even stronger articulated for the mean and 95th percentile rainfall.

In terms of grid point rainfall, a proxy for localised rainfall, maximum values are associated with circulation represented by nodes in the 3rd and 4th column of the SOM array (Figure 36), with highest values of both maximum and 95th percentile in nodes 3,4 and 8,9. There is a notable difference in magnitude of local rainfall between nodes dominated by the westerly regime, i.e. those in the 5th column of the SOM array, and the other circulation conditions occurring in the core of the rainy season, i.e. those represented by nodes in the 3rd and 4th column of the SOM array.

Another way to evaluate the circulation-extreme rainfall relationship in a more robust way is to consider the numbers of very high rainfall events recorded under each circulation pattern. This is illustrated in Figure 37, which clearly shows that the high area-average rainfall events are associated with the two nodes representing the westerly regime best, i.e. 5 and 10, while the high grid point rainfall events are associated with nodes 3,4,8 and 9 that represent easterly regime with relatively strong continental high and CAB/ITCZ in the southerly position.

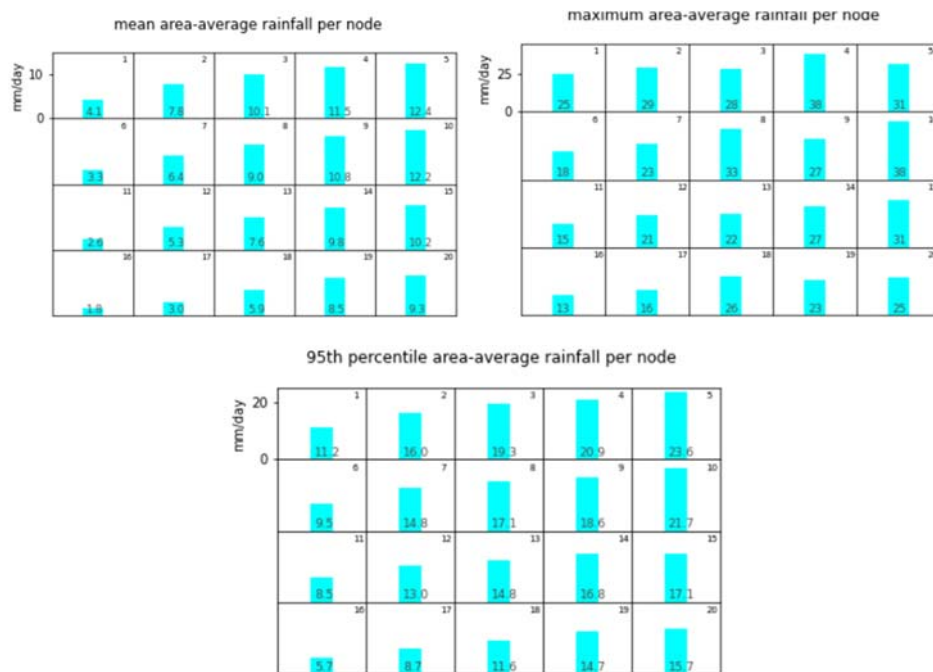


Figure 35: Mean, maximum and 95th percentile of area-average rainfall associated with each SOM circulation category.

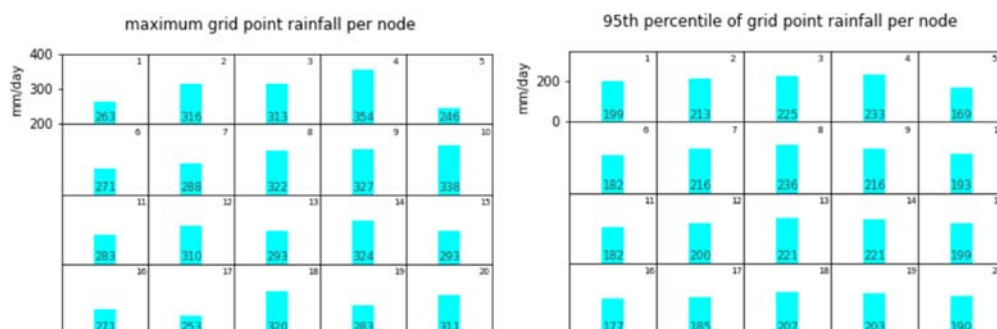


Figure 36: Maximum and 95th percentile grid point rainfall associated with each SOM circulation category.

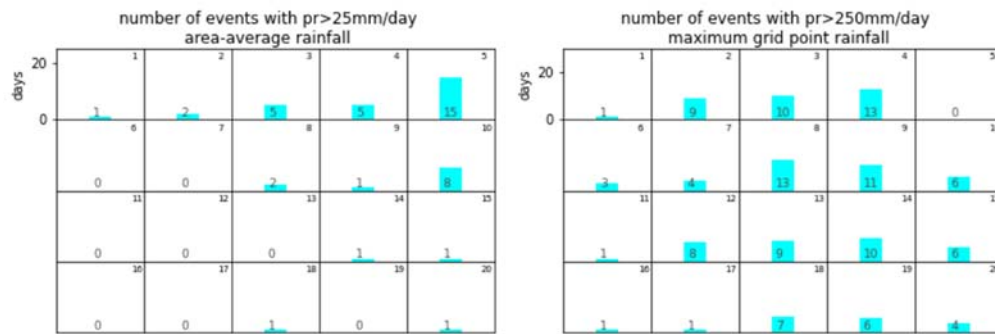


Figure 37: Frequency of high rainfall events associated with each SOM circulation category for area-average rainfall and local rainfall

In order to evaluate spatial heterogeneity of extreme rainfall under different synoptic forcing, we calculate the average quantile for all days on which each SOM circulation category occurs (Figure 38). To generate this figure, quantiles are calculated for each day for each grid point based on an empirical distribution describing the distribution of given grid point's daily rainfall over the 1979-2021 period. We use quantiles rather than actual rainfall values because of high differences between daily rainfall magnitudes in various parts of the domain, which mask any relationships between circulation and local rainfall anomalies. Using quantiles ensures that anomalies and extremes are depicted in terms of their relation to local average conditions rather than in terms of absolute magnitudes.

Figure 38 illustrates a relatively complex set of relationships between local extremes and synoptic circulation, manifested at regional and local spatial scales, and which can be summarised as follows:

- there is a relatively clear distinction between the northern (Lake Malawi and upstream) and southern (lower Shire basin) parts of the domain, with the north receiving extreme high rainfall under circulation conditions of nodes 4,5,9,10, and the south receiving high rainfall under circulation conditions of nodes 15,19 and 20.
- there are differences in the relationship between high rainfall and circulation manifesting at smaller spatial scales too. Notably, Lake Malawi itself, and in particular its northern half, shows different patterns to those characterizing the surrounding dryland regions. There also appear to be several small regions that behave differently than the surrounding, likely reflecting the influence of orography and land-water boundary on local convection – with the northwest shore of Lake Malawi showing particularly articulated differences.
- in the above, the northern half of Lake Malawi receives the highest rainfall under conditions described by nodes 2,3,7,8 while rainfall is subdued under circulation driving high rainfall in drylands, i.e. under nodes in columns 4 and 5 of the SOM node array. In turn, the north-western shore of the Lake receives high rainfall under circulation conditions described by nodes in column 5 of the SOM array, and in particular under conditions of nodes 5 and 10.

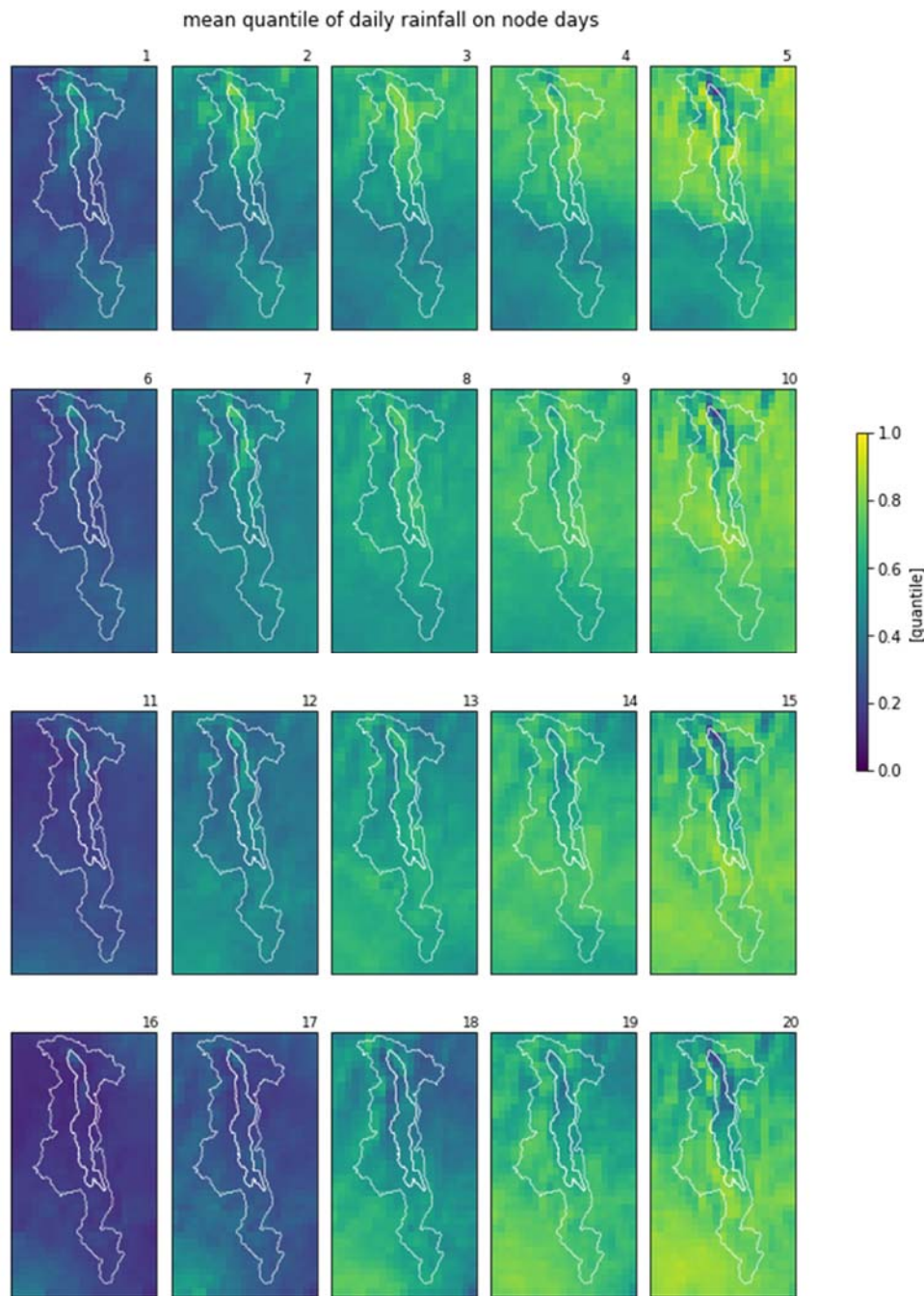


Figure 38: Maps showing average of quantile of daily rainfall on days on which a given circulation category occurs. Quantiles calculated on grid-point basis from empirical distribution describing daily rainfall (including no rainfall days) over the 1979-2021 period.

6.4.3 Extreme rainfall projections

We use plume plots described in Section 2.3 to evaluate historical and future changes in mean and extreme rainfall in the 3 regions of the Shire River Basin. Historical and projected changes in mean rainfall are presented in Figures 39 and 40 and in extreme rainfall Figures 41 through 44. There is a large uncertainty in projections of both mean and extreme rainfall for the Shire River basin, but the general patterns are as follows:

- There is a general reduction in mean annual rainfall projected for each of the analysed region both under rcp45/ssp245 and rcp85/ssp585 scenario, but ensemble median reduction is relatively small - in the order of 5% by 2070
- There is a general increase in extreme rainfall events projected for all three analysed regions. The increase is stronger under rcp85/ssp585 than under rcp45/ssp245 scenario, with ensemble median increases by 2070 in the order of 5% in the latter and 10% in the former, and essentially all members of all three analysed ensembles indicating higher intensities of 1-day and 5-day rainfall in 2070s than those observed in the reference period (1981-2010). Maximum projected values are in the order of 20% under rcp45/ssp245 and 30-35% under rcp85/ssp585 scenarios.
- There are minor differences between the three analysed regions, but they do not appear to be systematic
- Similarly, there are minor differences between the different generations of projections as represented by the three ensembles, but again, they do not appear to be systematic. In particular, there are no significant differences between the high-resolution downscaled projections with CORDEX ensemble and the two GCM ensembles (CMIP5 and CMIP6) although the uncertainty range (spread) of CORDEX ensemble is in general somewhat narrower than that of the GCMs. This might be a result of comparatively fewer models used in the CORDEX ensemble.
- Observations (represented here by ERA5 values) agree well with model simulations, both in terms of reduction in the mean rainfall and increases in the extreme rainfall. Observations of extreme rainfall show, however, somewhat stronger increases than those simulated by the models over the same time, particularly in the Central and Southern region (signified by the observed “trajectory” located at the “edge” of the plume in Figs. 41-44).

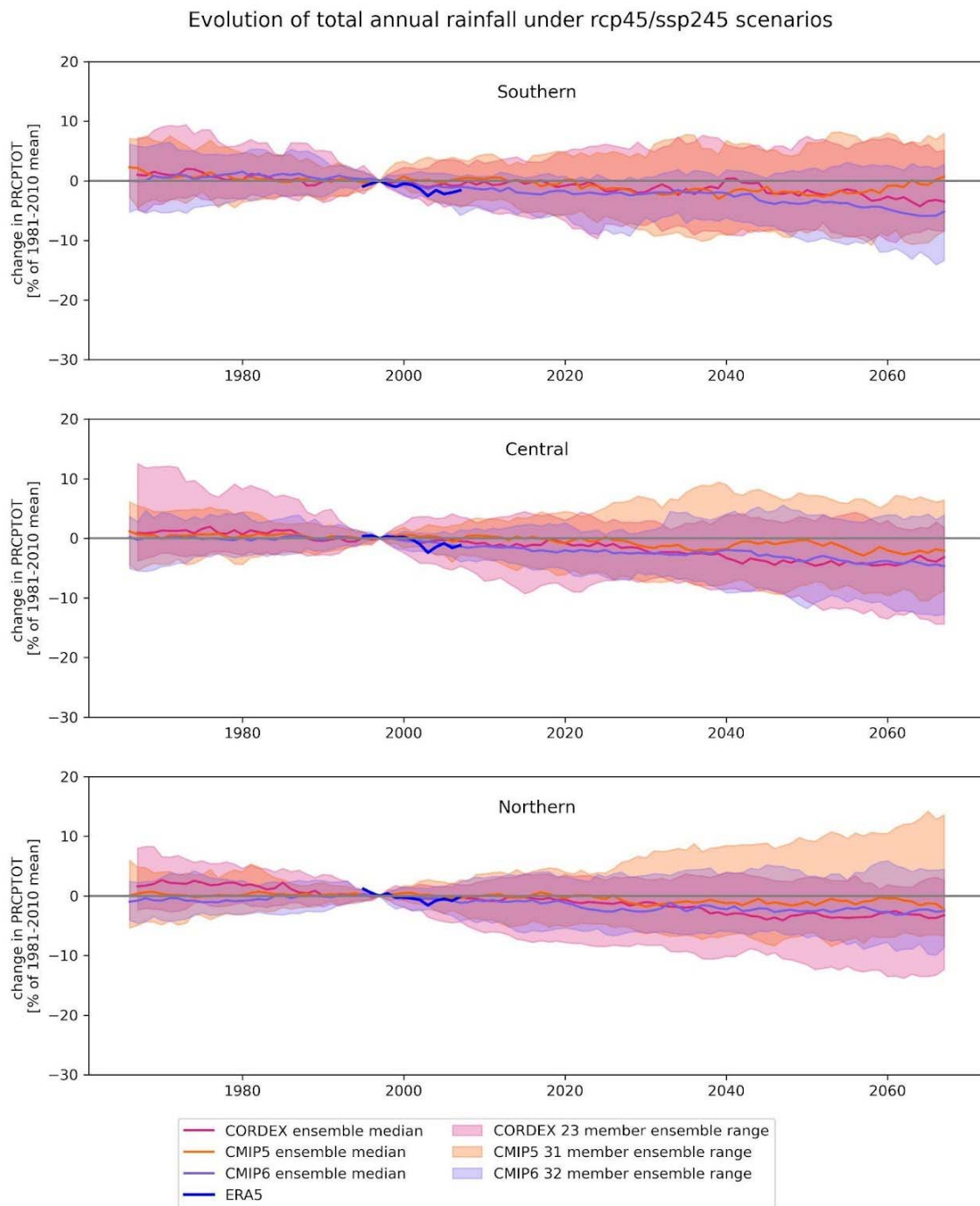


Figure 39: Plume plots illustrating ranges of total annual rainfall in historical simulations and climate projection under RCP45/SSP245.

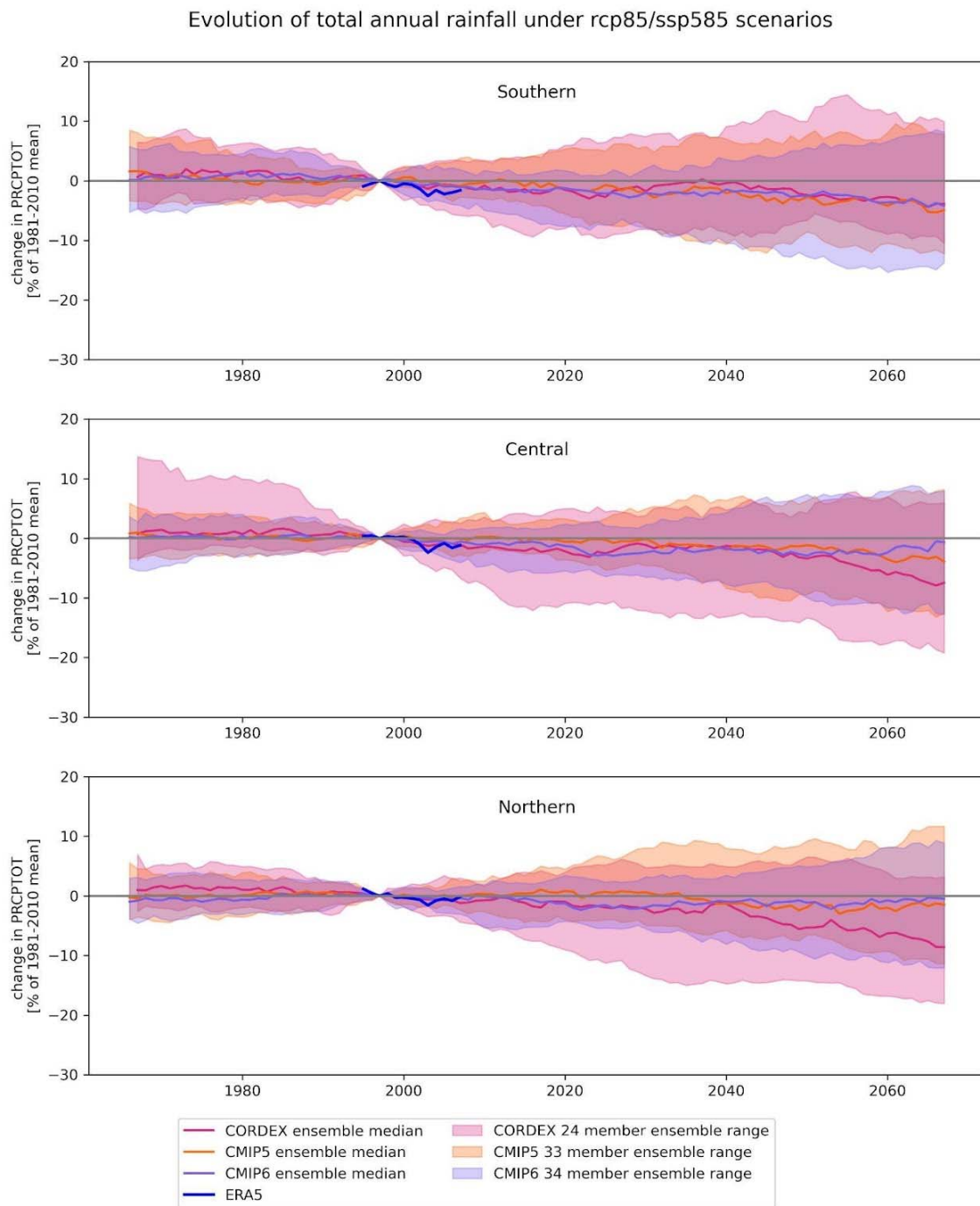


Figure 40: Plume plots illustrating ranges of total annual rainfall in historical simulations and climate projection under RCP85/SSP485.

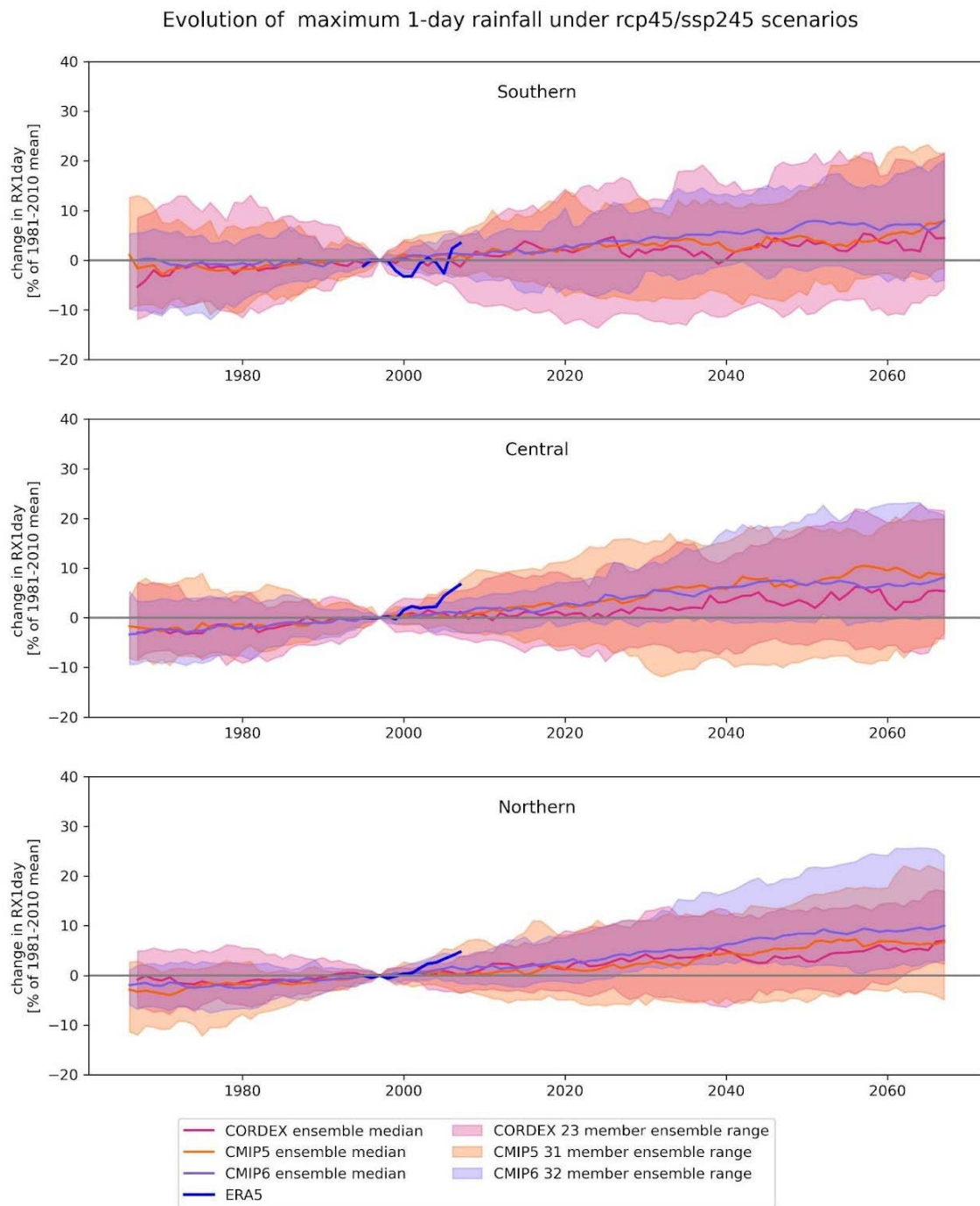


Figure 41: Plume plots illustrating ranges of 1-day annual maximum rainfall in historical simulations and climate projection under RCP45/SSP245.

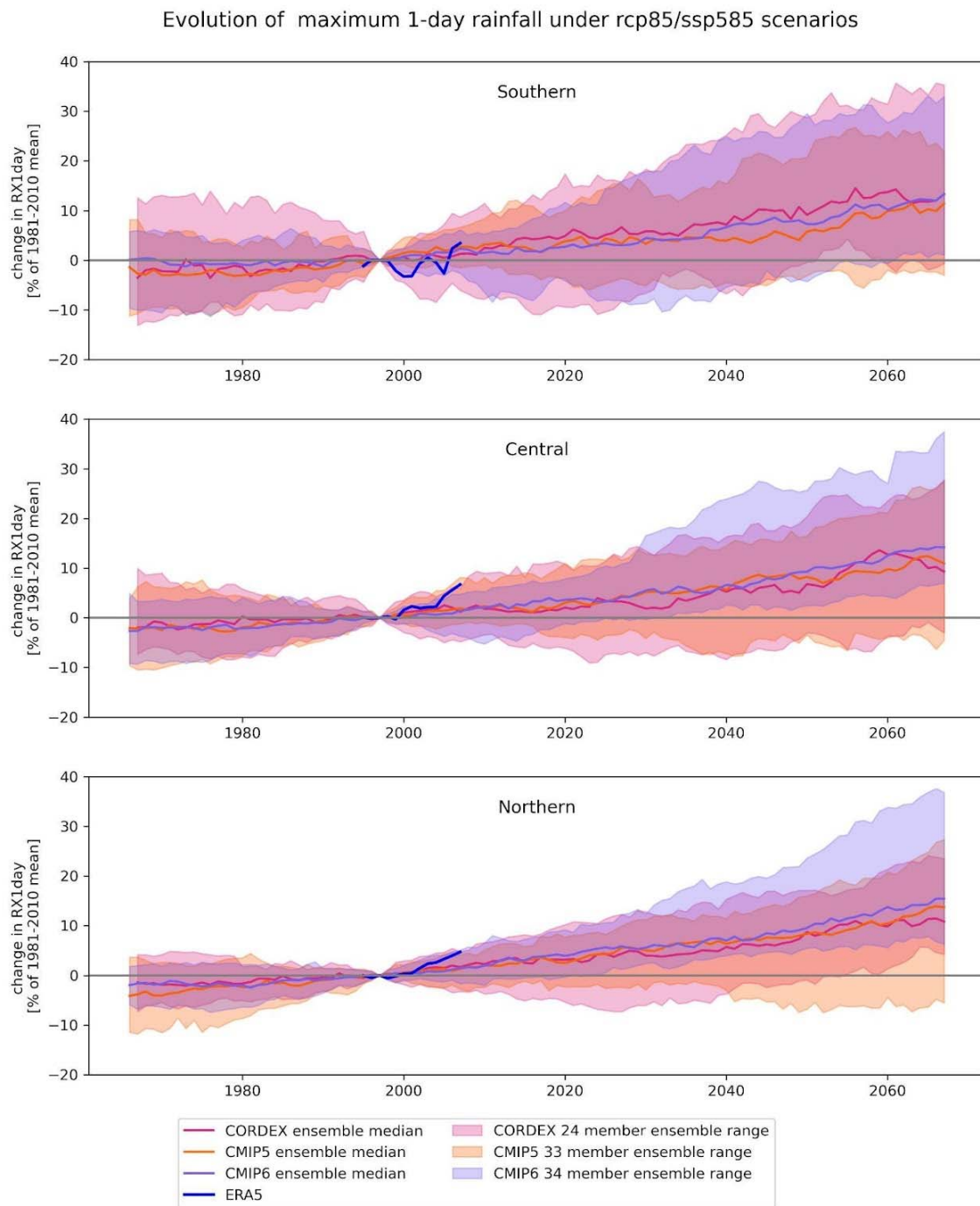


Figure 42: Plume plots illustrating ranges of 1-day annual maximum rainfall in historical simulations and climate projection under RCP85/SSP585.

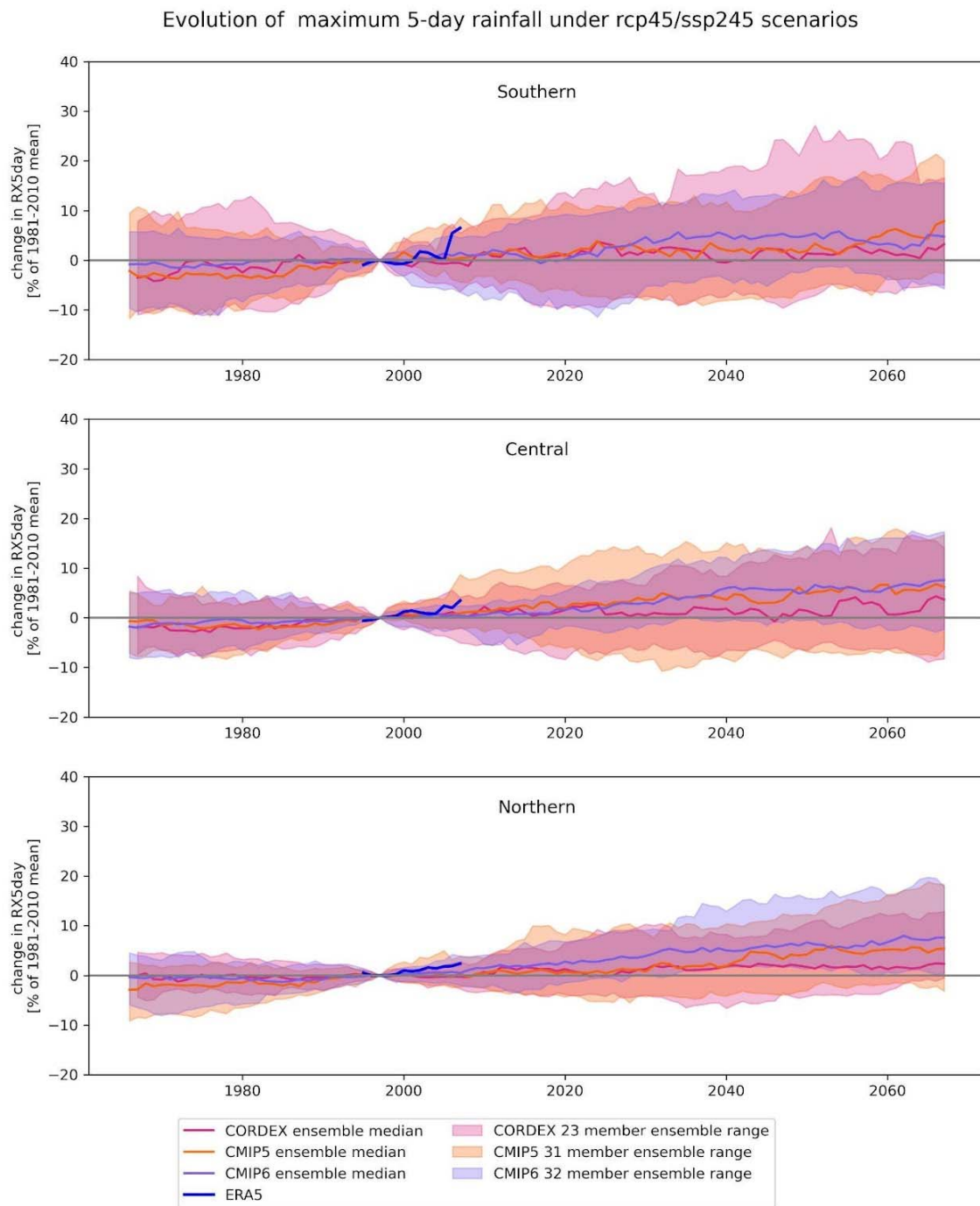


Figure 43: Plume plots illustrating ranges of 5-day annual maximum rainfall in historical simulations and climate projection under RCP45/SSP245.

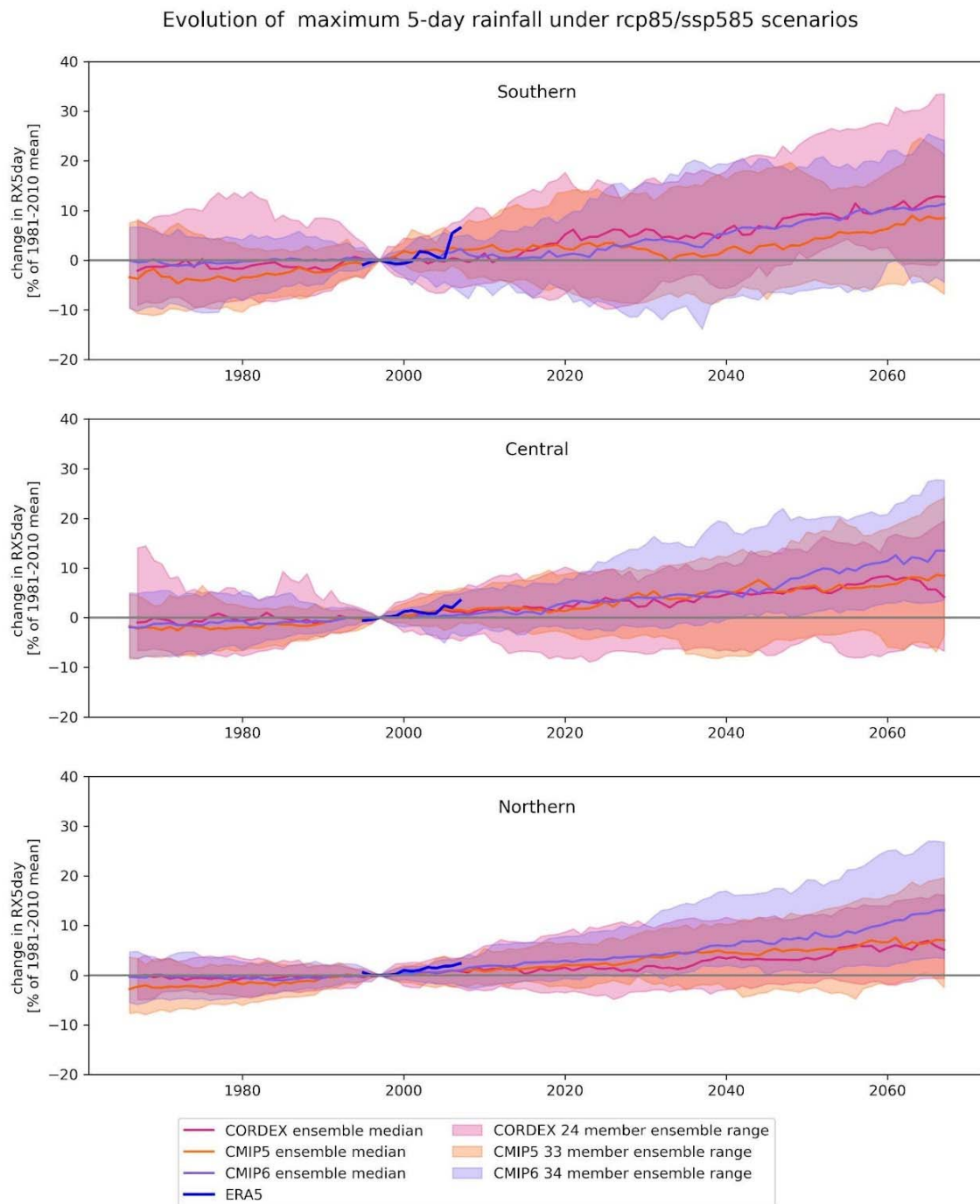


Figure 44: Plume plots illustrating ranges of 5-day annual maximum rainfall in historical simulations and climate projection under RCP85/SSP585.

6.5 Remarks

We distinguish two types of extremes - local extreme rainfall and region-average extreme rainfall, as these have different relevance to different sectors. Local rainfall extremes show substantial spatial heterogeneity that to a certain extent corresponds to that of mean annual rainfall, with the highest values in the mountainous regions in the north, and in the northern half of Lake Malawi.

We evaluate synoptic drivers of the two types of extreme events, with the outlook towards understanding the dynamical climate drivers of these events in order to evaluate their future projections.

The extreme area-average rainfall events occur during conditions of westerly moisture flow regime, as manifested by intensities and frequency of high intensity events. The extreme localized rainfall events are associated with a number of synoptic conditions and occur predominantly under easterly moisture flow regime and particularly under conditions when flow from tropical Indian Ocean is combined with flow from the subtropics.

While the above describes generalized regional patterns, our analyses reveal that the relationships between local rainfall extremes and circulation patterns are complex and intricate, with clear differences in synoptic drivers of rainfall extremes between the northern and the southern parts of the Shire River basin as well as differences between the lake surface itself and surrounding drylands with several locations, in particular north-west shores of Lake Malawi manifesting different relationships than those observed at the larger, regional scale.

In terms of projections of future rainfall over the Lake Malawi and Shire Basin, a reduction in mean annual rainfall projected for each of the analysed zones (Northern, Central and Southern), in the order of 5% by 2070. There is a relatively robust signal of increase in 1-day maximum and 5-day maximum rainfall into the future, with projections indicating values in the order of 0-20, 0-35% higher by 2070s than those historically recorded, depending on the GHG emission scenario. It has to be noted that these results consider only the rainfall output from GCMs used for climate projections, and do not explicitly evaluate whether these projections are consistent with the relationships between extreme rainfall and circulation dynamics described above. Deliverable 4.2 (Process based assessment of climate projections) analyses, however, evaluates how well different GCMs are able to simulate frequencies of the synoptic states considered here, building towards such an evaluation.

The analyses presented here provide a generalised understanding of the characteristics and synoptic drivers of the two considered extreme rainfall categories, but they carry an important caveat. These analyses do not address explicitly the role of tropical cyclones as causes of extreme rainfall. These will be explored in further deliverables of the project.

7 Defining multi-hazard indexes for combined extreme events in Africa

7.1 Background

Africa is widely recognized as the continent with the highest vulnerability to climate change and to climate extremes. Furthermore, the widespread poverty across SADC countries and their dependence on rainfed agriculture makes this area particularly vulnerable to climate-related disasters.

Climate change indeed presents a risk for the society and for several economic sectors, e.g., agriculture, water resources, infrastructures, food security, and health. Climate information, if opportunely incorporated into multidisciplinary development planning and projects, could enhance decision-making within the aforementioned sectors, by developing an integrated Climate Risk Management (CRM) approach.

Amigo designed a specific and flexible multi-hazard Extreme Climate Index (ECI) to describe the climate risk caused by extreme events. This index is built upon meteorological data, specified for climatic regions and designed to capture the severity and frequency of heat waves, droughts, floods, wind storms and other extreme weather events important to the SADC area, such as cyclones. In particular, ECI integrates a dedicated extreme wind component to address the occurrence of tropical cyclones and storms in the area.

7.2 The Extreme Climate Index (ECI)

ECI is aimed at shifting the focus from weather risk management to the broader scope of managing the risk associated with climate change. While weather risk management is related with the uncertain outcome of a specific activity when affected by the weather conditions on very limited time scales, and with the reaction to events of a specific physical type (e.g. droughts, floods, wind storms), the main purpose of ECI is instead to detect potential changes in the occurrence of extreme events, considering both their frequency and magnitude.

To so, a suitable ECI should:

- be multi-hazard, targeting the extreme events that are likely to have the gravest impact on Africa's vulnerable populations and on the economic growth potential;
- capture individual extreme events and be suitable for monitoring changes in both frequency and intensity of these extremes over an appropriate time frame;
- be standardized, so that it could be aggregated and compared across larger geographical regions;
- have a well-defined parametric probability distribution function, to allow for straightforward hypotheses testing and retrieving of other statistical diagnostics, such as the direct computation of return times;
- reflect the large-scale climate situation of a specific region;
- be constructed from data satisfying risk transfer criteria, that is data with a consistent, sufficiently-long, high-quality historical record that is also produced objectively and consistently in near-real time going forward.

The following sections will detail the design of our multi-hazard ECI, starting first from the identification of data matching our requirements, then the single hazard components are described, and finally a formal definition of ECI and of its statistical properties is provided.

7.2.1 Meteorological datasets

Building a multi-hazard ECI requires identifying and obtaining consistent data of critical meteorological variables to detail each climate hazard at a high spatio-temporal resolution. For this reason, ECI leverages the ECMWF Re-Analysis ERA5 to retrieve statistically-relevant time series to monitor climate extremes.

Data at a high spatio-temporal resolution is crucial for climate-risk monitoring at local scales: this characteristic is meant not only in terms of a sufficiently-long historical record, but also going forward, requiring data that is produced objectively and consistently in near-real time, a feature that is foundational to climate reanalyses such as ERA5.

ERA5 (McKee et al., 1993) is the fifth generation of global reanalysis by ECMWF, provided on a regular $0.25^\circ \times 0.25^\circ$ grid for a wide variety of meteo/climatological variables. ERA5 spans the period 1950-present with hourly temporal resolution; this aspect is of particular importance for calculating the single-hazard indicators defined below, as they need to rely on relatively long time series as baselines (at least 30 years).

In particular, our formulation of ECI for the SADC region relies on four variables from ERA5: precipitation, air temperature at 2 meters from ground level, and the zonal (u) and meridional (v) horizontal components of wind speed at 10 meters from ground level.

7.2.2 Hydrological component (SPI)

ECI relies on the Standardized Precipitation Index (SPI) developed by McKee et al. (1993)¹ to describe drought events and their time scale, probability and intensity in an intuitive and statistically sound manner.

The number of drought indices available in literature is huge (e.g. Zargar, Sadiq, Naser, & Khan, 2011). However, a drought index to be used in the definition of ECI must fulfill a few important properties: a) to require a minimum number of input variables so to be easily and sustainably computed over large areas; b) to have a consistent definition over different geographical areas, so that the critical threshold can be conveniently defined once all over the entire domain of interest.

Among the many existing drought indices, the Standardized Precipitation Index (SPI) meets the required properties. SPI has been developed with the specific objective of addressing the different practical issues that are important in the analysis of drought, namely their time scale, probability and intensity (Zargar et al., 2011). According to the definition by McKee et al. (1993), the standardized precipitation is simply the difference from the mean in precipitation for a specified time period divided by its standard deviation. However, the cumulated rainfall is not normally distributed when considering accumulation periods of less than one year. Typically, the cumulated rainfall has a skewed distribution with long tails of intense rainfall events. Such tails of the distribution become more populated when the accumulation period gets shorter. This reflects the fact that, for example, the relative fluctuations of rainfall over time scales of weeks is much larger than the variability over an entire season. Finally, in order to compute "standardized" deviations, the resulting probability corresponding to the value of the cumulated rainfall has to be transformed into its corresponding value of the normal distribution through the inverse normal distribution. This step allows SPI to have a normal distribution. It is good practice to account for the probability of zero rainfall before transforming the probabilities through the inverse transform distribution, i.e. $p_{new} = pze \cdot$

$[(1 - pze) * p_{old}]$, where p_{new} is the new probability to be transformed, p_{old} the one obtained through the rainfall distribution, and pze is the probability of zero rainfall at each location.

The computation of the SPI proceeds as follows.

1. Computing the moving accumulated rainfall, i.e. for each month the cumulated rainfall over the considered time scale, e.g. 3 months.
2. Fitting the moving accumulated rainfall on a specific month onto a suitable distribution to establish a relation between each value of accumulated rainfall and its probability.
3. Applying the inverse normal distribution technique on the values of probability associated to each value of the accumulated rainfall to compute the value of the index (SPI) which corresponds to the same probability.

This procedure produces, by construction, a set of values with mean $\mu = 0$, and standard deviation equal to $\sigma = 1$. A critical choice in the definition of SPI is the probability distribution onto which the moving accumulated rainfall is fitted. A standard approach in the computation of SPI is to use a gamma distribution:

$$g(x) = \frac{1}{\beta^\alpha \Gamma(\alpha)} x^{\alpha-1} e^{-\frac{x}{\beta}} \quad (1)$$

where x represents the accumulated distribution over the time scale of interest and the gamma function $\Gamma(\alpha)$ is defined as

$$\Gamma(\alpha) = \int_0^\infty y^{\alpha-1} e^{-y} dy \quad (2)$$

In equation (1), α is a shape parameter, which represents the skewness of the distribution. Larger values of the parameter α correspond to more symmetric distributions, while smaller α 's correspond to distributions with longer tails of extreme positive values. The rate (or inverse scale parameter) β determines, at any given α , a shift in the mean value of the accumulated rainfall. The analysis of long historical records demonstrate that using the gamma distribution allows one to characterize the rainfall regimes over the wide range of climatic regimes observed in Africa (Husak et al., 2007). Small values of α , $\alpha < 5$, correspond to areas that are usually dry but can receive occasional events of intense rainfall. Large values of α , $\alpha > 25$, are observed over areas that are usually wet, and are more unlikely to experience long periods without rainfall.

It is important to note that, in regions with high probability of zero rainfall (i.e. arid climates) or, vice versa, in humid areas with strong seasonal patterns in their rainfall regime, two cases that are very well represented by the climate zones in which SADC countries are found, the gamma distribution does not fit the frequency distribution of the historical rainfall adequately (https://edo.jrc.ec.europa.eu/documents/factsheets/factsheet_spi.pdf) and other distributions, e.g. Weibull, could be preferred. Nonetheless, we decide not to deviate from the original definition of SPI and mitigate anomalous behaviours by fitting also the location parameter of the gamma distribution.

Since the lack or the excess of rainfall have different impacts on the environment depending on their duration, the choice of SPI time scale depends on the process of interest. We include in our ECI for the SADC region the 3-month SPI, or SPI3. 3-month SPI reflects short- and medium-term moisture conditions and provides a seasonal estimate of precipitation, also relevant for cropping conditions.

7.2.3 Heat Component (SHI)

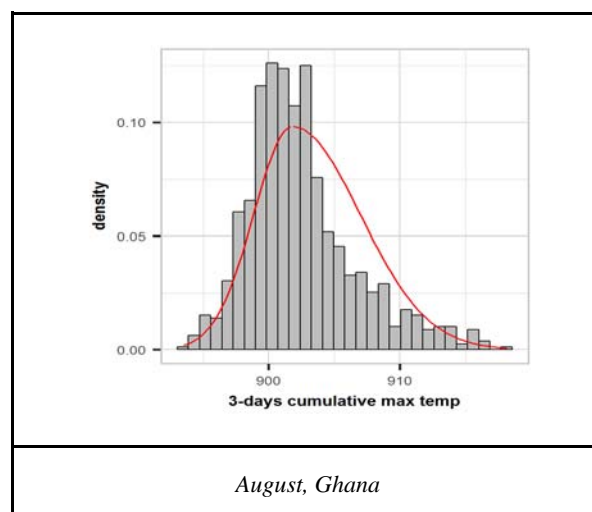
We define a standardized index for daily cumulative maximum temperatures, called Standardized Heat-wave Index (SHI), to be integrated in our multi-hazard ECI. SHI is derived as a modification of an existing heat-wave index (Russo et al., 2014) widely adopted for monitoring heat waves.

Heat-wave indicators have been mainly developed with the aim of capturing the potential impact of heat on specific sectors (e.g. agriculture, health, wildfires, transport, power generation, and distribution). Each definition of a heat wave, necessarily takes into account the specific nature of the sector of interest. For example, from the point of view of pure climatological statistics, the occurrence of peak temperatures may already represent a relevant indicator (Frich et al., 2002). However, the effect of extreme temperatures on plant phenology, for example, must take into account the possibility of exceeding specific thresholds (Koppe et al., 2004; Reyer et al., 2013).

For the purpose of ECI, a standardized index for daily cumulative maximum temperatures called Standardized Heat-wave Index (SHI) is defined. SHI is derived as a modification of an existing heat-wave index⁶, already adopted for monitoring heat waves. The computation of SHI, which is analogous to that of SPI, proceeds as follows.

1. Computing the total value of a moving cumulative maximum of daily temperatures for a time scale of interest, i.e. the past 3 days.
2. Fitting the resulting moving cumulative maxima onto a suitable theoretical distribution to establish a relation between each value of cumulative maximum daily temperature and its probability.
3. Applying the inverse normal distribution to the values of probability which correspond to each value of the cumulative maximum daily temperature, to finally compute the values of SHI corresponding to the same probability.

As for SPI, a critical choice in the definition of SHI is the theoretical probability distribution onto which the moving cumulative maximum daily temperature is fitted. In this case, literature does not give a clear indication of the best possible choice. This can be easily understood by looking at Figure 45, which displays examples of empirical distributions of the cumulative maximum daily temperature from the dataset. Depending on the month and the location, very different types of distribution are obtained, ranging from right- to left-skewed distributions (Figure 45).



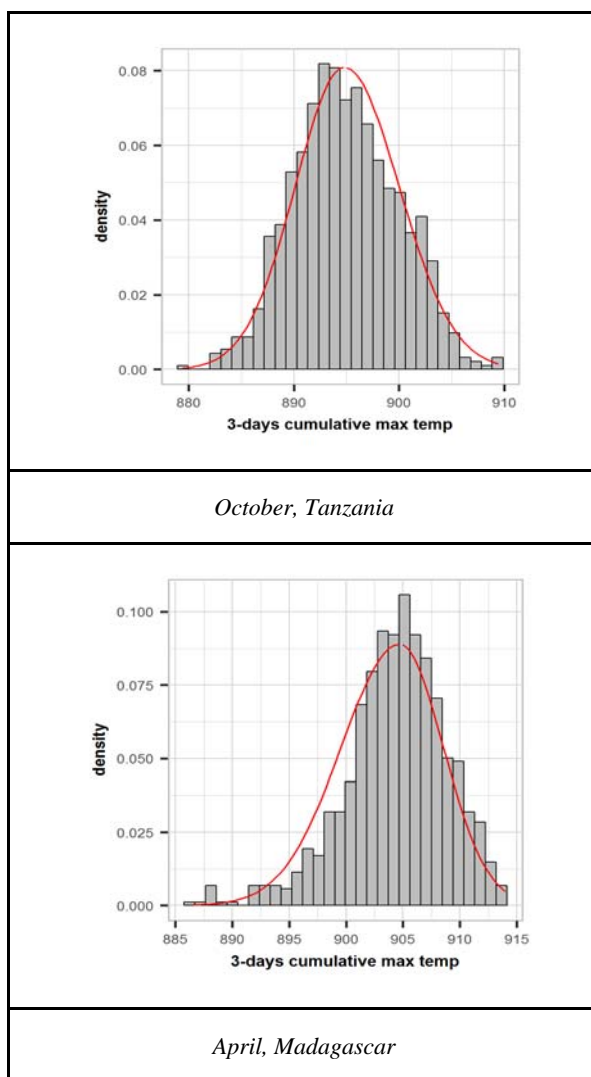


Figure 45: Examples of empirical distributions for 3-days cumulative maximum daily temperature, along with fitted split-normal distributions.

The so called Split Normal distribution is adopted to fit all the empirical distributions, and is defined as follows:

$$g(x) = \begin{cases} A \exp\left(-\frac{(x-\mu)^2}{2\sigma_1^2}\right), & x < \mu \\ A \exp\left(-\frac{(x-\mu)^2}{2\sigma_2^2}\right), & x \geq \mu \end{cases}, \quad (3)$$

$$A = \sqrt{\frac{2}{\pi}}(\sigma_1 + \sigma_2)^{-1}$$

Where x represents the cumulative maximum daily temperature over the time scale of interest, μ is the empirical mean of the sample. Finally, σ_1 and σ_2 are the empirical standard deviations of the two virtual distributions obtained by symmetrizing with respect to μ the two sides of the sample distribution, where $x < \mu$ and $x \geq \mu$.

Through the two different standard deviations, it is possible to account for the different properties of the observed distribution, with special regard to skewness. Such a SHI can be adopted for the definition of a multi-hazard index, in combination with other normally-distributed hazard indicators.

7.2.4 Wind Component (SWI)

We introduce a novel Standardized Wind Index (SWI) to be incorporated in our ECI, coherent in its formulation the other single-hazard indicators SPI and SHI.

Most of the indicators available in literature for describing extreme wind events can be found under the name of Storm Severity Index (SSI), albeit with widely different definitions (see for instance, Leckebush et al., (2008), Pinto et al., (2012), and Becker et al., (2015) among others). Nonetheless, none of the existing indices satisfies the requirement of coherency with SPI and SHI, on which our multi-hazard extreme climate index is based.

For our purposes, we chose to calculate SWI using the maximum daily wind speed instead of analyzing its latitudinal and longitudinal components separately.

The formal definition of our SWI closely resembles that of SPI. As for SPI, a standardized wind speed can be obtained by calculating the difference from the mean wind speed for a specified time period divided by its standard deviation. However, the distribution of wind speed is not normally distributed, but it is skewed with a long tail towards higher wind speeds, which is typically described by a Weibull distribution (Stevens et al., 1979), with parameters depending on the location. Therefore, to compute "standardized" deviations, a transformation needs to be applied to the wind speed values so that their distribution can be considered "normal" to a predetermined degree of approximation.

The computation of the SWI closely resembles that of SPI:

1. Fitting all the data from a given month (e.g. all the August's in the baseline period) and location onto the Weibull distribution and find month- and site-specific parameters.
2. Applying the resulting month- and site-specific Weibull distribution on the data to establish a relation between each value of wind speed and its probability.
3. Applying the inverse normal distribution technique on the values of probability associated to each value of wind speed to compute the value of the standardized wind index which corresponds to the same probability.

It is important to highlight here that the index obtained so far has two tails, with negative and positive values. However, its left tail, i.e. very low wind with small probability, is of no interest from the perspective of identifying extreme wind events that intuitively occur at very high wind speed. Nonetheless, for coherency with the other standardized indicators and guarantee certain properties to ECI (described below) we keep both tails, and interpret or neglect low wind events on a case-by-case basis.

7.2.5 Three-component ECI

ECI describes the nature of extreme climate events by incorporating two crucial aspects: 1. the intensity of the event, which indicates whether an event is extreme or not; and 2. the type of event, through the contribution of each hazard indicator to the overall intensity of the index. The mathematical definition of ECI results in a Chi-squared probability distribution function, making it suitable to identify extremes in an intuitive, statistically-sound manner.

In the definition of the ECI, we identified a mathematical approach to include the different components (climatological variables) into a single index. ECI is in fact composed of three standardized single-hazard indicators representing different climatological variables, i.e. SPI3, SHI, and SWI. Another important property aspect that is accounted for in ECI is that it should not suffer changes in

its mathematical properties when taking into account more single-hazard indicators, ensuring scalability and flexibility.

Assuming that each single-hazard indicator has a standard normal distribution (as in the case of SPI3, SHI, and SWI), it is thus intuitive to mathematically define ECI as the sum of squares of these indicators, which yields in turn a standardized index. Furthermore, under the hypothesis of mutually uncorrelated and independent single-hazard indices x_k , we define ECI as:

$$ECI_{(x_1, x_2, \dots, x_n)} = \sqrt{\sum_{k=1}^n x_k^2} \quad (4)$$

The resulting ECI has a well-defined Chi-squared probability distribution function $\chi(n)$, with n depending upon the number of single-hazard indices included. ECI can be therefore used to identify extremes after defining a suitable threshold above which events are held as extremes. In other words, extreme events can be easily set referring to theoretical percentiles of the $\chi(n)$ probability distribution. For example, adopting a well-established practice in climatology, an event can be considered extreme when its probability of occurrence is lower than 4% (or equivalent to a 1-in-25 year event return period). For the standardized single-hazard indicators, this 4% probability corresponds to deviations larger than roughly 2 standard deviations from the mean.

However, it is important to remark that climatological variables can hardly be considered independent. Several feedback loops interconnect the environmental compartments influencing climate and weather: it is thus reasonable to assume that our single-hazard indicators SPI3, SHI, and SWI, have a certain degree of mutual dependence and correlation. Thus, the ECI definition can be generalized to the case of n correlated standard normal-distributed single-hazard indices $x(t) = (x_1(t), x_2(t), \dots, x_n(t))$, resulting in:

$$ECI_x = \sqrt{x^T \Sigma^{-1} x} \quad (5)$$

Which in the case of our single-hazard indices is still $\chi(n)$ -distributed. Furthermore, this approach prevents an overestimation of the effect of strongly correlated variables. For the case of SPI3, SHI, and SWI, our three-component ECI is thus defined as:

$$ECI = \sqrt{C_{11}SPI3^2 + C_{12}SPI3 \cdot SHI + C_{22}SHI^2 + C_{23}SHI \cdot SWI + C_{13}SPI3 \cdot SWI + C_{33}SWI^2} \quad (6)$$

Where C_{ij} stands for the covariance coefficients measuring the joint variability of each combination of single-hazard indicators.

It is rather straightforward to make a parallelism between our ECI definition and polar coordinates, where the value of ECI corresponds to the distance of the point from the origin, i.e. the radius, and ϕ is the angle between the radius and one of the axes. In this representation, extremes are defined as those events with radius > 2 . The second polar coordinate, ϕ , identifies the type of extreme, i.e. indicates which component contributes the most to the radius value.

A schematic illustration of the three-component ECI in polar coordinates is shown in Figure 46.

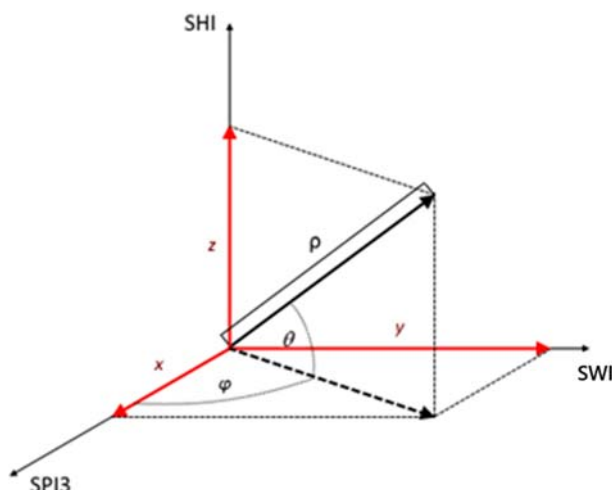


Figure 46: Schematic illustration of the three-component ECI in polar coordinates.

A classification of the intensity of events associated with ECI is provided in Table 7. As mentioned above, the intensity, i.e. the value, of ECI follows a Chi-squared distribution. Based on the resulting distribution of ECI, follows that values smaller than 2.5 are associated with normal fluctuations of the climate system. Values of ECI between 2.5 and 2.75 are associated with events of moderate intensity. Values between 2.75 and 3 are associated with severe events. Extreme events are associated with values of ECI larger than 3.

Table 7: Classification of the severity of events associated with ECI.

ECI value	Climate condition
>3	Extreme
2.75 to 2.99	Severe
2.5 to 2.74	Moderate
0.0 to 2.5	Near normal

7.3 Results

7.3.1 Examples of SWI analyses of storm footprints

Our newly introduced SWI is a meaningful indicator of wind storms in the SADC area: is effective both when used as a mapped indicator to visualize storm/cyclone footprints and when aggregated as a timeseries, to show seasonal patterns over an area of interest.

The effectiveness of SWI as a high-wind event indicator is here discussed in both contexts, i.e. to study the footprint of some major tropical cyclone events, and then spatially aggregated to identify storm events by setting a threshold, selecting Madagascar as study area.

Within the SADC countries, those facing the Indian Ocean are in fact particularly exposed to tropical cyclones. The Southwest Indian Ocean Region is, in fact, one of the most active areas in the world in terms of tropical cyclone formation. For island states such as Madagascar, Seychelles, Reunion and Mauritius, geographic predisposition reinforces their vulnerability to this type of events. According to

recent research, Madagascar exhibits the biggest storm damages in today's climate, amounting to \$17m per year. This figure is projected to increase to \$81m per year by 2100.

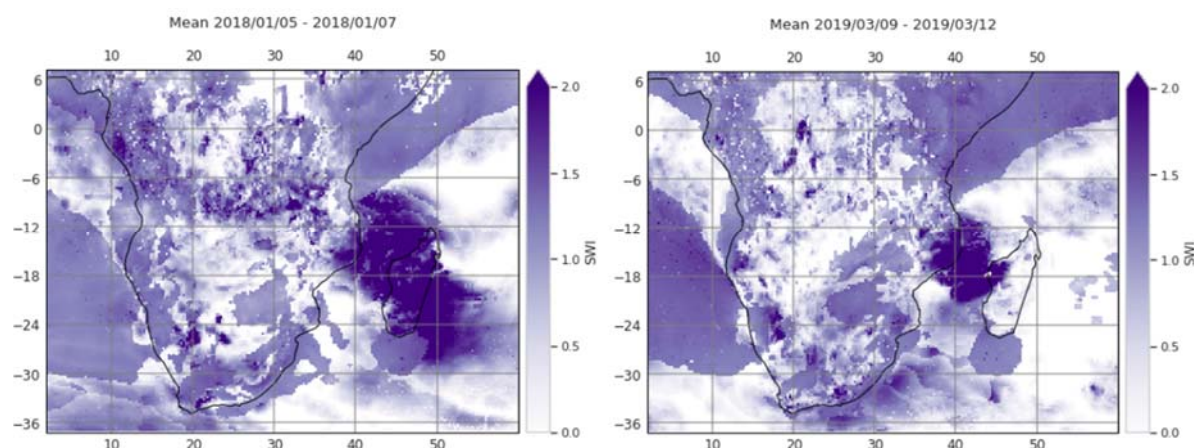


Figure 47: Footprints of the tropical cyclones Ava (started on 2018/01/05, on the left) and Idai (started on 2019/03/09, on the right), represented through SWI.

In Figure 47, SWI is shown in correspondence of two historical events, namely the tropical cyclones Ava (January 2018) and Idai (March 2019). SWI captures the extent of the two storms correctly, with one covering the entire island of Madagascar, the other involving the eastern coast of Madagascar, and Malawi, Mozambique, and Zimbabwe on mainland Africa. SWI provides further insight on the extraordinary severity of these two events, showing wind speeds that exceeded two standard deviations during the event ($SWI > 2$).

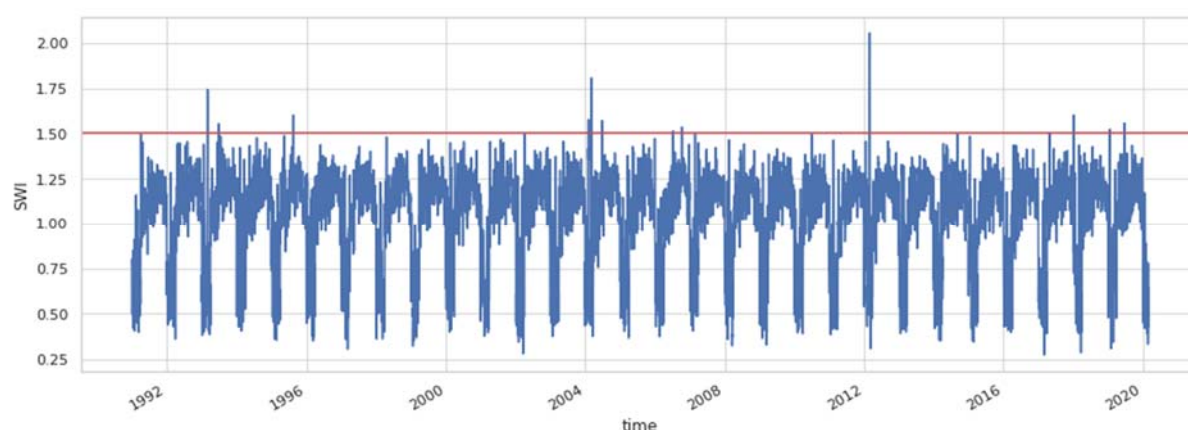


Figure 48: Daily time series of SWI, median value over Madagascar and surrounding waters. The red line marks $SWI = 1.5$.

When analysing the time series of median daily values of SWI during the baseline period (1991-2020) over Madagascar, it can be seen that SWI follows a marked periodical pattern, with generally lower values from January to May and higher values during the rest of the year. There are however some exceptionally high values especially during the low-SWI season, that interestingly roughly coincide with tropical cyclone season. This latter series is then compared with events in the disaster event database of Reliefweb.

We extracted the dates when the median SWI over Madagascar is > 1.5 , i.e. when the maximum daily wind speed exceeds one and a half standard deviations, corresponding to 14 events (namely in the

late February-early March 1993, late June 1993, August 1995, early February 2004, March 2004, June 2004, July 2004, October 2006, February 2007, late February-early March 2012, April 2017, early January 2018, mid-January 2019, June 2019). It is interesting to note that this approach classifies Ava (early January 2018) as storm, but not Idai (March 2019): this is a consequence of extracting the median over Madagascar, which was only partially impacted by Idai as it mostly involved its eastern coast (46, left panel).

As for the other events, Reliefweb does not include events prior to 1994, and the historical records seem to have some gaps up to more recent years. Nonetheless, two cyclones were recorded in March 2004 and June 2004, coinciding with our results, but not in July 2004, apparently being a false positive. Other false positives are those of October 2006, April 2017 and mid-January 2019, that nonetheless show high wind conditions in our mapped SWI, while the rest coincide with actual events (for instance, the event occurred in late February-early March 2012 is distinctly visible in the time series). As for the false negatives, we noticed that they were mostly local events, i.e. that did not involve large portions of Madagascar, thus they could have been disregarded by using the median as selection criterion.

SWI is thus a meaningful indicator of storms in the SADC area, yet care must be applied in selecting the most suitable method for spatial aggregation when large territories are considered. Furthermore, a prospective application of SWI on seasonal forecasts could be a promising tool for early warning of storms and cyclones.

7.3.2 ECI application for extreme detection

ECI proves to be very effective in detecting extreme events in the SADC region, and makes it possible to visualize the events' footprints with high spatial resolution. Unpacking ECI into its three components allows to identify temporal overlaps and potential synergies of weather events of different nature, potentially worsening their impact and related risk.

We show and analyse three emblematic events as an example of the application of ECI on different temporal scales: an extreme drought occurred in Angola in January 2001 (Figure 49), a heat wave in South Africa during 1-10 January 2016 (Figure 50), and a tropical cyclone that hit Mozambique on 25th April, 2019 (Figure 51); these events are matched by as many entries in the EM-DAT International Disaster Database.

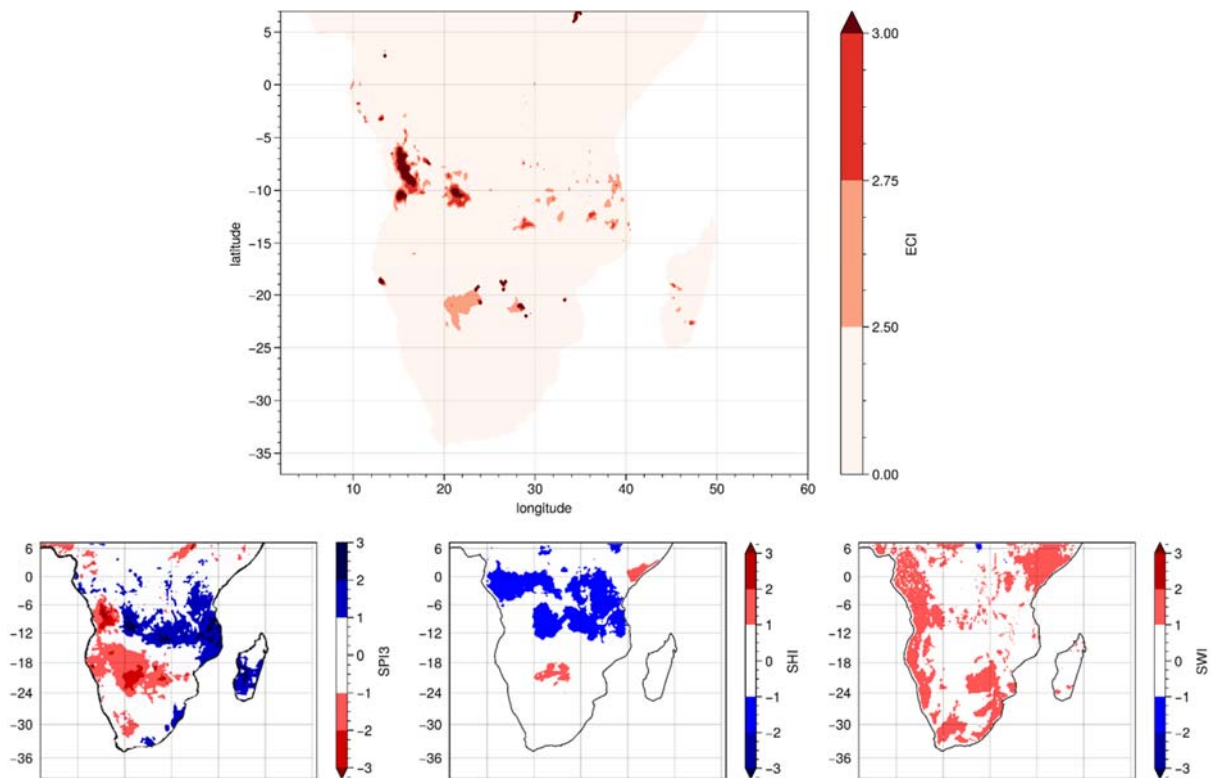


Figure 49: ECI (upper panel) and its three components (lower panels, left to right: SPI3, SHI, and SWI) averaged over January, 2001. The color scale of ECI (upper panel) matches the classification of the intensity of events in Table 7.

In Figure 49 (upper panel), not only ECI correctly detects the extreme drought that occurred in the Cuanza Sul province, North Angola, in January 2001, but also signals another event: the floods striking Zambia and Mozambique in the same period. SPI3 (Figure 49, lower left panel) is here key to provide further insights on both events.

Angola frequently experiences drought events, affecting the livelihoods and food security of millions of people, especially in its southern regions. Nonetheless, ECI highlights the presence of an extreme event, with peak values > 5 , in a northern area that matches the Cuanza Sul province (Figure 49, upper panel). When looking at the three components separately, SPI3 in this area appears to be remarkably low (Figure 49, lower left panel); no significant patterns can be identified in the other two components, confirming that ECI is signalling a severe drought event.

ECI also reports another event that occurred at the same latitudes as the Angola one, but on eastern areas, drawing a band that stretches up to Mozambique (upper panel). Here, SPI3 reports an unusual abundance of precipitation (lower left panel), corresponding to severe rainfall and flooding.

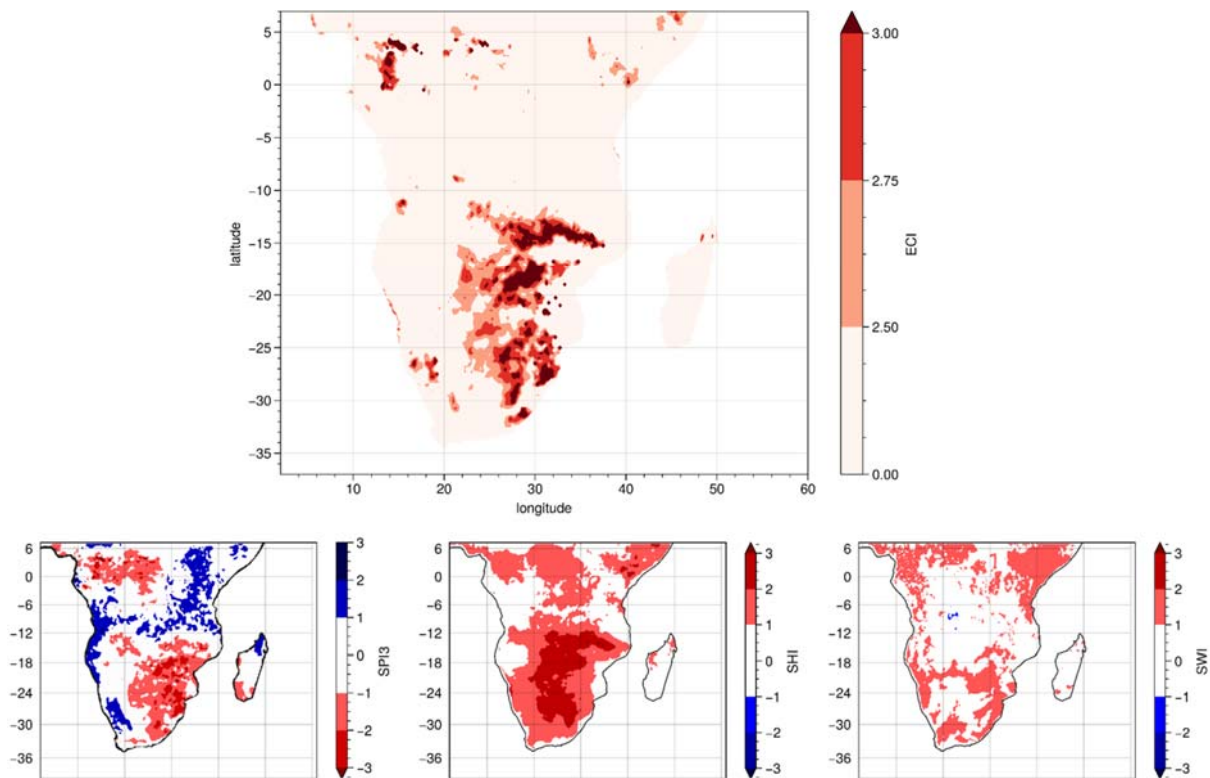


Figure 50: ECI (upper panel) and its three components (lower panels, left to right: SPI3, SHI, and SWI) averaged over 1-10 January, 2016. The color scale of ECI (upper panel) matches the classification of the intensity of events in Table 7.

In Figure 50 (upper panel), ECI reveals that the heat wave that occurred in South Africa in January 2016 exacerbated the effects of an underlying dry period, jointly resulting in an extreme event (even $ECI > 3$) with a large footprint, involving also Botswana, Zimbabwe, and Zambia.

The synergy of the two events is visible through the analysis of the single components: SPI3 presents in fact low values in the southern-east section of the SADC region (lower left panel), while SHI (lower central panel) shows high values in the entire south-SADC region.

In Figure 51: ECI (upper panel) and its three components (lower panels, left to right: SPI3, SHI, and SWI) for 25th April, 2019. The colour scale of ECI (upper panel) matches the classification of the intensity of events in Table 7. (upper panel) ECI makes clearly visible the landfall of tropical cyclone Kenneth in Mozambique, with peak values of about 9, signalling an extreme event of exceptional intensity. Again, ECI captures another extreme event: an ongoing drought in Southern Angola.

Among the three components, the prominent one is SWI, reporting the cyclone; nonetheless, the other two components reveal that the ongoing dry period in Angola (lower left panel; note that SPI3 is based on 3-month cumulative rainfall) was further exacerbated locally by high temperatures, as shown by SHI (lower central panel).

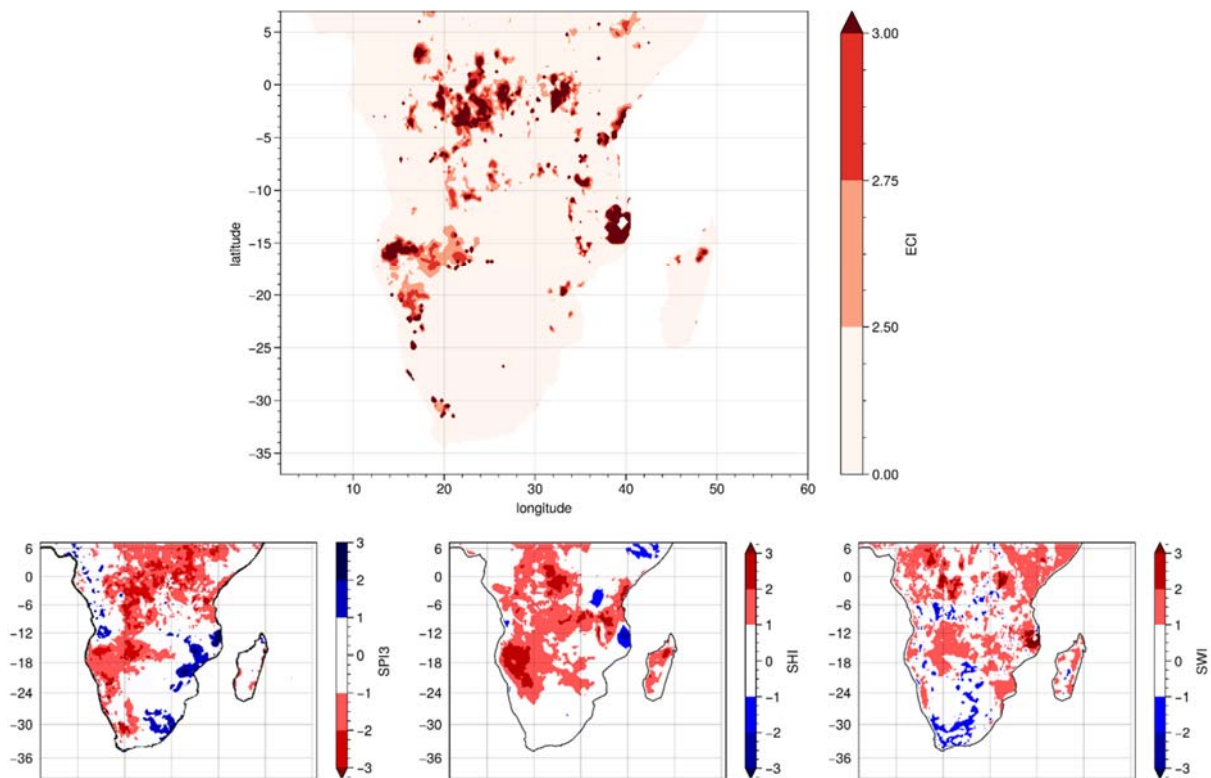


Figure 51: ECI (upper panel) and its three components (lower panels, left to right: SPI3, SHI, and SWI) for 25th April, 2019. The colour scale of ECI (upper panel) matches the classification of the intensity of events in Table 7.

7.4 Summary

Amigo introduced a flexible multi-hazard Extreme Climate Index (ECI) to describe the climate risk caused by extreme events, shifting the focus from weather risk management to the broader scope of managing the risk associated with climate change. Alongside well-established indicators of drought and heat waves, a tailored indicator for extreme wind events was developed and incorporated into our implementation of ECI for the SADC region.

The application of ECI is of particular interest in SADC countries, highly exposed to the impacts of climate change and to meteorological extremes and at the same time characterized by poor livelihoods, reliant on rainfed agriculture, thus particularly vulnerable to climate-related disasters.

ECI proves to be very effective in detecting extreme events in the SADC region, and makes it possible to visualize the events' footprints with high spatial resolution. Furthermore, unpacking ECI back into its three components allows to identify temporal overlaps and potential synergies of weather events of different nature, potentially worsening their impact and related risk.

Conclusion

The goal of this task is to contribute to a better knowledge of how climate variability affects the quality of seasonal forecasts, decadal predictions and climate projections in terms of extreme event characterization and evolution.

The evaluation of Regional Climate Models (RCMs) skill in capturing the most extreme daily events shows a weak dependence on the driving General Circulation Models, evidenced by the limited variability between each RCM (Section 2). This limited variability, combined with the limited size of the model ensemble, leads to a reduced uncertainty representation. The analysis of projected changes in the future climate provides a solid signal of warming with model uncertainty over some areas, while the precipitation result is characterized by model uncertainty across the whole SADC region.

A review of the impacts of climate extremes is then presented in Section 3, including an investigation of new methodologies to determine related risks. Machine Learning has proven to be an efficient method for improving extreme events forecasts and can be considered valuable in the context of FOCUS-Africa for improved service provision.

Going further to Section 4, a characterisation of the rainfall extremes dynamics in seasonal forecasts and climate projections is performed, assessing the teleconnections between climate modes (ENSO and IOD) and different indices for rainfall extremes. The analysis of the CMIP6 models' ability to represent the ENSO teleconnection to rainfall over Africa shows that these models do well at capturing the austral-summer dipole relationship observed over southern and East Africa during El Niño and La Niña events. This teleconnection is expected to change in the future, and this change is subjected to regional variation. Many models project a strengthening of the relationship under future climate change, while other models indicate a weakening or even a reversal of the expected DJF rainfall signal over southern Africa during El Niño/La Niña events.

This analysis is particularly significant for the agricultural sector, as crop productivity strongly depends on the variability of the growing season. Therefore, in Section 5 we analysed the nature of crop growing season rainfall extremes during anomalous years in seasonal forecasts. Results show that seasonal forecast models still have some limitations in predicting the spatial distributions of rainfall extremes across landscapes with various ecosystems. However, they more or less capture the observed response of anomalies of seasonal extremes during ENSO and IOD episodes.

In addition, in Section 6 the showcase for Lake Malawi is presented, to provide a generalised understanding of the characteristics and synoptic drivers of two types of extremes. Local extreme rainfall occurs predominantly under easterly moisture flow regime and particularly under conditions when flow from tropical Indian Ocean is combined with flow from the subtropics. Region-average extreme rainfall instead occurs during conditions of westerly moisture flow regime, as manifested by intensities and frequency of extreme events.

Finally, to describe the climate risk generated by severe weather events, a specific multi-hazard Extreme Climate Index ECI is defined (Section 7), which is particularly effective in detecting extreme events in the SADC region and enables high spatial resolution visualization of the events' footprints. The splitting of this index into its three components (precipitation, temperature and wind) helps in the identification of temporal overlaps and synergies between different types of weather events, that could worsen their impact and associated risk.

Bibliography

- [I] ADB, 2019. Southern Africa Economic Outlook 2019: Macroeconomic performance and prospects, African Development Bank, ISBN 978-9938-882-98-8. https://www.afdb.org/fileadmin/uploads/afdb/Documents/Publications/2019AEO/REO_2019_-_Southern_africa.pdf
- [II] AgERA5, 2021, Copernicus Climate Change Service (C3S), Fifth generation of ECMWF atmospheric reanalysis of the global climate for agriculture and agro-ecological studies. Copernicus Climate Change Service Climate Data Store (CDS), July-2021.
- [III] Ahmed, S. M. (2020). Impacts of drought, food security policy and climate change on performance of irrigation schemes in Sub-saharan Africa: The case of Sudan. *Agricultural Water Management*, 232, 106064. doi:<https://doi.org/10.1016/j.agwat.2020.106064>
- [IV] Allen, M. R., & Ingram, W. J. (2002). Constraints on future changes in climate and the hydrologic cycle. *Nature*, 419 (6903), 224–232. <https://doi.org/10.1038/nature01092>
- [V] Anderson, W., Taylor, C., McDermid, S., Ilboudo-Nébié, E., Seager, R., Schlenker, W., . . . Markey, K. (2021). Violent conflict exacerbated drought-related food insecurity between 2009 and 2019 in sub-Saharan Africa. *Nature Food*, 2(8), 603-615. doi:10.1038/s43016-021-00327-4
- [VI] Ayanlade, A., Oluwaranti, A., Ayanlade, O. S., Borderon, M., Sterly, H., Sakdapolrak, P., . . . Ayinde, A. F. O. (2022). Extreme climate events in sub-Saharan Africa: A call for improving agricultural technology transfer to enhance adaptive capacity. *Climate Services*, 27. doi:10.1016/j.cliser.2022.100311
- [VII] Bako, M. M., Mashi, S. A., Bello, A. A., & Adamu, J. I. (2020). Spatiotemporal analysis of dry spells for support to agriculture adaptation efforts in the Sudano-Sahelian region of Nigeria. *SN Applied Sciences*, 2(8). doi:10.1007/s42452-020-3161-x
- [VIII] Batté, L. and Déqué, M.: Randomly correcting model errors in the ARPEGE-Climate v6.1 component of CNRM-CM: applications for seasonal forecasts, *Geosci. Model Dev.*, 9, 2055–2076, <https://doi.org/10.5194/gmd-9-2055-2016>, 2016.
- [IX] Becker, N., Nissen, Katrin M., and Ulbrich, U. (2015). A storm severity index based on return levels of wind speeds. *Geophysical Research Abstracts Vol. 17*, EGU2015-5699, 2015 EGU General Assembly 2015
- [X] Beillouin, D., Schauburger, B., Bastos, A., Ciais, P., & Makowski, D. (2020). Impact of extreme weather conditions on European crop production in 2018. *Philos Trans R Soc Lond B Biol Sci*, 375(1810), 20190510. doi:10.1098/rstb.2019.0510
- [XI] Bruno Soares M, Daly M, Dessai S (2018) Assessing the value of seasonal climate forecasts for decision-making. *Wiley Interdiscip Rev Clim Change*.
- [XII] Camberlin, P., Janicot, S. and Poccarr, I., 2001. Seasonality and atmospheric dynamics of the teleconnection between African rainfall and tropical sea-surface temperature: Atlantic vs. ENSO. *International Journal of Climatology: A Journal of the Royal Meteorological Society*, 21(8), pp.973-1005, <https://doi.org/10.1002/joc.673>.
- [XIII] Chatzopoulos, T., Pérez Domínguez, I., Zampieri, M., & Toreti, A. (2020). Climate extremes and agricultural commodity markets: A global economic analysis of regionally simulated events. *Weather and Climate Extremes*, 27. doi:10.1016/j.wace.2019.100193
- [XIV] Chikoore, H., & Jury, M. R. (2021). South African drought, deconstructed. *Weather and Climate Extremes*, 33. doi:10.1016/j.wace.2021.100334
- [XV] CNPC (National Commission for Civil Protection) (2016). Droughts in Angola 2012–2016. Post Disaster Needs Assessment Report. PNUD, Luanda, Angola
- [XVI] Contractor, S., Donat, M. G., Alexander, L. V., Ziese, M., Meyer-Christoffer, A., Schneider, U., ... Vose, R. S. (2020). Rainfall Estimates on a Gridded Network (REGEN) – a global land-based gridded dataset of daily precipitation from 1950 to 2016. *Hydrology and Earth System Sciences*, 24(2), 919–943. <https://doi.org/10.5194/hess-24-919-2020>
- [XVII] Deryng, D., Conway, D., Ramankutty, N., Price, J., & Warren, R. (2014). Global crop yield response to extreme heat stress under multiple climate change futures. *Environmental Research Letters*, 9(3), 034011. doi:10.1088/1748-9326/9/3/034011
- [XVIII] Dossou-Yovo, E., Zwart, S., Kouyaté, A., Ouédraogo, I., & Bakare, O. (2018). Predictors of Drought in Inland Valley Landscapes and Enabling Factors for Rice Farmers' Mitigation Measures in the Sudan-Sahel Zone. *Sustainability*, 11(1). doi:10.3390/su11010079

- [XIX] Edwards, D. C. and McKee, T.B., 1997: Characteristics of 20th century drought in the United States at multiple time scales. *Climatology Report 97-2*, Department of Atmospheric Science, Colorado State University, Fort Collins, Colorado.
- [XX] Endris, H.S., Lennard, C., Hewitson, B., Dosio, A., Nikulin, G. and Artan, G.A., 2019. Future changes in rainfall associated with ENSO, IOD and changes in the mean state over Eastern Africa. *Climate dynamics*, 52(3), pp.2029-2053, <https://doi.org/10.1007/s00382-018-4239-7>.
- [XXI] Ficchi, A., Cloke, H., Neves, C., Woolnough, S., de Perez, E.C., Zsoter, E., Pinto, I., Meque, A., Stephens, E., 2021. Beyond El Niño: unsung climate modes drive African floods. *Weather Clim. Extremes* 33, 100345.
- [XXII] Findell, K. L., Sutton, R., Caltabiano, N., Brookshaw, A., Heimbach, P., Kimoto, M., . . . Wang, L. (2022). Explaining and Predicting Earth System Change: A World Climate Research Programme Call to Action. *Bulletin of the American Meteorological Society*. doi:10.1175/bams-d-21-0280.1
- [XXIII] Frich, P., et al. (2002) Observed Coherent Changes in Climatic Extremes during the Second Half of the Twentieth Century. *Climate Research*, 19, 193-212. <http://dx.doi.org/10.3354/cr019193>
- [XXIV] Funk, C., Peterson, P., Landsfeld, M., Pedreros, D., Verdin, J., Shukla, S., ... Michaelsen, J. (2015). The climate hazards infrared precipitation with stations—a new environmental record for monitoring extremes. *Scientific Data*, 2(1), 150066. <https://doi.org/10.1038/sdata.2015.66>
- [XXV] Gebrechorkos, S. H., Pan, M., Beck, H. E., & Sheffield, J. (2022). Performance of state-of-the-art C3S European seasonal climate forecast models for mean and extreme precipitation over Africa. *Water Resources Research*, 58, e2021WR031480. <https://doi.org/10.1029/2021WR031480>
- [XXVI] Giannakaki, P., Barton, Y., von Waldow, H., Chevalier, C., Pfahl, S., & Martius, O. (2016). Clustering of Regional-Scale Extreme Precipitation Events in Southern Switzerland. *Monthly Weather Review*, 144(1), 347-369. doi:10.1175/mwr-d-15-0205.1
- [XXVII] Giorgi, F., Coppola, E., Teichmann, C., & Jacob, D. (2021). Editorial for the CORDEX-CORE Experiment I Special Issue. *Climate Dynamics*, 57(5–6), 1265–1268. <https://doi.org/10.1007/s00382-021-05902-w>
- [XXVIII] Glantz, M.H., Ramirez, I.J. Reviewing the Oceanic Niño Index (ONI) to Enhance Societal Readiness for El Niño's Impacts. *Int J Disaster Risk Sci* 11, 394–403 (2020). <https://doi.org/10.1007/s13753-020-00275-w>
- [XXIX] Gnitou, G. T., Tan, G., Niu, R., & Nooni, I. K. (2021). Assessing Past Climate Biases and the Added Value of CORDEX-CORE Precipitation Simulations over Africa. *Remote Sensing*, 13(11), 2058. <https://doi.org/10.3390/rs13112058>
- [XXX] Guha-Sapir, D., Below, R., Ph. Hoyois - EM-DAT: The CRED/OFDA International Disaster Database – www.emdat.be – Université Catholique de Louvain – Brussels – Belgium. Gutiérrez, J. ., Jones, R. G., Narisma, G. T., Alves, L. M., Amjad, M., Gorodetskaya, I. V., ... Yoon, J.-H. (n.d.). The Physical Science Basis. Contribution of Working Group I to the Sixth Assessment Report of the Intergovernmental Panel on Climate Change. In *Climate Change 2021*.
- [XXXI] Harris, I., Jones, P. D., Osborn, T. J., & Lister, D. H. (2014). Updated high-resolution grids of monthly climatic observations - the CRU TS3.10 Dataset. *International Journal of Climatology*, 34(3), 623–642. <https://doi.org/10.1002/joc.3711>
- [XXXII] Harris, I., Osborn, T.J., Jones, P., Lister, D., 2020. Version 4 of the CRU TS monthly highresolution gridded multivariate climate dataset. *Science Data*, 7, 109. <https://doi.org/10.1038/s41597-020-0453-3>.
- [XXXIII] Haqiqi, I., Grogan, D. S., Hertel, T. W., & Schlenker, W. (2021). Quantifying the impacts of compound extremes on agriculture. *Hydrology and Earth System Sciences*, 25(2), 551-564. doi:10.5194/hess-25-551-2021
- [XXXIV] Hersbach, H, Bell, B, Berrisford, P, et al. (2020). The ERA5 global reanalysis. *Q J R Meteorol Soc.*, 146: 1999– 2049. <https://doi.org/10.1002/qj.3803>
- [XXXV] Hewitson, B.C. and Crane, R.G., 2006. Consensus between GCM climate change projections with empirical downscaling: precipitation downscaling over South Africa. *International Journal of Climatology: A Journal of the Royal Meteorological Society*, 26(10), pp.1315-1337.
- [XXXVI] Hoell, A., Cheng, L. Austral summer Southern Africa precipitation extremes forced by the El Niño–Southern oscillation and the subtropical Indian Ocean dipole. *Clim Dyn* 50, 3219–3236 (2018). <https://doi.org/10.1007/s00382-017-3801-z>
- [XXXVII] Hoell, A., C. Funk, T. Magadzire, J. Zinke, and G. Husak, 2015: El Niño–Southern Oscillation diversity and Southern Africa teleconnections during Austral Summer. *Clim Dyn*, 45,1583-1599
- [XXXVIII] Hoell, A., Gaughan, A.E., Magadzire, T., Harrison, L., 2021. The modulation of Daily Southern Africa precipitation by El Niño–Southern oscillation across the Summertime Wet Season. *Journal of Climate*, 34(3), pp.1115–1134. <https://doi.org/10.1175/JCLI-D-20-0379.1>.

- [XXXIX] https://edo.jrc.ec.europa.eu/documents/factsheets/factsheet_spi.pdf
- [XL] <https://reliefweb.int/disasters>
- [XLI] <https://reliefweb.int/report/mozambique/wfp-mozambique-flood-emergency-situation-report-01-jan-12-feb-2001>
- [XLII] <https://reliefweb.int/report/mozambique/mozambique-two-cyclones-idai-and-kenneth-22-may-2019>
- [XLIII] <https://reliefweb.int/report/angola/gdo-analytical-report-drought-southern-angola-october-2019>
- [XLIV] Husak, G.J., Michaelsen, J. and Funk, C. (2007), Use of the gamma distribution to represent monthly rainfall in Africa for drought monitoring applications. *Int. J. Climatol.*, 27: 935-944. <https://doi.org/10.1002/joc.1441>
- [XLV] IPCC, 2021: Climate Change 2021: The Physical Science Basis. Contribution of Working Group I to the Sixth Assessment Report of the Intergovernmental Panel on Climate Change [Masson-Delmotte, V., P. Zhai, A. Pirani, S.L. Connors, C. Péan, S. Berger, N. Caud, Y. Chen, L. Goldfarb, M.I. Gomis, M. Huang, K. Leitzell, E. Lonnoy, J.B.R. Matthews, T.K. Maycock, T. Waterfield, O. Yelekçi, R. Yu, and B. Zhou (eds.)]. Cambridge University Press. In Press.
- [XLVI] Iturbide, M., Fernández, J., Gutiérrez, J. ., Bedia, J., Cima-devilla, E., Díez-Sierra, J., ... Yelekci, Ö. (2021). Repository supporting the implementation of FAIR principles in the IPCC-WG1 Atlas. Zenodo. <https://doi.org/10.5281/zenodo.3691645>
- [XLVII] Irene Cionni, Llorenç Lledó, Verónica Torralba, Alessandro Dell'Aquila, Seasonal predictions of energy-relevant climate variables through Euro-Atlantic Teleconnections, *Climate Services*, Volume 26, 2022, 100294, ISSN 2405-8807, <https://doi.org/10.1016/j.cliser.2022.100294>
- [XLVIII] Iversen, T., Bentsen, M., Bethke, I., Debernard, J. B., Kirkevåg, A., Seland, Ø., ... Seierstad, I. A. (2013). The Norwegian Earth System Model, NorESM1-M – Part 2: Climate response and scenario projections. *Geoscientific Model Development*, 6(2), 389–415. <https://doi.org/10.5194/gmd-6-389-2013>
- [XLIX] Johnson SJ, Stockdale TN, Ferranti L, Balmaseda MA, Molteni F, Magnusson L, Tietsche S, Decremier D, Weisheimer A, Balsamo G, Keeley SP, Mogensen K, Zuo H, Monge-Sanz BM (2019) SEAS5: the new ECMWF seasonal forecast system. *Geosci Model Dev* 12(3):1087–1117.
- [L] Karypidou, M. C., Sobolowski, S. P., Katragkou, E., Sangelantoni, L., & Nikulin, G. (2022). The impact of lateral boundary forcing in the CORDEX-Africa ensemble over southern Africa. *Geoscientific Model Development Discussions*, (January), 1–36. Retrieved from <https://doi.org/10.5194/gmd-2021-348>
- [LI] King, A. D., Hudson, D., Lim, E.-P., Marshall, A. G., Hendon, H. H., Lane, T. P., & Alves, O. (2020). Sub-seasonal to seasonal prediction of rainfall extremes in Australia. *Quarterly Journal of the Royal Meteorological Society*, 146(730), 2228–2249. <https://doi.org/10.1002/qj.3789>
- [LII] Kolusu, S. R., Shamsudduha, M., Todd, M. C., Taylor, R. G., Seddon, D., Kashaigili, J. J., Ebrahim, G. Y., Cuthbert, M. O., Sorensen, J. P. R., Villholth, K. G., MacDonald, A. M., and MacLeod, D. A.: The El Niño event of 2015–2016: climate anomalies and their impact on groundwater resources in East and Southern Africa, *Hydrol. Earth Syst. Sci.*, 23, 1751–1762, <https://doi.org/10.5194/hess-23-1751-2019>, 2019.
- [LIII] Koppe, C. G., Kovats, S., Jendritzky, G., & Menne, B. (2004). *Heat Waves: Risks and Responses*. Copenhagen: World Health Organization.
- [LIV] Leckebusch, G. C., Renggli, D., & Ulbrich, U. (2008). Development and application of an objective storm severity measure for the Northeast Atlantic region. *Meteorologische Zeitschrift*, 575-587.
- [LV] Lee, D., Davenport, F., Shukla, S., Husak, G., Funk, C., Harrison, L., . . . Verdin, J. (2022). Maize yield forecasts for Sub-Saharan Africa using Earth Observation data and machine learning. *Global Food Security*, 33. doi:10.1016/j.gfs.2022.100643
- [LVI] Lenderink, G. and Fowler, H.J., 2017. Understanding rainfall extremes. *Nature Climate Change*, 7(6), pp.391-393, <https://doi.org/10.1038/nclimate3305>.
- [LVII] Lennard, C. and Hegerl, G., 2015. Relating changes in synoptic circulation to the surface rainfall response using self-organising maps. *Climate Dynamics*, 44(3), pp.861-879.
- [LVIII] Lindesay, J.A., 1988. South African rainfall, the Southern Oscillation and a Southern Hemisphere semi-annual cycle. *Journal of Climatology*, 8(1), 17–30. <https://doi.org/10.1002/joc.3370080103>.
- [LIX] Liu, B., Asseng, S., Müller, C., Ewert, F., Elliott, J., Lobell, David B., . . . Zhu, Y. (2016). Similar estimates of temperature impacts on global wheat yield by three independent methods. *Nature Climate Change*, 6(12), 1130-1136. doi:10.1038/nclimate3115
- [LX] Liu, X.; Zhou, J. Assessment of the Continuous Extreme Drought Events in Namibia during the Last Decade. *Water* 2021, 13, 2942. <https://doi.org/10.3390/w13202942>

- [LXI] Maclachlan C, Arribas A, Peterson KA, Maidens A, Fereday D, Scaife AA, Gordon M, Vellinga M, Williams A, Comer RE, Camp J, Xavier P, Madec G (2015) Global Seasonal forecast system version 5 (GloSea5): a high-resolution seasonal forecast system. *Q J R Meteorol Soc* 141(689):1072–1084.
- [LXII] Mariotti, A., Baggett, C., Barnes, E. A., Becker, E., Butler, A., Collins, D. C., . . . Albers, J. (2020). Windows of Opportunity for Skillful Forecasts Subseasonal to Seasonal and Beyond. *Bulletin of the American Meteorological Society*, 101(5), E608-E625. doi:10.1175/bams-d-18-0326.1
- [LXIII] Martius, O., Sodemann, H., Joos, H., Pfahl, S., Winschall, A., Croci-Maspoli, M., . . . Wernli, H. (2013). The role of upper-level dynamics and surface processes for the Pakistan flood of July 2010. *Quarterly Journal of the Royal Meteorological Society*, 139(676), 1780-1797. doi:https://doi.org/10.1002/qj.2082
- [LXIV] Masih, I., et al. (2014) A Review of Droughts on the African Continent: A Geospatial and Long-Term Perspective. *Hydrology and Earth System Sciences Discussions*, 11, 2679-2718. https://doi.org/10.5194/hessd-11-2679-2014
- [LXV] Mbatha Mfaniseni, W., Mnguni, H., & Mubecua Mandla, A. (2021). Subsistence Farming as a Sustainable Livelihood Approach for Rural Communities in South Africa. *African Journal of Development Studies (formerly AFFRIKA Journal of Politics, Economics and Society)*, 11(3), 55-75. doi:10.31920/2634-3649/2021/v11n3a3
- [LXVI] McKee, T.B., Doesken, N.J. and Kleist, J. (1993) The Relation of Drought Frequency and Duration to Time Scales. *Proceedings of the 8th Conference on Applied Climatology*, Anaheim, California, 17-22 January 1993, 179-184
- [LXVII] Meza, F. J., Hansen, J. W., & Osgood, D. (2008). Economic Value of Seasonal Climate Forecasts for Agriculture: Review of Ex-Ante Assessments and Recommendations for Future Research. *Journal of Applied Meteorology and Climatology*, 47(5), 1269-1286. doi:10.1175/2007jamc1540.1
- [LXVIII] Moeletsi, M.E., Walker, S. and Landman, W.A., 2011. ENSO and implications on rainfall characteristics with reference to maize production in the Free State Province of South Africa. *Physics and chemistry of the earth, parts A/B/C*, 36(14-15), pp.715-726, https://doi.org/10.1016/j.pce.2011.07.043.
- [LXIX] Molua, E.L., Mendelsohn, R.O., Akamin, A., (2020). Economic vulnerability to tropical storms on the southeastern coast of Africa. *Jamba Journal of Disaster Risk Studies*, Oct 19;12(1):676. doi: 10.4102/jamba.v12i1.676.
- [LXX] Mountain Research Initiative EDW Working Group. (2015). Elevation-dependent warming in mountain regions of the world. *Nature Climate Change*, 5(5), 424–430. https://doi.org/10.1038/nclimate2563
- [LXXI] Neiman, P. J., Gottas, D. J., White, A. B., & Moore, B. J. (2020). Extreme Precipitation Events in Northern California during Winter 2016–17: Multiscale Analysis and Climatological Perspective. *Monthly Weather Review*, 148(3), 1049-1074. doi:10.1175/mwr-d-19-0242.1
- [LXXII] Nicholson, S.E., Kim, J., 1997. The relationship of the El Niño–Southern oscillation to African rainfall. *International Journal of Climatology*, 17, pp.117–135, https://doi.org/10.1002/(SICI)1097-0088(199702)17:2<117::AID-JOC84>3.0.CO;2-O.
- [LXXIII] Nicholas Klingaman and Will Keat, 2018. El Niño 2018-19: Historical Impact Analysis. Strengthening resilience and response to crises, the UK Department for International Development.
- [LXXIV] Nicholson, S.E., Entekhabi, D. The quasi-periodic behavior of rainfall variability in Africa and its relationship to the southern oscillation. *Arch. Met. Geoph. Biocl. A*. 34, 311–348 (1986). https://doi.org/10.1007/BF02257765
- [LXXV] NOAA, 2022. Climate Indices: Monthly Atmospheric and Ocean Time-Series. Accessed 16 September 2022. https://www.cpc.ncep.noaa.gov/data/indices/ersst5.nino.mth.91-20.ascii.
- [LXXVI] Ojara, M. A., Lou, Y., Aribo, L., Namumbya, S., & Uddin, M. J. (2020). Dry spells and probability of rainfall occurrence for Lake Kyoga Basin in Uganda, East Africa. *Natural Hazards*, 100(2), 493-514. doi:10.1007/s11069-019-03822-x
- [LXXVII] Panitz, H.-J., Dosio, A., Büchner, M., Lüthi, D., & Keuler, K. (2014). COSMO-CLM (CCLM) climate simulations over CORDEX-Africa domain: analysis of the ERA-Interim driven simulations at 0.44° and 0.22° resolution. *Climate Dynamics*, 42(11–12), 3015–3038. https://doi.org/10.1007/s00382-013-1834-5
- [LXXVIII] Pepler, A. S., Díaz, L. B., Prodhomme, C., Doblas-Reyes, F. J., & Kumar, A. (2015). The ability of a multi-model seasonal forecasting ensemble to forecast the frequency of warm, cold and wet extremes. *Weather and Climate Extremes*, 9, 68–77. https://doi.org/10.1016/j.wace.2015.06.005

- [LXXIX] Pinto, J. G., Karremann, M. K., Born, K., Della-Marta, P. M., and Klawa, M. 2012: Loss potentials associated with European wind-storms under future climate conditions, *Clim. Res.*, 54, 1–20, <https://doi.org/10.3354/cr01111>
- [LXXX] Priestley, M. D. K., Pinto, J. G., Dacre, H. F., & Shaffrey, L. C. (2017). The role of cyclone clustering during the stormy winter of 2013/2014. *Weather*, 72(7), 187-192. doi:<https://doi.org/10.1002/wea.3025>
- [LXXXI] Ramirez-Villegas, J., Ghosh, A., Craparo, S., Thornton, P., Manvatkar, R., Bogart, B., & Läderach, P. (2021). Climate change and its impacts in Southern Africa: A synthesis of existing evidence in support of the World Food Programme's 2021 Climate Change Position Paper. *Climate Change, Agriculture and Food Security (CCAFS)*, (358).
- [LXXXII] Ratnam, J. V., S. K. Behera, Y. Masumoto, and T. Yamagata, 2014: Remote Effects of El Niño and Modoki Events on the Austral Summer Precipitation of Southern Africa. *Journal of Climate*, 27, 3802-3815.
- [LXXXIII] Reason, C. J. C., 2001: Subtropical Indian Ocean SST dipole events and southern African rainfall. *Geophysical Research Letters*, 28, 2225-2227.
- [LXXXIV] Reyer, C. P., Leuzinger, S., Rammig, A., Wolf, A., Bartholomeus, R. P., Bonfante, A., ... & Pereira, M. (2013). A plant's perspective of extremes: terrestrial plant responses to changing climatic variability. *Global change biology*, 19(1), 75-89.
- [LXXXV] Rosenzweig, C., Iglesias, A., Yang, X. B., Epstein, P. R., & Chivian, E. (2001). Climate Change and Extreme Weather Events; Implications for Food Production, Plant Diseases, and Pests. *Global Change and Human Health*, 2(2), 90-104. doi:10.1023/A:1015086831467
- [LXXXVI] Russo, S., Dosio, A., Graversen, R. G., Sillmann, J., Carrao, H., Dunbar, M. B., Singleton, A., Montagna, P., Barbola, P., and Vogt, J. V. (2014), Magnitude of extreme heat waves in present climate and their projection in a warming world, *J. Geophys. Res. Atmos.*, 119, 12,500– 12,512, doi:10.1002/2014JD022098.
- [LXXXVII] Saji, N. H., B. N. Goswami, P. N. Vinayachandran, and T. Yamagata, A dipole mode in the tropical Indian Ocean, *Nature*, 401, 360–363, 1999
- [LXXXVIII] Santamaria, L., Riishojgaard, L. P., Harding, J., Larroquette, B., & Zoetelief, J. (2021). No Member Left Behind—Part 2. Development partners' perspectives on overcoming sustainability challenges in observing networks and data exchange—lessons learned. *Boletín-Organización Meteorológica Mundial*, 70(2), 76-82.
- [LXXXIX] Sazib N, Mladenova IE and Bolten JD (2020) Assessing the Impact of ENSO on Agriculture Over Africa Using Earth Observation Data. *Front. Sustain. Food Syst.* 4:509914. doi: 10.3389/fsufs.2020.509914
- [XC] Semenov, M. A. (2007). Development of high-resolution UKCIP02-based climate change scenarios in the UK. *Agricultural and Forest Meteorology*, 144(1-2), 127-138. doi:10.1016/j.agrformet.2007.02.003
- [XCI] Seneviratne, S.I., X. Zhang, M. Adnan, W. Badi, C. Dereczynski, A. Di Luca, S. Ghosh, I. Iskandar, J. Kossin, S. Lewis, F. Otto, I. Pinto, M. Satoh, S.M. Vicente-Serrano, M. Wehner, and B. Zhou, 2021: Weather and Climate Extreme Events in a Changing Climate. In *Climate Change 2021: The Physical Science Basis. Contribution of Working Group I to the Sixth Assessment Report of the Intergovernmental Panel on Climate Change* [Masson- Delmotte, V., P. Zhai, A. Pirani, S.L. Connors, C. Péan, S. Berger, N. Caud, Y. Chen, L. Goldfarb, M.I. Gomis, M. Huang, K. Leitzell, E. Lonnoy, J.B.R. Matthews, T.K. Maycock, T. Waterfield, O. Yelekçi, R. Yu, and B. Zhou (eds.)]. Cambridge University Press, Cambridge, United Kingdom and New York, NY, USA, pp. 1513–1766, doi:10.1017/9781009157896.013
- [XCII] Serdeczny, O., Adams, S., Baarsch, F., Coumou, D., Robinson, A., Hare, W., . . . Reinhardt, J. (2017). Climate change impacts in Sub-Saharan Africa: from physical changes to their social repercussions. *Regional Environmental Change*, 17(6), 1585-1600. doi:10.1007/s10113-015-0910-2
- [XCIII] Solaraju-Murali, B., Gonzalez-Reviriego, N., Caron, L.-P., Ceglar, A., Toreti, A., Zampieri, M., . . . Doblas-Reyes, F. J. (2021). Multi-annual prediction of drought and heat stress to support decision making in the wheat sector. *npj Climate and Atmospheric Science*, 4(1). doi:10.1038/s41612-021-00189-4
- [XCIV] Sørland, S. L., Brogli, R., Pothapakula, P. K., Russo, E., Van de Walle, J., Ahrens, B., ... Thiery, W. (2021). COSMO-CLM regional climate simulations in the Coordinated Regional Climate Downscaling Experiment (CORDEX) framework: a review. *Geoscientific Model Development*, 14(8), 5125–5154. <https://doi.org/10.5194/gmd-14-5125-2021>
- [XCV] Stevens, M. J. M., & Smulders, P. T. (1979). The Estimation of the Parameters of the Weibull Wind Speed Distribution for Wind Energy Utilization Purposes. *Wind Engineering*, 3(2), 132–145.

<http://www.jstor.org/stable/43749134>

- [XCVI] Stuch, B., Alcamo, J., & Schaldach, R. (2020). Projected climate change impacts on mean and year-to-year variability of yield of key smallholder crops in Sub-Saharan Africa. *Climate and Development*, 13(3), 268-282. doi:10.1080/17565529.2020.1760771
- [XCVII] Sun, Q., Miao, C., Qiao, Y. et al. The nonstationary impact of local temperature changes and ENSO on extreme precipitation at the global scale. *Clim Dyn* 49, 4281–4292 (2017). <https://doi.org/10.1007/s00382-017-3586-0>
- [XCVIII] Taschetto, A.S., Ummenhofer, C.C., Stuecker, M.F., Dommenges, D., Ashok, K., Rodrigues, R.R. and Yeh, S.W., 2020. ENSO atmospheric teleconnections. El Niño southern oscillation in a changing climate, pp.309-335, <https://doi.org/10.1002/9781119548164.ch14>.
- [XCIX] Taylor, K.E., 2001. Summarizing multiple aspects of model performance in a single diagram. *Journal of Geophysical Research: Atmospheres*, 106(D7), pp.7183–7192, <https://doi.org/10.1029/2000JD900719>.
- [C] Tebaldi, C., & Lobell, D. (2018). Differences, or lack thereof, in wheat and maize yields under three low-warming scenarios. *Environmental Research Letters*, 13(6). doi:10.1088/1748-9326/aaba48
- [CI] Thoithi, W., Blamey, R. C., & Reason, C. J. C. (2021). Dry Spells, Wet Days, and Their Trends Across Southern Africa During the Summer Rainy Season. *Geophysical Research Letters*, 48(5), e2020GL091041. doi:<https://doi.org/10.1029/2020GL091041>
- [CII] Trisos, C. H., Adelekan, I. O., Totin, E., Ayanlade, A., Efitre, J., Gameda, A., ... Zakieldeen, S. (2022). Nine principles for encouraging a context-driven, inclusive and proactive approach to planning for climate risk in African cities. *Climate Change 2022: Impacts, Adaptation and Vulnerability*. <https://doi.org/10.1017/9781009325844.011.1286>
- [CIII] Troccoli, A., Harrison, M., Anderson, D.L.T., Mason, S.J., 2008. Seasonal Climate: Forecasting and Managing Risk, Seasonal Climate: Forecasting and Managing Risk. <https://doi.org/10.1007/978-1-4020-6992-5>.
- [CIV] Tuel, A., & Martius, O. (2021). A global perspective on the sub-seasonal clustering of precipitation extremes. *Weather and Climate Extremes*, 33. doi:10.1016/j.wace.2021.100348
- [CV] Vashisht, A., Zaitchik, B. and Gnanadesikan, A., 2021. ENSO teleconnection to eastern African summer rainfall in global climate models: Role of the tropical easterly jet. *Journal of Climate*, 34(1), pp.293-312, <https://doi.org/10.1175/JCLI-D-20-0222.1>.
- [CVI] Vogel, E., Donat, M. G., Alexander, L. V., Meinshausen, M., Ray, D. K., Karoly, D., . . . Frieler, K. (2019). The effects of climate extremes on global agricultural yields. *Environmental Research Letters*, 14(5). doi:10.1088/1748-9326/ab154b
- [CVII] Wang, F. (2010), Subtropical dipole mode in the Southern Hemisphere: A global view, *Geophys. Res. Lett.*, 37, L10702, doi:10.1029/2010GL042750.
- [CVIII] Werner, A. T., & Cannon, A. J. (2016). Hydrologic extremes – an intercomparison of multiple gridded statistical downscaling methods. *Hydrology and Earth System Sciences*, 20(4), 1483-1508. doi:10.5194/hess-20-1483-2016
- [CIX] Weyn, J. A., Durran, D. R., Caruana, R., & Cresswell-Clay, N. (2021). Sub-Seasonal Forecasting With a Large Ensemble of Deep-Learning Weather Prediction Models. *Journal of Advances in Modeling Earth Systems*, 13(7). doi:10.1029/2021ms002502
- [CX] Wheeler, T., & von Braun, J. (2013). Climate Change Impacts on Global Food Security. *Science*, 341(6145), 508-513. doi:10.1126/science.1239402
- [CXI] Williams, C. A. and Hanan, N. P.: ENSO and IOD teleconnections for African ecosystems: evidence of destructive interference between climate oscillations, *Biogeosciences*, 8, 27–40, <https://doi.org/10.5194/bg-8-27-2011>, 2011.
- [CXII] WMO, 2003. Weather and Climate Forecasts for Agriculture, in: Guide to Agricultural Meteorological Practices. WMO, pp. 1–57
- [CXIII] World Meteorological Organization (WMO), 2012: Standardized Precipitation Index User Guide (M. Svoboda, M. Hayes and D. Wood). (WMO-No. 1090), Geneva.
- [CXIV] Zargar, A., Sadiq, R., Naser, B. and Khan, F.I. (2011) A Review of Drought Indices. *Environmental Reviews*, 19, 333-349. <https://doi.org/10.1139/a11-013>

- [CXV] Zscheischler, J., Martius, O., Westra, S., Bevacqua, E., Raymond, C., Horton, R. M., . . . Vignotto, E. (2020). A typology of compound weather and climate events. *Nature Reviews Earth & Environment*, 1(7), 333-347. doi:10.1038/s43017-020-0060-z
- [CXVI] Zscheischler, J., Westra, S., van den Hurk, B. J. J. M., Seneviratne, S. I., Ward, P. J., Pitman, A., . . . Zhang, X. (2018). Future climate risk from compound events. *Nature Climate Change*, 8(6), 469-477. doi:10.1038/s41558-018-0156-3